Transient heat transfer measurements in a short duration hypersonic facility on a blunted cone-flare using QIRT.
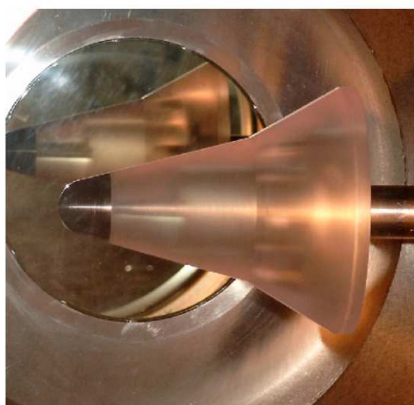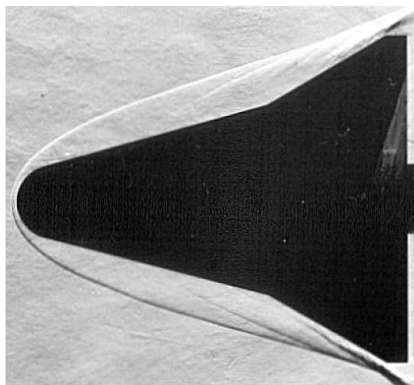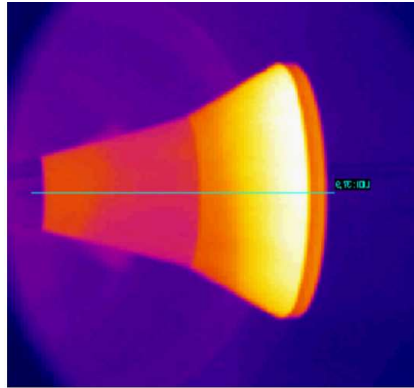
March 20, 2003

F.F.J.Schrijer

TUDelft

Delft University of Technology

Department of Aerospace Engineering

Summary

In the aerothermal design of winged re-entry vehicles it is important to understand the hypersonic flow phenomena around a wing with its extended flaps, in its relevance to flap effectiveness and aerodynamic surface heating. With this motivation the hypersonic flow over an axisymmetric compression corner has been studied, with its related boundary layer separation an reattachment phenomenon. The model under investigation is DART (Delft Aerospace Re-entry Test vehicle), a re-entry demonstrator vehicle, which is designed and developed at the Faculty of Aerospace engineering of TU Delft. The vehicle is designed to be fully reusable and has the task to collect aerothermodynamic flight data and to test new thermal protection system concepts. It is a blunted cone-flare made of Makrolon, a thermoplast with a high emissivity and low conductivity.

Transient heat transfer measurements were conducted in a short duration hypersonic facility at Mach 9, schlieren visualization was used as a complementary tool. The surface temperature variation in time was obtained using an infrared camera which operated in line-scan model to obtain an adequate sampling rate. The camera was successfully calibrated using a black-body and the emissivity of the model also was successfully determined.

Data reduction

The measured temperature transient can be correlated to heat transfer by means of a one-dimensional semi-infinite wall approximation. For the thermal data reduction two different approaches were employed: a numerical integration of the temperature signal and an optimization curve-fit process. Two numerical integration techniques were investigated. In the first method the heat transfer is calculated directly using the method of Cook and Feldermann however, this method is rather noise sensitive. Therefore an indirect method was used as well, which first calculates the cumulative heat input into the model. The heat transfer is then obtained as the derivative of the cumulative heat input and can be computed using finite differencing. For the optimization process two theoretical curves were employed, which were fitted to the measured temperature signal using the simplex optimization method. The first theoretical curve is based on the hypothesis of a constant value of the convective heat transfer coefficient, whereas the second theoretical curve is valid for a constant value of the heat transfer itself. All the employed methods yielded very comparable results for the heat transfer.

Flow analysis

In order to study the effect of roughness induced boundary layer turbulence, two different configurations were investigated, with a smooth nose or a roughened nose. The roughness was obtained by adding three rings, which were made of copper wire, to the model nose. Heat transfer measurements were performed at different values for the Reynolds number to investigate Reynolds number influence. For the clean nose configuration the heat transfer was found to decrease slightly with downstream distance due to laminar boundary layer development. Following the laminar part an abrupt drop in heat transfer was observed, which is a result of the boundary layer separation due to the adverse pressure gradient caused by the flare. The separation point was found to move downstream with increasing Reynolds number which, according to literature, is indicative of a transitional state of the boundary layer. The separation point inferred from the schlieren pictures

was found to agree with the separation location observed from the heat transfer measurements. At the flare the heat transfer increases strongly due to flow compression and at about half of the flare length an inflexion point in the heat transfer distribution is noted. This point closely correlates with the location of the compression wave observed from schlieren pictures. At the end of the flare maximum heating is reached. The peak heating ratio deduced from the measurements was found to be considerable and is probably caused by transition in the separated shear layer. This conjecture is supported by spark schlieren visualization which shows unsteady flow features near the end of the flare. Due to the bow shock an entropy layer is generated which also recompresses along the flare masking some flow features regarding transition and reattachment.

For the roughened nose configuration the heat transfer near the nose is a factor 1.5 higher and the separation point is more sensitive to the Reynolds number with respect to the clean nose. The roughened nose also shows an downstream movement of the separation point when increasing the Reynolds number. At high Reynolds numbers the separation region vanishes and a single compression wave can be seen in the schlieren pictures emerging from the cone-flare junction. At the flare the heat transfer increases considerably until a plateau is noted which again is connected with free shear layer transition.

For the roughened nose experiments the steepness of the heat transfer at the cone-flare junction is considerably higher compared to the clean nose configuration. This is believed to be caused by a faster decrease of the free shear layer thickness which is caused by establishing more efficient mixing in the shear layer due to the perturbation of the boundary layer that is caused by the roughness elements at the nose.

Acknowledgments

This report represents my Master Thesis of my graduation at the Department of Aerospace Engineering at Delft University of Technology, in the section Aerodynamics.

Four years ago I did a project on the design of a re-entry vehicle in the framework of the Design Synthesis exercise which forms part of the 3rd year of the study. This project was continued by the faculty of Aerospace Engineering and the DART-project was started. For myself it initiated great interest in high speed aerodynamics. During my specialization in aerodynamics and attending gasdynamics lectures my interest in hypersonics grew considerably. So the thesis project was a great opportunity to continue in this direction. During the project I learned much about operating a hypersonic wind tunnel in all its aspects. Working with an infrared camera and the development of the heat transfer measurement technique considerably improved my understanding on heat transfer theory and radiation principles. But most of all I have learned to handle a large project like this.

During my project I received a lot of help from a number of people. First of all I would like to thank Fulvio Scarano and Bas van Oudheusden for all their supervision and advice. I also want to thank Eric de Keizer for helping me with the operation of the HTFD and for answering all my questions about it, Frits Donker Duyvis for setting up the schlieren system and Peter Duyndam for always building things on a short notice. I also want to thank Prof. dr. G. Carlomagno, dr. T. Astarita and Prof. dr. G. Cardone for introducing me into the world of Quantitative Infrared Thermography. Furthermore I want to thank all the people in the cellar for the continuous discussions (on aerodynamics...).

Above all I would like to thank my parents and friends for always listening to my complaints and encouraging me during my study.

Ferry Schrijer
Delft, March 2003

Contents

Nomenclature

Latin

a	speed of sound	$[m/s]$
A	cross section, area	$[m^2]$
B	calibration constant spectral factor	$[-]$
c	thermal capacity	$[J/(kg\ K)]$
c_f	friction coefficient	$[-]$
c_h	Stanton number	$[-]$
c_p	specific heat at constant pressure	$[J/(kg\ K)]$
c_v	specific heat at constant volume	$[J/(kg\ K)]$
C	Chapman-Rubesin linear viscosity law constant	$[-]$
C_1	first radiant constant	$[Wm^2]$
C_2	second radiant constant	$[mK]$
d	diameter	$[m]$
E	energy per surface area	$[W/m^2]$
f	function value	$[K]$
F	calibration constant shape factor	$[-]$
h	heat transfer coefficient, enthalpy	$[W/(m^2\ K)], [J/kg]$
I	sample value	$[-]$
k	nose drag coefficient	$[-]$
K	hypersonic similarity parameter, Gladstone-Dale coefficient	$[-], [m^3/kg]$
L	length, thickness	$[m]$
M	Mach number	$[-]$
n	refractive index	$[-]$
p	static pressure	$[N/m^2]$ or $[bar]$
p_t	total pressure	$[N/m^2]$ or $[bar]$
Pr	Prandtl number	$[-]$
q	heat flux, dynamic pressure	$[W/m^2], [N/m^2]$
Q	cumulative heat input	$[J/m^2]$
r	recovery factor	$[-]$
R	specific gas-constant, aperture, calibration constant response factor	$[J/(kgK)], [m], [-]$
Re	Reynolds number	$[-]$
s	entropy, distance along the body	$[J/(kgK)], [m]$
SRF	slit response function	$[-]$
t	time	$[s]$
T	static temperature	$[K]$ or $[°]$
T_t	total temperature	$[K]$ or $[°]$
u	flow speed	$[m/s]$
w	slit width	$[m]$

Greek

α	diffusivity, absorption coefficient, deflection angle	$[m^2/s]$, $[-]$, $[rad]$
δ	boundary layer thickness	$[m]$
δ^*	displacement thickness	$[m]$
ϵ	emissivity	$[-]$
γ	specific heat ratio (1.4)	$[-]$
κ	thermal conductivity	$[W/K]$
κ_ϵ	parameter controlling bluntness effect	$[-]$
λ	wavelength	$[m]$
μ	dynamic viscosity	$[kg/(m\ s)]$
ν	kinematic viscosity	$[m^2/s]$
ϕ	temperature	$[K]$
ρ	density, reflectivity	$[kg/m^3]$, $[-]$
σ	Stefan-Boltzmann constant	$[W/(m^2\ K^4)]$
τ	transmissivity	$[-]$
θ	angle	$[°]$ or $[rad]$
$\bar{\chi}$	hypersonic viscous interaction parameter	$[-]$

Subscript

0	reservoir
1	pre-shock, pre-interaction
2	post-shock
3	post-interaction
a	ambient
aw	adiabatic wall
b	tube, body
c	convective, cone
e	boundary layer edge
fl	flare
i	initial, incipient
L	length of the model
o	beginning of interaction, object
p	plateau
r	radiative, re-attachment
s	surface, shock
sep	separated
t	total
tr	transition
w	wall
λ	spectral
∞	free stream

Superscript

*	evaluated at the reference temperature

Abbreviation

BRUT	burst recording unit
CCD	charged coupled device
FOV	field of view
IFOV	instantaneous field of view
IR	infrared
LWB	low wave band
NETD	noise equivalent temperature difference
SWB	short wave band

Chapter 1

Introduction

The need for more cost effective launchers is growing due to the need for more commercial satellite launches. Also the expansion and continuation of projects like the international space station depend on the usage of less expensive space transportation systems. The development of a cost effective launcher focuses on three important aspects. Single stage to orbit (SSTO), re-usability and a horizontal launch system. The SSTO concept still poses big problems; engine performance is still not adequate both for rocket powered as air-breathing combined-cycle engines [12]. So a switch is made to Two stage to orbit (TSTO) which can be achieved using current day or near future technology. The re-usability poses some strict constraints on structural design and thermal protection system (TPS); the structure has to be strong enough to withstand several re-entry load cycles but also has to be light enough to insure propellant fraction. The TPS has to be optimized for the same reasons, this means the thermal loads during re-entry have to be carefully evaluated. The third important aspect is horizontal launch. If a vehicle is horizontally launched, both ground and flight operations can be based on aircraft operations which further reduces costs. The launcher can accelerate in less denser atmosphere which reduces heating and a horizontal launch is favorable for the astronauts. In order to achieve a horizontal launch and landing, the launcher needs wings. From previous experience with the space shuttle it appeared that the wings introduced problems with respect to structural mass and flap effectiveness. To be able to further optimize the wings it is important to understand the hypersonic flow phenomena around a wing with its extended flaps, in its relevance to flap effectiveness and aerodynamic surface heating.

With this motivation the flow over an axisymmetric compression corner is studied, with its related flow separation and shock interaction. The model which is studied is DART (Delft Aerospace Re-entry Test vehicle), a re-entry demonstrator vehicle, which is designed and developed at the Faculty of Aerospace Engineering of TU Delft. In the next section some more details about the DART are given. The investigation is conducted by experimental means in the hypersonic facility of TUDelft Aerospace engineering. Quantitative infrared thermography was used to evaluate the spatial heat transfer distribution on the model and to do flow diagnostics, these measurements were supplemented by means of schlieren visualization.

1.1 The DART project

In 1999 a group of students at the Faculty of Aerospace Engineering of TU Delft had the assignment to design a small reusable re-entry vehicle which would be affordable for Delft Aerospace and which could be designed in-house. The outcome of the study was promising and was well received by referees from ESA-ESTEC and Fokker Space, so it was decided to continue studying the re-entry vehicle [8].

1.1.1   Goals

The long-term goal behind the re-entry research such as the DART project is the development of fully reusable, low cost launch vehicles and hypersonic transports. In order to achieve this goal a better understanding of the hypersonic flow regime is needed. Also knowledge about the behavior of certain materials under re-entry conditions is needed. And finally a new light-weight, easy to maintain reusable thermal protection system has to be developed.

Since it is not possible to reproduce all aspects of hypersonic flight in wind tunnel facilities and current computer codes do not give accurate enough results, there is a need for flight testing in order to achieve further knowledge before constructing a full-scale reusable launcher.

The main goals which have to be achieved in the DART project are the validation of a hot metal external load-carrying structure and the collection of aerothermodynamic data for CFD and aerodynamic theory validation with the emphasis on the study of separation and reattachment of the boundary layer. Secondary goals are the validation of new thermal protection system concepts and validation of computer codes regarding hypersonic aerodynamics, trajectory simulations and stability (vehicle control).

1.1.2   Launcher

The launcher selected for DART is a Russian decommissioned SLBM named Volna (see figure 1.1). The total launch weight of the Volna is 35.3 tons, the length is 14.1 m and it has a diameter of 1.8 m. The launcher has liquid propellants and can be launched in any weather (from a submerged
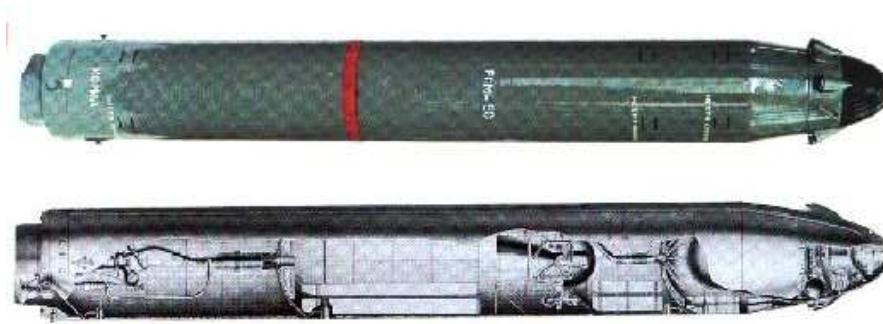
Figure 1.1: Volna launcher, taken from [1]

submarine). Since the launcher is a former nuclear-armed missile it is designed for reliability and accuracy. The payload bay has a diameter of 1300 mm and a length of 1650 mm. The maximum mass allowed for the payload is 500 kg, this is more than sufficient for the DART vehicle. The re-entry vehicle hangs upside down between the second and third stage of the launcher. After the boost phase the third stage aims the re-entry vehicle for the ballistic phase. The vehicle will perform a re-entry at 100 km with a velocity of 7 km/s and at an entry angle of 5 °.

1.1.3   DART model geometry

The design of the outer geometry of the DART vehicle is driven by a number of considerations; the hypersonic aerodynamic experiments (mainly the viscous phenomena), the applied materials of the outer skin, the limitations of the cooling system, the required vehicle volume to accommodate the measurement equipment and the constraints posed by the Volna launcher. The simplest geometry is an axisymmetric blunted cone-flare. Two different geometries have been analyzed; the first one is based on the Russian Volan re-entry module depicted in figure 1.2, the second geometry is based on an in-house study and is called the REVolution. Both geometries have their advantages and disadvantages; the REVolution has a smaller nose radius than the Volan, which results in a larger

Figure 1.2: REVolution (left) and the Volan geometry (right), taken from [1]

heat flux but it has a stronger shock-wave boundary layer interaction which is the phenomenon to be investigated. This interaction increases again the heat flux on the flare which is a disadvantage.
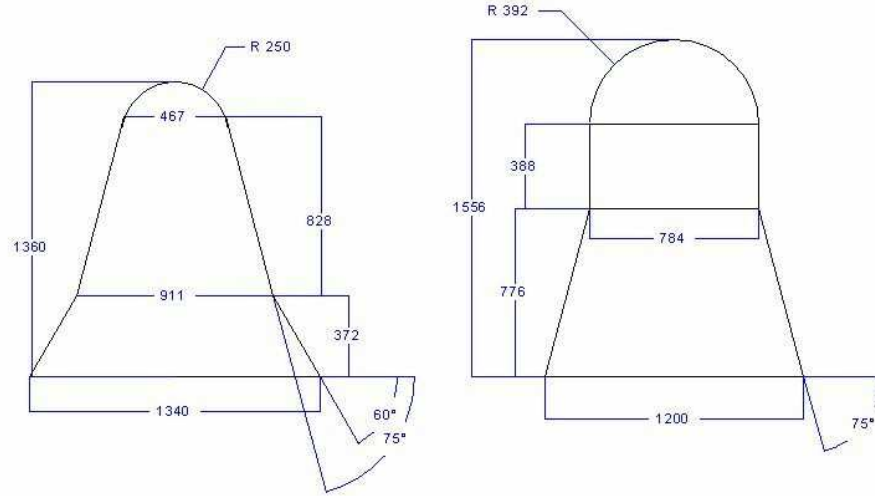
1.1.4 Outer structure and thermal protection

For the external structure, PM1000 ODS(Oxide-Dispersion Strengthened) will be used, this material is an alloy which can withstand temperatures up to 1200 °C. A strong oxide layer protects the underlying material from the aggressive atomic oxygen environment which is generated during re-entry. During a ballistic re-entry the nose will endure the highest heat load, to prevent the nose from melting it is cooled by water. To achieve this the entire spherical part of the nose is integrated into a water tank, see figure 1.4. A major part of the heat which is generated at the nose during re-entry will be absorbed by the water which will heat up and evaporate. Due to this process the inside of the nose will remain at boiling temperature. The water vapor will ejected through a pressure valve to the base of the vehicle. The total amount of water which is needed depends on the thermal loading history and the nose radius, in the most severe case less than 8 kg of water is needed to cool a nose which has a radius of 200 mm [8].

The cone and flare part of the vehicle also need to be cooled. This is done by placing a porous layer which is saturated with water behind the hot PM1000 outer wall. The hot outer wall will radiate its heat to the porous material, the temperature of the saturated material will not exceed approximately 100 °C due to the boiling temperature of the water, see figure 1.3. This results in a steady cool background for the hot outer wall to radiate its heat onto. In this way the wall can both radiate in- and outward, this increases the radiation cooling efficiency. The evaporated water will be vented through the base of the vehicle adding some convection cooling to the system. The concept of the TPS is currently tested and the theory is already validated [1].
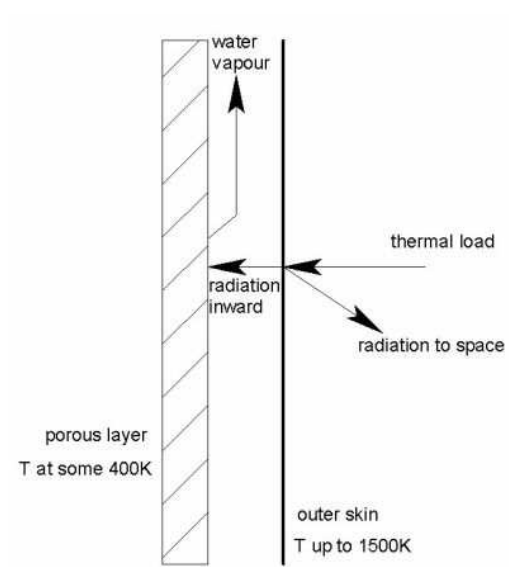
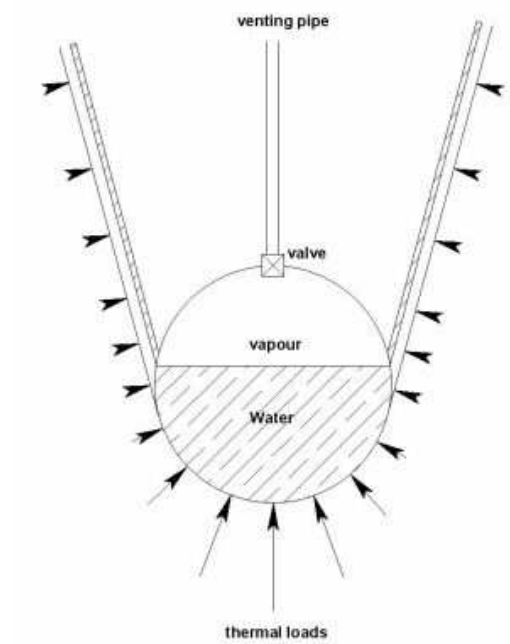Figure 1.3: Concept of porous layer TPS, taken from [1]

Figure 1.4: Nose cooling concept for DART, taken from [1]

1.1.5 DART aerodynamics

During reentry the DART vehicle will pass through several speed regimes, from highly hypersonic at the beginning to low subsonic flow at the end of the trajectory. The hypersonic flow regime will impose severe heat loads on the vehicle. The main flow features in the hypersonic/supersonic flow regime are the curved bow shock in front of the vehicle and the separation and reattachment phenomenon near the cone-flare junction.

As the oncoming flow passes through the bow shock it will be decelerated causing the density
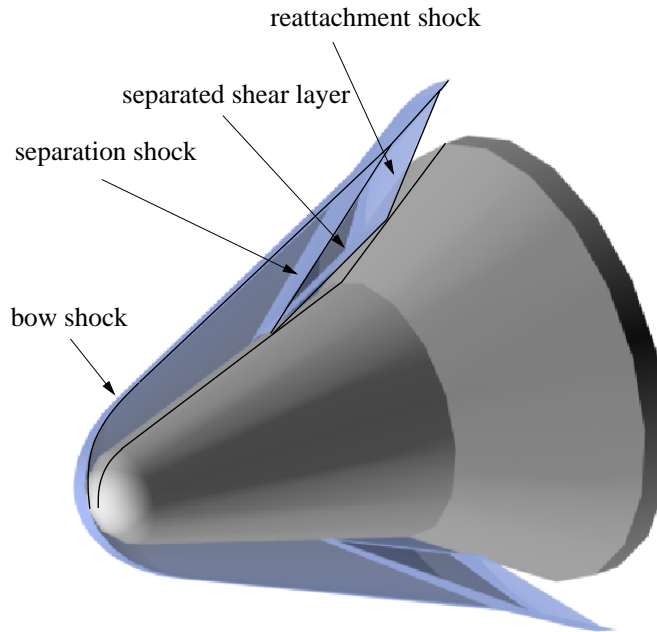
Figure 1.5: Impression of the hypersonic flow round the REVolution concept

and temperature to increase. The largest deceleration occurs through the most normal part of the bow shock (stagnation region). In the stagnation region the flow will come to a complete standstill inducing high convective heating. To reduce the heating, the nose of the vehicle is blunted.

Moving further downstream the flow accelerates along the blunted nose reducing the pressure and heat transfer. At the cone the pressure remains constant (depending on the bluntness also a pressure over- or undershoot can occur) and the heat transfer will continue to decrease along the cone due to boundary layer growth. At the aft part of the cone the bow shock will become straight with a shock angle equal to the shock generated by a sharp cone having the same cone angle.

As the boundary layer approaches the flare, it will separate causing a separation shock which, further downstream, merges with the bow shock. As the boundary layer reattaches at the flare, the reattachment shock will deflect the flow so that it runs parallel to the flare. Due to the compression the boundary layer thickness will reduce causing high heating rates. Besides higher heat rates the flare also induces higher pressures stabilizing the vehicle during reentry.

1.2 Aim of the investigation

The aims of the present work are the application of quantitative infrared thermography in a short duration hypersonic facility together with the accessory data reduction methods for heat transfer determination. Quantitative infrared thermography is applied to detect and investigate

the separation and reattachment of a hypersonic boundary layer on a blunted cone-flare. For flow-field diagnostics the heat transfer measurements will be complemented by Schlieren visualization. The model geometry used in the current study is equivalent to the REVolution concept and will be referred to as the DART model.

1.3   Outline of the thesis

The thesis is organized as follows; in chapter 1 a short introduction on the DART project is given. In the second chapter an analysis of the flow field and the heat transfer is presented; some typical flow parameters will be discussed as well as heat transfer correlations. Typical compression ramp phenomena will be discussed and important bluntness effect will be analyzed.

In chapter 3 the experimental apparatus will be addressed such as the hypersonic wind tunnel (HTFD), the cone-flare model and the schlieren visualization system. Also the different experimental configurations will be discussed.

Chapter 4 deals with the infrared measurement technique; infrared theory is discussed and the data acquisition system is presented. Finally this chapter deals with the calibration of the infrared camera and the emissivity measurement of the model material.

Chapter 5 discusses the applied data reductions with their theory and implementation. Also the performance of the data reduction models is analyzed.

In chapter 6 the results will be discussed, first the flow quality is checked and secondly the experimental results are presented.

Finally in chapters 7 and 8 the conclusions and recommendations will be given.

Chapter 2

Flow analysis

2.1 General flow description

The flow around the cone-flare geometry is dominated by the curved bow shock. In the front part of the shock where strong solutions of the shock wave equations apply, the flow is subsonic behind the shock, see figure 2.1. In this region large convective heat transfer occurs. As the

M$_1$ >1

streamlines

outer edge of
entropy layer

sonic line

M$_2$ <1

stagnation point

boundary layer

M$_2$ >1
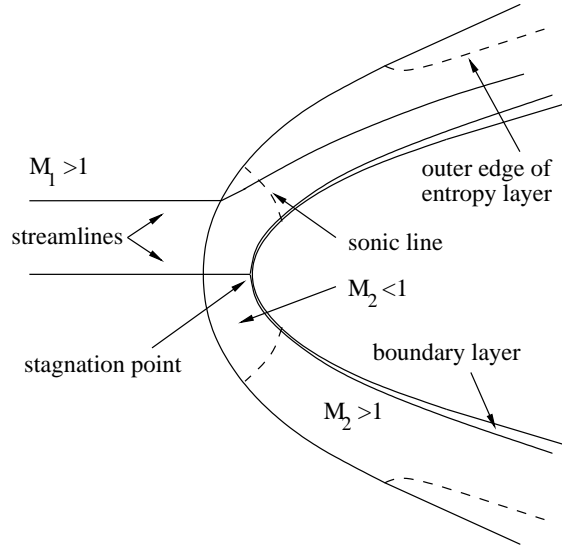
Figure 2.1: Blunt body flow field

flow accelerates further downstream the heat transfer decreases. Generally due to the blunted nose the boundary layer stabilizes and transition occurs further downstream than in the case of a sharp nose. But for a large bluntness transition may occur prematurely, this destabilizing effect is referred to as the "blunt nose paradox" [3] and is connected with an overexpansion at the nose-cone junction.

Due to the curved bow shock, the flow exhibits an entropy gradient. For perfect gas flow the entropy difference over a shock wave is given by [7]:

$$s_2 - s_1 = \frac{R}{(\gamma - 1)} \left\{ \ln \left[\frac{2\gamma M_1^2 \sin^2 \theta - (\gamma - 1)}{(\gamma + 1)} \right] - \gamma \ln \left[\frac{(\gamma + 1) M_1^2 \sin^2 \theta}{(\gamma - 1) M_1^2 \sin^2 \theta + 2} \right] \right\}.$$

When regarding the above equation it is evident that the entropy rise over a streamline passing the nearly normal portion of the bow shock experiences a larger entropy increase than does the

streamline passing the more oblique portion of the shock wave. Since the entropy is constant along a streamline for an inviscid, adiabatic and steady flow, the entropy will vary continuously through the shock layer. Since the curvature at the front of the bow shock is relatively strong an entropy layer is formed in which the boundary layer will develop. This layer encompasses a strong variation in the total pressure. For a normal shock wave in a free-stream Mach number of 9.13 a pressure loss of $\frac{p_{t_2}}{p_{t_1}} = 0.4646 \times 10^{-2}$ results while for an 18° oblique shock-wave a total pressure loss of $\frac{p_{t_2}}{p_{t_1}} = 0.1831$ results. This shows that a considerable variation is present in the total pressure throughout the entropy layer. Proceeding further downstream from the nose the boundary layer will encounter the compression corner which will introduce an increasing pressure on the boundary layer causing it to separate under the generation of a separation shock before the actual compression corner is reached (see sections 2.3.1 and 2.3.2). Depending on the extent of the separation region the boundary layer will reattach again at the flare causing a reattachment shock. This shock will recompress the flow inducing a high heat flux at the wall. At the base of the model the flow expands again.

2.1.1   Typical flow parameters

In this section some typical parameters will be discussed which are considered in this study. One of the most important flow parameters is the Reynolds number, it represents the relation between the viscous and inertial forces:

$$Re_x = \frac{\rho U_\infty x}{\mu}.$$

In the current study a slightly different definition of the Reynolds number is used:

$$Re_x = \frac{\rho_\infty U_\infty x}{\mu_\infty}. \tag{2.1}$$

where the Reynolds number is based on the free stream values ∞ and a characteristic length x. The parameter which indicates the compressibility of the flow is the Mach number, it is the ratio between the local flow speed and the speed of sound:

$$M = \frac{u}{a} \tag{2.2}$$

The Stanton number is used to describe the non dimensional convective heat transfer. For a calorically perfect gas ($h = c_p T$) it is defined as:

$$c_h = \frac{q_s}{c_p \rho_e u_e (T_{aw} - T_w)} \tag{2.3}$$

where c_h is the Stanton number and ρ_e and u_e are the density and velocity at the boundary layer edge. T_{aw} and T_w are respectively the adiabatic wall temperature and wall temperature. In the current study the definition adapted for the Stanton number is somewhat different:

$$c_h = \frac{q_s}{c_p \rho_\infty u_\infty (T_0 - T_w)}. \tag{2.4}$$

Where the reference values of ρ and u are taken as the free stream values and the total temperature rather than the adiabatic wall temperature is used. The free stream values are used since ρ and u are not available at the boundary layer edge. Since a short duration facility is used, the adiabatic wall temperature cannot be measured so the total temperature is chosen as reference using the following consideration: the classical definition for the adiabatic wall temperature is as follows [37]:

$$T_{aw} = T_\infty + r\frac{u_\infty^2}{2c_p} = T_\infty \left\{ 1 + r\frac{\gamma - 1}{2} M_\infty^2 \right\}. \tag{2.5}$$

For high values of the Mach number this equation may be approximated by:

$$T_{aw} \approx r \frac{u_\infty^2}{2c_p} \approx rT_t. \tag{2.6}$$

Due to the uncertainty in the recovery factor for general flow situations the modified Stanton number, equation (2.4) is generally applied.

The ratio of the viscous and the thermal diffusion rate is expressed by the Prandtl number:

$$Pr = \frac{\mu c_p}{\kappa}. \tag{2.7}$$

The Prandtl number can be calculated using the Sutherland viscosity and conductivity law (see section 5.6.1).

2.1.2 Interaction parameters

When regarding a flat plate at hypersonic Mach numbers, it is noticed that the pressure over the plate is significantly influenced by the rapid boundary layer development over the plate (the boundary layer thickness develops as $\frac{M_e^2}{\sqrt{Re_x}}$, [3], [33]). Due to the boundary layer growth a curved shock is generated which considerably influences the flow properties on the plate. This can be described by applying the tangent-wedge formula to an effective body described by the local slope of the displacement thickness $\left(\frac{d\delta^*}{dx} \right)$. Results and derivation of the viscous interaction theory are summarized in [3] and [33]. The viscous interactions can be divided into two cases: a strong interaction where $\frac{d\delta^*}{dx}$ is large so $K^2 = \left(M_\infty \frac{d\delta^*}{dx} \right)^2 \gg 1$ and a weak interaction where $\frac{d\delta^*}{dx}$ is moderate so $K^2 = \left(M_\infty \frac{d\delta^*}{dx} \right)^2 \ll 1$. In both interactions the equation for the pressure depends solely on one governing similarity parameter:

$$\bar{\chi} = \sqrt{C} \frac{M_\infty^3}{\sqrt{Re}}.$$

Where C is the Chapman-Rubensin linear viscosity parameter [39]:

$$C = \frac{\mu T_\infty}{\mu_\infty T} \tag{2.8}$$

The strong and weak interaction regimes are described by:

- Strong interaction $\bar{\chi} > 3$
- Weak interaction $\bar{\chi} < 3$.

For completeness also the viscous interaction parameters for turbulent flow are given:

- Strong interaction $\left(\frac{M_\infty^9 C}{Re} \right)^{2/7}$
- Weak interaction $\left(\frac{M_\infty^9 C}{Re} \right)^{1/5}$.

The viscous interaction parameters are only valid for sharp nosed models. When bluntness is applied, the pressure distribution can be calculated using blast wave theory which is discussed in [3] and [33]. When both bluntness and boundary layer displacement effects are governing the flow field, the pressure distribution can be approximated by applying a linear combination of the two effects, [15].

In [13] Cheng et al discussed the general viscous hypersonic similitude including the effects of leading edge bluntness. The boundary layer thickness, heat transfer and skin friction on a flat plate-wedge were determined from a locally similar solution of the boundary layer equations for

combined leading edge bluntness and boundary layer displacement effects. Cheng et al showed that the general similitude governing these parameters can be written in terms of the nondimensional parameters [13], [22] and [23]:

$$\left.\begin{array}{l} M^3 c_h \left(\kappa_{\epsilon,L}/\chi_{\epsilon,L}{}^2\right)^3 \\ M^3 c_f \left(\kappa_{\epsilon,L}/\chi_{\epsilon,L}{}^2\right)^3 \\ \left[\frac{p_w}{p_\infty}\right] c_h \left(\kappa_{\epsilon,L}/\chi_{\epsilon,L}{}^2\right)^2 \end{array}\right\} = f\left[\frac{x}{L}, \frac{\chi_{\epsilon,L}}{\kappa_{\epsilon,L}{}^{2/3}}, \frac{1}{2}\left(\frac{\kappa_{\epsilon,L}}{\chi_{\epsilon,L}}\right) M\theta, \left(\frac{\kappa_{\epsilon,L}}{\chi_{\epsilon,L}}, \gamma, \frac{T_w}{T_0}, Pr\right)\right]. \tag{2.9}$$

Where $\kappa_\epsilon = M^3 k\epsilon(d/x)$ is a parameter controlling the inviscid tip bluntness effect, $k = 2D_N/(\rho_\infty U_\infty^2 d)$ which is the nose drag coefficient and $\chi_\epsilon = \epsilon\left[0.664 + 1.73T_w/T_0\right]\bar{\chi}_L$.
Using the combined bluntness-viscous interaction parameter $\chi_\epsilon/\kappa_\epsilon^{2/3}$, the bluntness-dominated regime can be indentified as $\chi_\epsilon/\kappa_\epsilon^{2/3} < 0.1$. For $\chi_\epsilon/\kappa_\epsilon^{2/3} > 1$ the flow is displacement dominated where the viscous interaction theory is valid.
In the current experiments $\chi_\epsilon/\kappa_\epsilon^{2/3} \ll 0.1$, so the entire flow-field is bluntness dominated.

2.2   Cone flow

The heat transfer at the first conical part of the model can be approximated using the Taylor-Maccoll method for a sharp cone together with the reference temperature method.

2.2.1   Reference temperature

When predicting the heat transfer for both laminar and turbulent hypersonic flows the reference temperature concept is frequently used. The concept is based on the idea of utilizing the formulas obtained from incompressible flow theory and evaluating the thermodynamic and transport properties at some reference temperature indicative of the temperature somewhere inside the boundary layer. Using this idea, in a sense the classical incompressible formulas are "corrected" for compressibiliy effects. In Rasmussen [33] the reference temperature is derived as:

$$\frac{T^*}{T_e} = 0.566Pr^{1/3}\left[1 + \left(r - 0.744Pr^{2/3}\right)\frac{\gamma-1}{2}M_e^2\right] + \frac{T_w}{T_e}\left(1 - 0.566Pr^{1/3}\right) \tag{2.10}$$

In the derivation Reynolds analogy is used, which can be derived from the self similar energy equation as [33]:

$$\frac{c_h}{c_f} = \frac{Pr^{-2/3}}{2}. \tag{2.11}$$

2.2.2   Heat transfer estimation

When the incompressible laminar flow over a flat plate is considered classical theory predicts the Stanton number as:

$$c_h = \frac{0.332}{\sqrt{Re_x}}Pr^{-2/3}. \tag{2.12}$$

For turbulent flow, the incompressible result is:

$$c_h = \frac{0.0296}{Re_x^{0.2}}Pr^{-2/3}. \tag{2.13}$$

In this equation Re_x and Pr are based on the properties at the edge of the boundary layer. To expand equation (2.12) for compressible laminar flow over a flat plate, the reference temperature concept is used. The Reynolds and Prandtl numbers are evaluated at the reference temperature T^*:

$$Re_x^* = \frac{\rho^* u_e x}{\mu^*} \tag{2.14}$$

$$Pr^* = \frac{\mu^* c_p^*}{k^*} \tag{2.15}$$

where ρ^*, μ^*, c_p^* and k^* are also evaluated at the reference temperature. The laminar Stanton number can now be calculated as

$$c_h = \frac{0.332}{\sqrt{Re_x^*}} \left(Pr^*\right)^{-2/3} \tag{2.16}$$

while the turbulent Stanton number is given by

$$c_h = \frac{0.0296}{Re_x^{*\,0.2}} \left(Pr^*\right)^{-2/3} \tag{2.17}$$

To apply these equations to a cone (axisymmetric equivalent of a flat plate, also a flat pressure distribution), they have to be transformed to their axisymmetric equivalents using the Mangler transformation [33]. In practise it is not needed to completely transform the equations, it is sufficient to multiply the result with the Mangler fraction, $\sqrt{3}$, although caution has to be taken that this is not valid for all calculated parameters.

Due to the three dimensional relieving effect the Stanton number for a flat plate is lower than for a cone. When comparing a cone to a flat plate the boundary layer becomes thinner which results in larger velocity and temperature gradients inducing higher heat transfer.

2.2.3   Taylor-Maccoll method

The inviscid flow past a sharp cone at zero incidence can be described by a single second-order ordinary differential equation [33], [4] (see figure 2.2):

$$\frac{\gamma - 1}{2} \left[u_{max}^2 - u_r{}^2 - \left(\frac{\mathrm{d}u_r}{\mathrm{d}\theta}\right)^2 \right] \left[2u_r + \frac{\mathrm{d}u_r}{\mathrm{d}\theta}\cot\theta + \frac{\mathrm{d}^2 u_r}{\mathrm{d}\theta^2} \right] - \frac{\mathrm{d}u_r}{\mathrm{d}\theta}\left[u_r \frac{\mathrm{d}u_r}{\mathrm{d}\theta} + \frac{\mathrm{d}u_r}{\mathrm{d}\theta}\frac{\mathrm{d}^2 u_r}{\mathrm{d}\theta^2} \right] = 0 \tag{2.18}$$

where u_r is the velocity in radial direction and u_{max} is the maximum theoretical velocity obtainable from a fixed reservoir condition $\left(h_t = \mathrm{const} = h + \frac{u^2}{2} = \frac{u_{max}^2}{2} \right)$. This equation can be numerically integrated from the shock to the surface of the cone. The surface of the cone is reached when $u_\theta = \frac{\mathrm{d}u_r}{\mathrm{d}\theta}$ is equal to zero (for a solid wall, the velocity normal to the wall is zero), then the cone angle is also known. If the cone angle is too large the starting shock angle must be decreased and vice versa. In this way for a given cone angle a shock-wave angle θ_s and Mach number M_e at the cone surface can be iteratively calculated. Using the free stream Mach number and the shock angle, the decrease in total quantities and Mach number can be calculated. Using the isentropic relations also the flow variables on the cone surface can be calculated. The flow variables at the cone surface can now be used as input variables for boundary layer calculations such as the reference temperature method.

2.3   Compression ramp flow

In literature several studies have been conducted on shock wave boundary layer interactions in high speed flows. Most studies dealt with both compression corner flow and impinging shock flows. Both flows are equivalent through Chapman's "free interaction region" principle. In the current study only results obtained from compression ramp interactions are discussed.

2.3.1   Description of the inviscid compression ramp flow

When looking at the inviscid flow field near the cone-flare junction, the classification scheme of Edney can be used to categorize the shock interactions created by the cone-flare configuration.
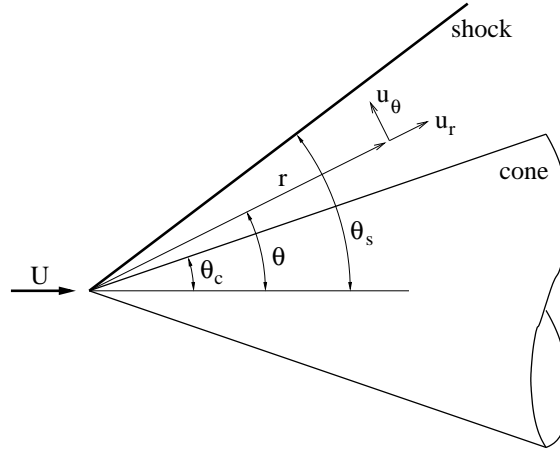
Figure 2.2: Coordinate system for the Taylor-Maccoll equation

Olejniczak et al [32] conducted a numerical study solving the two dimensional Euler equations with a finite-volume computational fluid dynamics method. In the study, double-wedge flows were considered. When looking at the configuration in figure 2.3, it is clearly visible that the cone-flare geometry including the separated region is equivalent to a double-wedge geometry. In the discussion the bow shock is omitted, this is justified since the bow shock is relatively far away from the surface so it does not take part in the shock-shock interaction due to the compression ramp. The shock wave created by the first wedge is analogous to the shock created by the separating
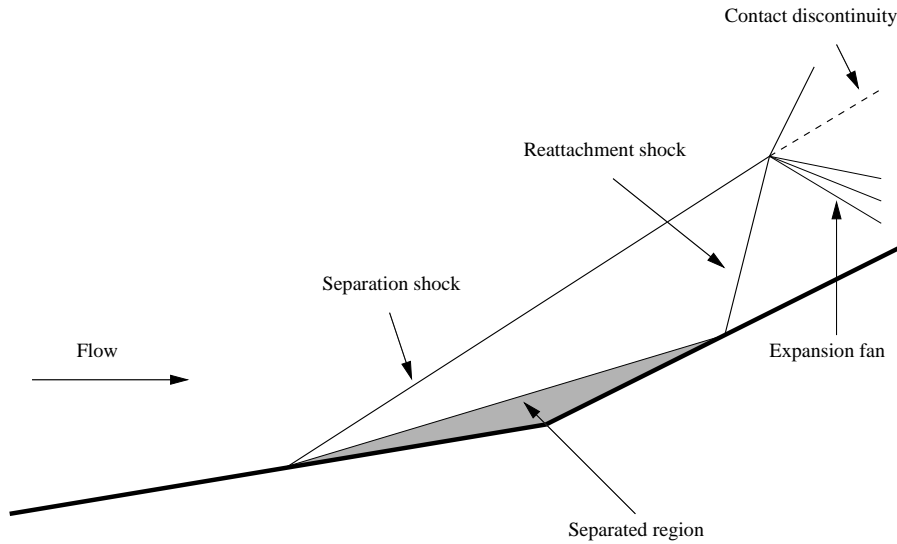
Figure 2.3: Inviscid flow field over a separated compression corner

boundary layer and the shock due to the compression corner between the first and second wedge is analogous to the shock created by the reattaching boundary layer. The only interaction possible for the present cone-flare configuration at $M = 9$ is the type IV interaction. The separation shock intersects with the shock induced by the reattaching boundary layer. A contact discontinuity (slipline) is produced separating two regions, one region near to the wall contains the flow which has passed through both oblique shocks and the second region away from the wall contains the flow which has only passed through the oblique shock produced by the reattaching boundary layer.

The intersection of the two oblique shock also produces a third wave, the nature of this relatively weak wave (shock or expansion) strongly depends on the free stream conditions.

2.3.2 Description of the viscous compression ramp flow

In the previous section the inviscid outer flow over a compression ramp with its accompanying separated region is discussed. In this section the development of the separated region is discussed. In the current discussion based on [37] the interaction is regarded as being two dimensional which is a good approximation for axisymmetric flows since it is assumed they have no axial gradients. In the discussion the influence of the entropy layer is omitted for simplicity.

If the flow was to be inviscid, no boundary layer would be present and an oblique shock would
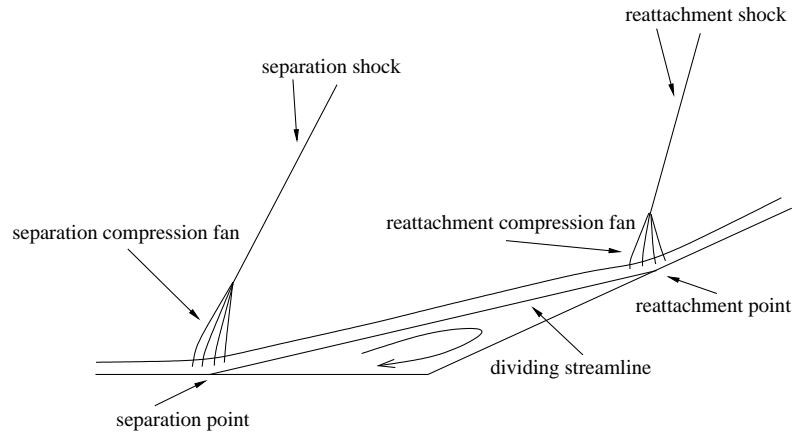

Figure 2.4: Viscid flow field over a separated compression corner

emerge from the compression corner to reach the appropriate deflection of the flow. However there is a boundary layer present near the wall. Due to the no-slip condition at the wall also a subsonic sublayer is involved. Through this subsonic sublayer information may be transmitted upstream and the oncoming flow may feel the effect of the deflected ramp in advance. With a moderate compression corner angle, a weak shock wave may extend into the boundary layer (the shock's strength and inclination changes due to the Mach number gradient) but it must vanish within the supersonic part of the flow. Due to the upstream compression corner the subsonic part of the boundary layer will encounter a continuous pressure rise, which is bound to cause the streamlines to diverge and thickens the subsonic sublayer. This divergence will locally influence the outer hypersonic/supersonic stream causing a formation of a system of compression waves which will eventually coalesce onto a single oblique shock. For a modest compression corner angle, the resulting weak interaction will be contained within a relatively small region near the compression corner.

As the compression corner angle is increased, the oncoming boundary layer faces an increasing adverse pressure gradient, until it can no longer withstand it and separates. In this case, the upstream influence of the compression corner is enlarged and the shock structure becomes significantly distinct from the inviscid case.

The recirculation bubble which is formed in well separated cases is bounded by a separation shock upstream of the compression corner and a reattachment fan which is created when the shear layer approaches the reattachment point and is gradually deflected to turn parallel to the flare surface. The compression fan will gradually converge into a reattachment shock. Both the separation and reattachment shock will merge at some distance from the flare into a single stronger shock which is equal to the inviscid wedge shock.

Downstream of reattachment the boundary layer will reach a minimum thickness in the "neck" region, where peak heating occurs.

2.3.3 Typical pressure distribution

The typical pressure distribution of a wedge type separation is shown in figure 2.5. Estimations
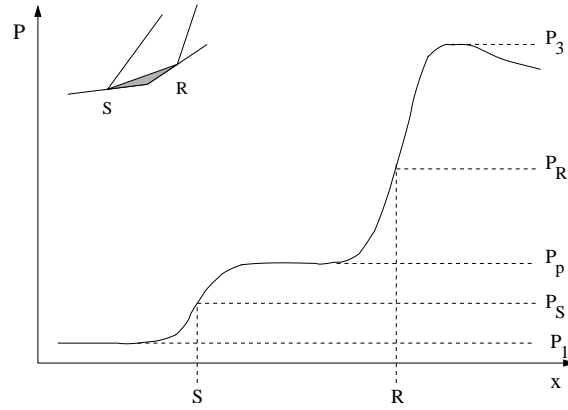

Figure 2.5: Typical pressure distribution over a compression ramp

from schlieren pictures indicate that the separation point coincides with the first inflextion point in the pressure distribution; the exact determination of its location is very difficult experimentally [31]. After separation S the pressure gradient starts to decrease until, when the separated region is large enough, a constant "plateau" pressure p_p is reached where the free shear layer is straight. Before reattachment R the pressure starts to rise steeply, the gradient exceeding that at separation, and reaches a peak downstream of reattachment.

2.3.4 Typical heat transfer distribution

In figure 2.6 a typical heat transfer distribution is depicted. When starting at the nose and proceeding further downstream a gradual decrease in heat transfer is noticed, this is due to the normal laminar or turbulent boundary layer development, see equations (2.16) and (2.17). Due to the pressure rise caused by the compression ramp the boundary layer will separate and a significant drop in heat transfer is noticed, according to Chapman [10] a characteristic drop is about 60 %. As can be seen from the figure, the heat transfer does not drop to zero because it is still heated by the hot flow in the separated region. At the compression ramp the flow reattaches again causing the boundary layer thickness to decrease and the heat transfer reaches a peak just downstream, see section 2.3.5 for the peak heating correlations.

2.3.5 Compression ramp correlations

Chapman et al [11] experienced that certain characteristics of separated flows did not depend on the object shape or on the mode of inducing separation. Any phenomenon near separation which is independent of object shape would not depend on geometric boundary conditions which describe the flow downstream, but would only depend on the simultaneous solution of the flow equations in the boundary layer together with the flow equations in the flow external to the boundary layer. Flows that are free from direct influences (although not free from indirect influences) of downstream geometry, and are free from complicating influences of the mode of inducing separation are termed "free interactions".
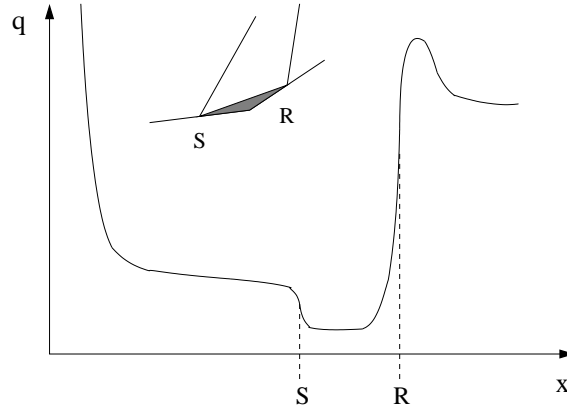
Figure 2.6: Typical heat transfer distribution over a compression ramp

Plateau pressure   In a well-enough developed separated region a pressure plateau exists. Using the free interaction concept a correlation for this plateau pressure can be developed [11], [17] and [37]:

$$\frac{p - p_o}{q_o} = f\left(\frac{x - x_o}{L}\right)\sqrt{2c_{f,o}}\left\{M_o^2 - 1\right\}^{-1/4}. \tag{2.19}$$

Where the subscript o denotes the conditions at the beginning of the interaction. f is a universal function independent of Mach and Renolds number influences. In Mallinson et al [28] the pressure coefficient at separation is given as:

$$\frac{p_o - p_\infty}{q_o} = k\left\{Re_{x_o}\left(M_o^2 - 1\right)\right\}^{-1/4} \tag{2.20}$$

where k is a constant of proportionality. Various investigators found this constant to lie around 1. This equation in fact is a further simplification of equation (2.19). From the correlations can be seen that the plateau pressure increases with increasing Mach number and decreasing Reynolds number.

Incipient separation   The incipient separation angle for a sharp flat plate, θ_i, is given by [31], [38]:

$$M_\infty \theta_i \approx 80\bar{\chi}_L^{1/2}. \tag{2.21}$$

Where $\bar{\chi}_L$ is the value of $\bar{\chi}$ evaluated at the compression corner $(x = L)$, and θ_i is in degrees. From the correlation can be concluded that the incipient angle increases with Mach number and decreases with Reynolds number except for transitional cases. For turbulent cases, the appropriate turbulent viscous interaction parameter $\bar{\chi}_{turb}$ becomes important. In [23] and [22] Holden studied incipient separation and found that for a blunted flat plate-wedge the phenomenon was governed by the parameters

$$M\theta_i\left(\frac{\kappa_{\epsilon,L}}{\bar{\chi}_{\epsilon,L}^2}\right), \frac{\bar{\chi}_{\epsilon,L}}{\kappa_{\epsilon,L}^{2/3}} \text{and} \frac{\kappa_{\epsilon,L}}{\bar{\chi}_{\epsilon,L}^2}.$$

The measurements for a blunted flat plate-wedge conducted by Holden correlated by:

$$M\theta_i\left(\frac{\kappa_{\epsilon,L}}{\bar{\chi}_{\epsilon,L}^2}\right) = 4.34\left(\frac{\bar{\chi}_{\epsilon,L}}{\kappa_{\epsilon,L}^{2/3}}\right). \tag{2.22}$$

Separated length In Simeonides [38] is given that the upstream influence length of a two-dimensional shock wave boundary layer interaction over a adiabatic wall should be correlated by:

$$\frac{L_o}{\delta_o} Re_{\delta_o}{}^a = f(\theta_{fl}, M_\infty).$$

In Delery et al [17] experiments have shown that if the streamwise extent of the interaction is scaled by the boundary layer thickness, there is still Reynolds number dependence (the exponent a is finite). This indicates that boundary layer thickness alone cannot represent the scale of the interaction.

Despite many attempts to correlate the extent of the separated region and shock wave boundary layer interactions in terms of the geometry and the oncoming flow conditions, these have had limited succes and no generally accepted correlations are available yet. In [37] two correlations are given, the first is based on theoretical considerations

$$\frac{L_{sep}}{x_o} M_\infty^3 \left[\frac{p_3}{p_p} \right]^{-2} \propto Re_{x_o}{}^{1/2} \tag{2.23}$$

and the second is based on computational work on two-dimensional shock wave boundary layer interactions

$$\frac{L_{sep}}{\delta_{L,corner}^*} \frac{M_\infty^3}{(Re_{L,corner}/C)^{1/2}} = 4.4 \left(\frac{p_3 - p_p}{p_o} \right) \tag{2.24}$$

The behavior of the extent of separation with the Reynolds number is highly dependent on the nature of the interaction (wether the flow is laminar, turbulent or transitional at reattachment). For both laminar and turbulent interactions the extent of separation increases with the Reynolds number while for transitional flows the extent decreases with increasing Reynolds number [21], [11], [23]. The empirical correlation for the separation extent presented by Needham and Stollery [31] reads

$$\frac{L_{sep}}{x_o} \propto \left[\frac{p_3}{p_p} \right]^2 \frac{1}{M_\infty^3} \tag{2.25}$$

As has been stated before, transition is an important aspect regarding the separation extent. In Heffner et al [21] a correlation is given which links the transition length with the separation length:

$$\frac{L_{sep} M_\infty^{3/2}}{\Delta x_{tr}} \propto \sqrt{p_3/p_1}. \tag{2.26}$$

Heffner et al compared the correlation with experimental values and found a general agreement but the choice of Δx_{tr} remained obviously critical.

Peak heating As the boundary layer reattaches, peak heating occurs. In Hung and Barnett [26] peak heating correlations were obtained for laminar, transitional and turbulent interactions. The reference Stanton number is evaluated at the same streamwise location for an identical geometry but without compression ramp. For a laminar interaction, the peak Stanton number is given by:

$$\frac{c_{h,peak}}{c_{h,(ref,lam)}} = 0.13 \left(\frac{p_3}{p_1} \right)^{1.13}. \tag{2.27}$$

For a transitional interaction (laminar at separation and turbulent or transitional at reattachment), the relation becomes:

$$\frac{c_{h,peak}}{c_{h,(ref,lam)}} = 0.468 \left[Re_{L,corner} \times 10^{-6} \right]^{1.85} \left(\frac{p_3}{p_1} \right)^{1.13}. \tag{2.28}$$

The peak heat transfer for a turbulent interaction is given by:

$$\frac{c_{h,peak}}{c_{h,(ref,lam)}} = \left(\frac{p_3}{p_1} \right)^{0.8}. \tag{2.29}$$

In these correlations p_3/p_1 is the inviscid pressure rise due to the inviscid oblique shock wave emerging from the cone-flare junction.

Simeonides [38], [37] developped a more elaborate theory for the (peak) heating. The theory is based on the reference temperature method mentioned in section 2.2.1; differently written, the Stanton number is given by:

$$c_h \left(Re_x\right)^n = \frac{A}{s} \left[\frac{u_e p_e}{u_\infty p_\infty} \right]^{1-n} \left[\frac{T_\infty}{T^*} \right]^{1-2n} (C^*) \left[\frac{T_{aw} - T_w}{T_t - T_w} \right] \tag{2.30}$$

where $n = 0.5, A = 0.332$ and $s = Pr^{2/3}$ for a laminar boundary layer, and $n = 0.2, A = 0.0296$ and $s = 1$ for a turbulent boundary layer at high Mach numbers. The Stanton number at peak heating can now be estimated by placing the virtual origin of the developing boundary layer at the location of the peak ramp pressure. This Stanton number can now be compared with a reference state, a flat plate with the boundary layer origin at the sharp leading edge, and a theoretically based correlation is obtained:

$$\frac{c_{h,peak}}{c_{h,ref}} = B \left[Re^*_{x_{peak}} \right]^a \left[\frac{p_{peak} u_{peak}}{p_{ref} u_{ref}} \right]^{1-n} \left[\frac{x_{peak}}{L_{peak}} \right]^n . \tag{2.31}$$

with $a = 0$, $B = 1$ and $n = 0.5$ for fully laminar interactions with a laminar reference level, $a = 0$, $B = 1$ and $n = 0.2$ for fully turbulent interactions with a turbulent reference level, and $a = 0.3$, $B = 0.072$ and $n = 0.2$ for turbulent peak heating with a laminar reference level.

The length scale L_{peak}, which is the effective growth length of the boundary layer can be approximated by:

$$L_{peak} = \frac{\delta_r}{\sin(\theta_{fl} - \theta_{sep})}. \tag{2.32}$$

When the velocity ratio is neglected an error of the order of 10% is induced. When also fully laminar or fully turbulent interactions are regarded and x_{peak}/L_{peak} is in the order of one, the correlations of Hung and Barnett are obtained.

2.3.6 Bluntness effects

In the current experiments a blunted model is used while the correlations discussed before only apply for sharp nose configurations. For a sharp nose configuration the viscous interaction is a governing process for the flow development (displacement-dominated regime). For a highly blunted nose this interaction can be neglected and the entropy layer (which is a layer of high temperature, rotational low density gas) becomes an important aspect of the flow (bluntness-dominated regime). When recalling the "free interaction" concept it is clear that the governing flow process has considerable influence on the separation and reattachment mechanism.

In [22] and [23] Holden studied the effect of leading edge bluntness on the compression corner interaction from the displacement- to bluntness-dominated regime. From section 2.1.2 it was concluded that the current experiments are conducted in the bluntness-dominated regime. From a simple flow model already some effects of blunting can be identified. Due to the introduction of bluntness the magnitude of the favourable pressure gradient is increased upstream of the compression corner and, consequently, reduces the boundary layer thickness. The Mach number at the boundary layer edge is greatly reduced and although the pressure is increased due to the blunting, the increase in temperature (due to the normal shock wave at the nose) reduces the density and the local Reynolds number.

Although the favourable pressure gradient together with the lower local Reynolds number tend to stabilize the attached layer, the locally lower Mach number is a strong destabalizing influence so the effect of bluntness on incipient separation is difficult to predict. For blunted cones a pressure undershoot near the nose can occur [7], causing an adverse pressure gradient for a finite distance. From literature ([25], [20], [29], [23] and [22]) it is found that when increasing the leading-edge bluntness the plateau pressure decreases due to the lower local Mach number. The incipient separation slightly decreases although the effect is weak. Increasing the bluntness causes the the

reattachment point to move downstream creating a larger separated region. Due to the presence of the entropy layer the pressure loss increases and a slower recompression over the flare results in attached flow. In general the skin friction and the heat transfer on the flare decreases; these distributions no longer exhibit a local maximum on the wedge. Due to the interaction with the compression of the entropy layer on the flare many of the features of the reattachment compression process which are present on sharp flat plate models are masked.

Chapter 3

Experimental apparatus

3.1 Hypersonic Test Facility Delft

The HTFD is a Ludwieg tunnel; in a long tube with a constant cross section, a gas is stored under high pressure and temperature (p_0 and T_0). The tube is closed on one end and connected to a vacuum tank through a fast closing valve, a laval nozzle and a measuring section. When the valve is opened, the pressurized air expands through the nozzle into the measuring section. The expansion wave which is formed when the valve is opened travels into the storage tube. The constant flow conditions which are different from the storage conditions P_0 and T_0 behind the expansion wave determine the reservoir conditions for the flow through the nozzle. When the expansion wave hits the closed end of the tunnel, it is reflected and runs back toward the nozzle. When the wave reaches the nozzle the maximum running time is reached.
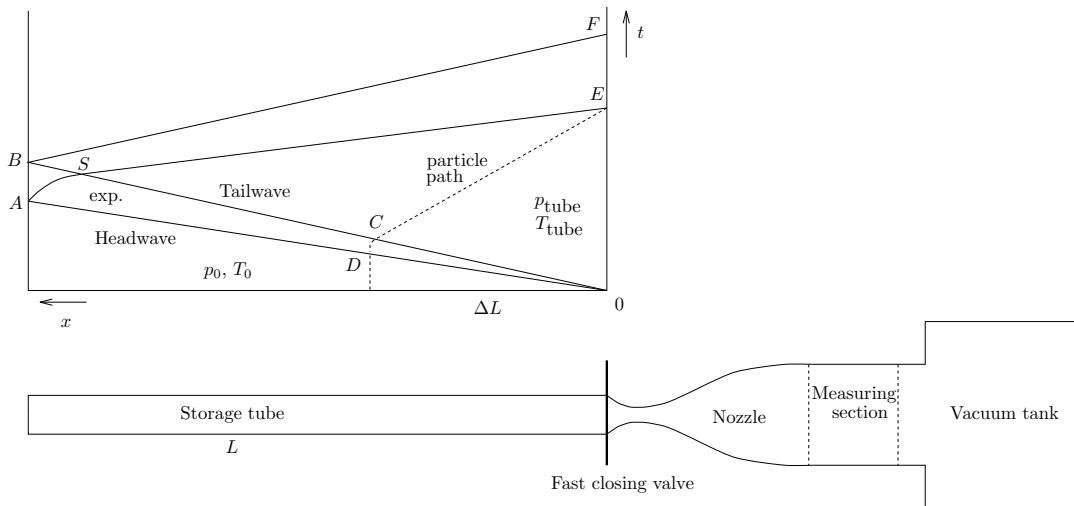

Figure 3.1: Operation principle of the Ludwieg tube

3.1.1 Flow process

If the valve is opened very quickly, the flow process can be described using "simple wave" theory. In that case a centered wave expansion wave is developed in the supply tube. According to simple wave theory the propagation speed of the expansion wave with respect to the tube is given by the

slope of the Γ^- characteristics:

$$\frac{\mathrm{d}x}{\mathrm{d}t} = u - a, \tag{3.1}$$

u and a are respectively the local speed and the local speed of sound in the gas. To determine the conditions behind the expansion wave, the Riemann-invariant theory for right-running characteristics is used:

$$u_b + \frac{2a_b}{\gamma - 1} = \frac{2a_0}{\gamma - 1} \tag{3.2}$$

Here γ is the ratio of the specific heats $\left(\frac{c_p}{c_v}\right)$ and a_0 is the speed of sound in the storage tube with undisturbed gas. This equation can be rewritten as:

$$\frac{a_b}{a_0} = \sqrt{\frac{T_b}{T_0}} = \frac{1}{1 + \frac{\gamma-1}{2}M_b} \tag{3.3}$$

and

$$\frac{p_b}{p_0} = \left(\frac{T_b}{T_0}\right)^{\frac{\gamma}{\gamma-1}} = \frac{1}{\left(1 + \frac{\gamma-1}{2}M_b\right)^{\frac{2\gamma}{\gamma-1}}} \tag{3.4}$$

Where $M_b = \frac{u_b}{a_b}$ is the Mach number in the stationary tube flow behind the expansion wave, which is determined by the contraction ratio of the nozzle. Under the assumptions that the flow through the nozzle is stationary and isentropic during the run, the mass flow in the tube must be equal to the mass flow in the nozzle throat:

$$\frac{A_b}{A^*} = \frac{1}{M_b}\left[\frac{2}{\gamma+1}\left(1 + \frac{\gamma-1}{2}M_b^2\right)\right]^{\frac{\gamma+1}{2(\gamma-1)}} = \frac{d_b^2}{d^{*2}} \tag{3.5}$$

For Mach 9 the largest diameter ratio exists (for lower Mach numbers a tandem nozzle is used). With a tube diameter of $d_b = 49.25\ mm$ and a critical diameter $d^* = 19.35\ mm$, a tube Mach number of $M_b = 0.09$ results. The reservoir conditions can be calculated using (3.3), (3.4) and isentropic relations:

$$\frac{T_{t_b}}{T_0} = \frac{T_{t_b}}{T_b} \cdot \frac{T_b}{T_0} = \frac{1 + \frac{\gamma-1}{2}M_b^2}{\left(1 + \frac{\gamma-1}{2}M_b\right)^2} \tag{3.6}$$

$$\frac{p_{t_b}}{p_0} = \frac{p_{t_b}}{p_b} \cdot \frac{p_b}{p_0} = \left\{\frac{1 + \frac{\gamma-1}{2}M_b^2}{\left(1 + \frac{\gamma-1}{2}M_b\right)^2}\right\}^{\frac{\gamma}{\gamma-1}} \tag{3.7}$$

From (3.6) and (3.7) the loss of total quantities can be calculated. For $M_b = 0.09$ a total pressure loss of $p_{t_b}/p_0 = 0.888$ and a total temperature loss of $T_{t_b}/T_0 = 0.967$ results. As can be seen from the equations, the losses of the total quantities only depend on the diameter ratio, they remain constant irrespective of the pressure and temperature settings of the storage tube

The maximum duration of constant reservoir properties in a certain area in the storage tube can be calculated using shock tube theory, [19]:

$$t_1 = \frac{L}{a_0}\frac{2}{1 + M_b}\left(1 + \frac{\gamma-1}{2}M_b\right)^{\frac{\gamma+1}{2(\gamma-1)}} \tag{3.8}$$

Where L is the total length of the tube. The maximum measuring time depends on the hot tube temperature through the speed of sound $a_0 = \sqrt{\gamma R T_0}$. For a tube length $L = 29\ m$ and a hot tube temperature of $T_0 = 773\ K$, t_1 has a maximum of 0.101 s.

Due to the high Mach number the water vapour, the oxygen and the nitrogen tend to condensate so the air in the storage tube must be pre-heated. When the air is pre-heated the speed of sound in the storage tube increases and the run-time of the tunnel is decreased. To overcome this disadvantage only that part of the air is heated which is actually used during the measurement. The heated

length of the tube can be determined from figure 3.1 where point D practically coincides with point C. If ΔL represents the last air-particle which can reach the nozzle within time t_1, ΔL can be calculated by:

$$\Delta L = \frac{u_b \left(a_b - u_b \right)}{a_b} t_1 = \frac{M_b \left(a_b - u_b \right)}{a_0} 2L.$$ (3.9)

With equation (3.3) and from the fact that $M_b < 0.1$, so that

$$\left| \frac{u_b - a_b}{a_b} \right| < 0.9$$

This results in $\frac{\Delta L}{L} < 0.18$, with $L = 29\ m$ this indicates a mass-outflow from the storage tube over a maximum length of $5.22\ m$.

If only one part of the tunnel is heated and the other part is kept on a lower temperature to increase the run-time, the expansion wave will be reflected at the temperature discontinuity. This effect can be canceled out by a change in cross section according to:

$$\frac{d_{\text{hot}}}{d_{\text{cold}}} = \left(\frac{T_{\text{hot}}}{T_{\text{cold}}} \right)^{\frac{1}{4}}$$ (3.10)

In figure 3.2 the measured reservoir pressure development in time is depicted. As the valve is opened, the storage pressure drops due to creation of the centered expansion wave. From equation
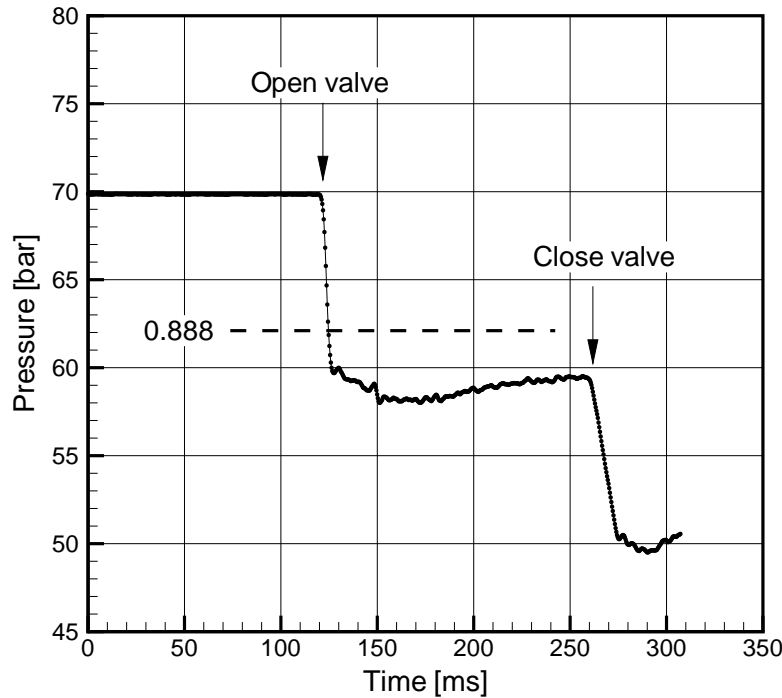

Figure 3.2: Storage tube pressure development for a single shot

(3.4), the theoretical pressure drop can be calculated. For $M_b = 0.09$ the predicted pressure drop becomes $p_b/p_0 = 0.888$, although a larger pressure drop is observed in figure 3.2. This is probably due to two dimensional effects in the tube. For data reduction, still the total pressure drop

$p_{t_b}/p_0 = 0.888$ is used as well as the previously obtained total temperature drop $T_{t_b}/T_0 = 0.967$. At the start of the pressure time history the reflection of the expansion wave at the cross-sectional discontinuity can be seen.

3.1.2 Tunnel calibration

The HTFD has been calibrated for the Mach 9 conical nozzle [6]. The raw Mach numbers calculated in [6] were calculated from pitot tube measurements using the storage tube pressure as reservoir pressure (the drop in total pressure due to the expansion wave was not taken into account). From these calibrations it appeared the mean Mach number was 9.37. To correct for the total pressure drop, the mean Mach number is calculated back to pitot pressure ratio. This pressure ratio is subsequently corrected and used to determine the corrected Mach number. The correlation between the Mach number and pressure ratio can be obtained through the normal shock-wave relations:

$$\frac{P_{\text{pitot}}}{P_t} = \left(\frac{(\gamma+1)M^2}{2+(\gamma-1)M^2} \right)^{\frac{\gamma}{\gamma-1}} \cdot \left(1 + \frac{2\gamma}{\gamma+1} \left(M^2 - 1 \right) \right)^{\frac{-1}{\gamma-1}} \tag{3.11}$$

where M is the Mach number, P_{pitot} is the pitot pressure and P_t is the total pressure. The corrected Mach number appeared to be 9.13, which was also used for all subsequent data reductions. The Mach number slightly varies in streamwise direction due to imperfections in the conical nozzle. This variation is approximately $\frac{\mathrm{d}M}{\mathrm{d}x} \approx 0.024 \ cm^{-1}$. In terms of a model length of 132 mm this is a Mach number increase of 0.32, a deviation of 3.5 %. The Mach number variation perpendicular to the flow is less than 2 %.

Because the Mach number is quite high and the total temperature is relatively low, the static temperature will drop to about 45 K. In order to prevent condensation, all the water is extracted from the air. Under normal conditions even the air itself would liquify. This won't happen because the run times of the tunnel are extremely short, so the air doesn't get the chance to condensate and it remains a strongly under-cooled gas.

This illustrates that preferably the total temperature should be as high as possible, which has a drawback since this decreases the maximum attainable Reynolds number. Using these two considerations a total temperature of 773.15 K (500 $^{\circ}C$) was chosen.

3.2 Model description

The model, which is used in the experiments, is based on the DART vehicle concept. The cone and the flare are made of plastic (see below) and the nose is made of metal. The same model is used for both heat transfer and schlieren measurements. Both a clean and a rough nose were tested, the roughness was obtained by gluing three rings to the nose of the model.

3.2.1 Geometry

The model dimensions are governed by the size of the wind tunnel, it is a blunted cone flare which has a total length of 131.9 mm, the cone and flare angles are respectively 15° and 30°. The metal nose has a radius of 12.7 mm, see figure 3.3. To increase the surface roughness three metal rings were added. The rings were made of 0.5 mm copper wire and glued to the nose with a spacing of 7 mm.

3.2.2 Material

The main body of the wind tunnel model was made in a synthetic material called makrolon. This material was chosen since it is easily obtainable and machineable, the thermal properties are favorable and it has a high enough melting temperature to withstand the flow conditions. The emissivity of makrolon is comparable to that of Plexiglas which is approximately 0.85. The exact emissivity is measured using a sample of makrolon and appears to be 0.88, see section 4.3.2.
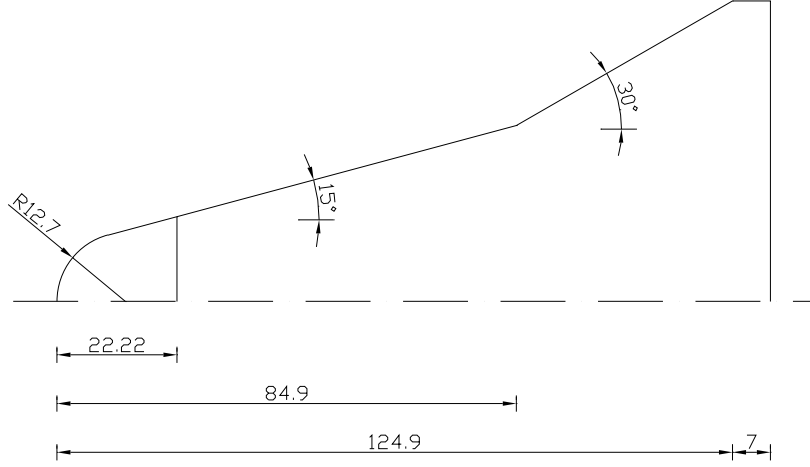
Figure 3.3: DART model dimensions

For heat transfer measurements, the thermal product $(\sqrt{\rho c k})$ and the diffusivity $\left(\alpha = \frac{k}{\rho c}\right)$ are two important parameters. The larger the diffusivity, the deeper a thermal pulse diffuses into the model within a certain time interval, in the current experiments a relatively small value is appreciated ($\leq 0.5 \ m^2/s$, [34]). The thermal product is a variable which correlates the amount of heating needed to increase the surface temperature of the model (see section 5.3.1). If the thermal product is low, relatively little heating is needed, if the thermal product is high, large heating is needed. Because the wind tunnel can produce a limited amount of heat trough the flow, the thermal product must be as low as possible in order to produce a large thermal effect, although of course care has to be taken not to exceed the melting temperature of the material.
Makrolon is a polycarbonate which has a density ρ of $1.2 \times 10^3 \ kg/m^3$, a conductivity k of $0.20 \ W/(m \ K)$ and a thermal capacity c of $1.17 \times 10^3 \ J/(kg \ K)$. This results in a thermal product of $(\sqrt{\rho c k}) = 530 \ J/(m^2 \ K \ \sqrt{s})$ and a diffusivity of $\alpha = 1.42 \times 10^{-07} \ m^2/s$.

3.3 Schlieren system

During the experiments the schlieren method was used as an additional flow diagnostic tool. The schlieren flow visualization method is based on the influence of density gradients on the deflection of light rays.

3.3.1 Light refraction

The refractive index n of air depends on the density ρ by a simple linear relationship:

$$n = 1 + K\rho \tag{3.12}$$

where K is the Gladstone-Dale coefficient. This coefficient depends on the thermodynamic state of the gas and the wave length of the light. The effect of the wave length on K is only small, for practical purposes K can be taken constant.
Using Fermat's principle (wave front is perpendicular to direction of propagation), the refraction

of light rays in non homogeneous media can be described. When this principle is applied to a density discontinuity, Snell's refraction law is obtained [35]:

$$n_1 \sin \alpha_1 = n_2 \sin \alpha_2. \tag{3.13}$$

See figure 3.4 for definition of n_1, n_2, α_1 and α_2. From this equation can be concluded that the
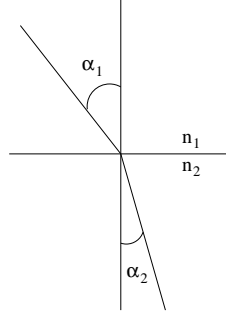

Figure 3.4: Deflection of light rays

light rays are deflected to the direction of increasing density. The total deflection of the light ray is obtained by integrating the density gradients along the light ray path.

3.3.2   Schlieren method

In figure 3.5 the basic setup of a schlieren system is reproduced. An image is formed by focusing on a plane in the flow; all the rays emanating from a point P in the focused plane converge to the image point P'. The width of the beam in the focal point of the imaging lens has finite dimensions
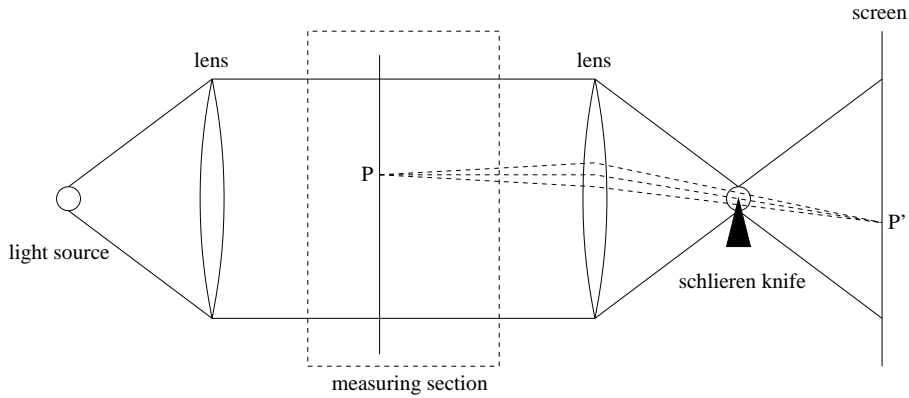

Figure 3.5: Operation principle of the schlieren method

because an image of the light source is created. In this focal point a schlieren filter is placed. The most simple form for this filter is a schlieren knife, a thin sheet of nontransparent material placed perpendicular to the light beam axis. When using the configuration shown in figure 3.5, with the knife edge normal to the plane of drawing, the lower rays originating from point P will be blocked by the schlieren knife. This results in a reduced illumination in the point P' on the screen to half of the original intensity. If density gradients in the test section result in an upward deflection of the light rays, the beam in the focal plane will also be shifted upward. Now also a smaller part of the beam is cut off by the knife and a larger illumination intensity results. Inversely if the rays are deflected downward a larger part will be blocked and the illumination will decrease. Thus the

schlieren method provides an image of the total deflection angle of the rays, hence, if the gradient of the density in the direction perpendicular to the edge of the schlieren knife. When the schlieren knife is turned 90° the density gradients in the other direction are visualized. Using this type of schlieren filter only one gradient at a time can be visualized. There are a lot of different schlieren filter shapes. In the current experiments also a color filter is used. The layout of this filter is depicted in figure 3.6 together with the conventional one. When the color schlieren filter is used,
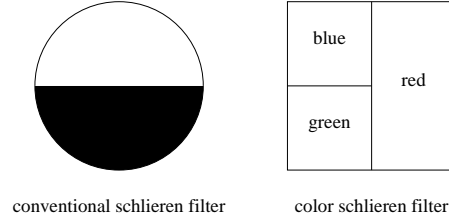
Figure 3.6: Schlieren filters

more information about the density gradients is visualized. Because the color filter has two knife edges (difference between two colors) which visualize the density gradients in two directions.

3.4 Measurement setup

The model is positioned in the wind tunnel with a steel support attached to the back, under zero angle of attack with the oncoming flow. The same model was used both for the heat transfer and the schlieren measurements. In figure 3.7 the model can be seen in the wind tunnel with the germanium window at the back.

Figure 3.7: DART in HTFD

3.4.1   IR setup

Figure 3.8 shows the setup for the infrared system. The infrared camera is placed under a slight angle with respect to the model centerline. The r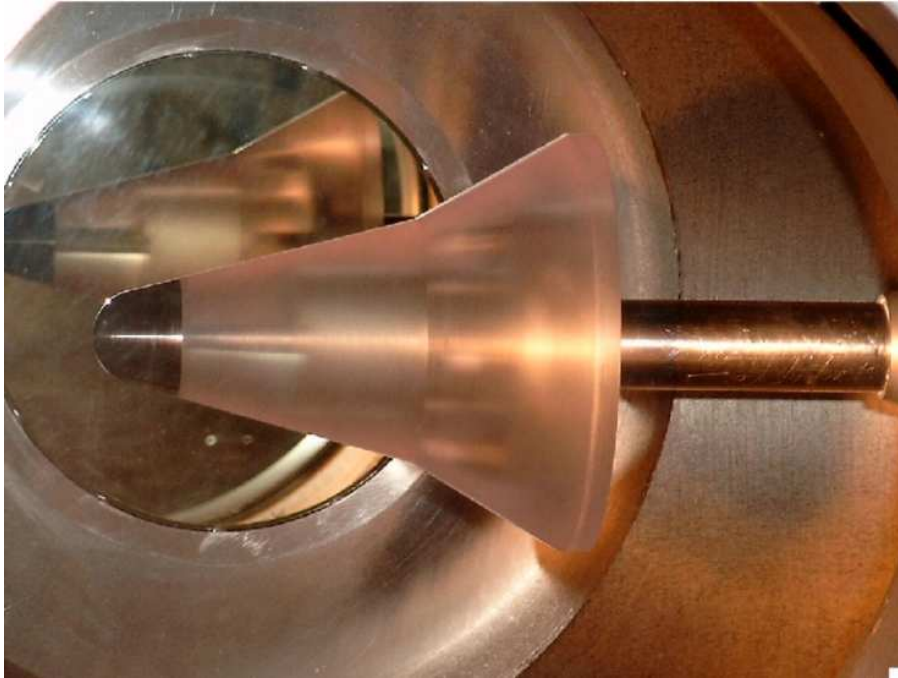eason is twofold: first the viewing angle of the camera with respect to the surface (cone and flare) of the model is minimized; secondly when the camera is placed perpendicular to the window, the camera would detect its own reflection (especially the reflection of the cold optics). The infrared camera is an Agema 880 LWB scanner
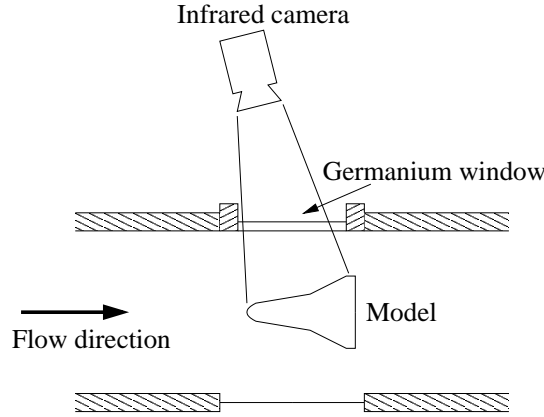

Figure 3.8: Infrared setup for HTFD

which operates in the long wave band $(8 - 12 \ \mu m)$. The camera is switched into line scan mode to achieve a high frame rate of 2.5 kHz. Each line consists of 140 pixels where the radiation intensity is digitized into a 13 bit number (see appendix D). The pixel size on the cone is 1.03 mm, on the flare it is 0.91 mm. The distance of the camera to the model was approximately 0.5 m. The NETD is 0.2 $^\circ C$ and the minimum detectable object size is 4 $mrad$ (obtained from slit response function). For more information see section 4.2.

3.4.2   Schlieren setup

The actual schlieren setup is different from the setup shown in figure 3.5. The setup used for the experiments is shown in figure 3.9. When this picture is compared with figure 3.5, lenses are replaced by parabolic mirrors as is common in large-scale wind tunnels. In fact the lenses must be of the size as the imaged area so it is cheaper to use parabolic mirrors. The mirror also enables a more compact setup of the system. The recording device is either a high speed or a digital CCD camera. The high speed drum camera consists of a disc on which film is attached that is situated inside a drum. At the front of the drum there is a magnetically controlled shutter. When performing a schlieren measurement the shutter is opened and the film is illuminated by a high speed flash system while the disc inside the drum rotates. By varying the rotational speed of the disc, the camera speed can be adjusted. In the current experiments the disc speed was 400 rpm. Each film consists of approximately 75 frames (depends on the frame size) so a frame rate of 500 Hz is obtained. Since the drum camera uses conventional films and the development of these pictures took a relative long time it was chosen to also use a digital CCD camera. The pictures obtained by the digital CCD camera were zoomed because of the limited resolution of the camera. The digital camera has a colour-CCD with a resolution of 640×480 pixels and a refresh rate of 30 fps. The images are saved in an 8 bit bitmap (`bmp`) format.
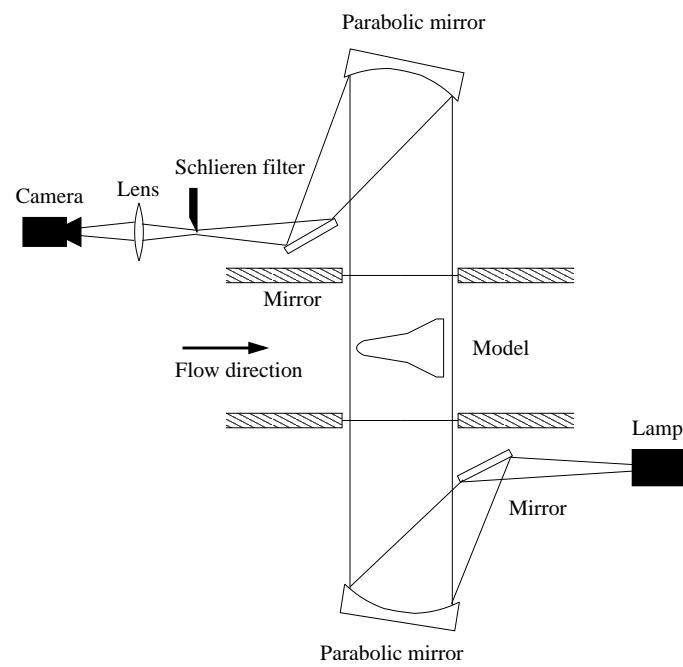
Figure 3.9: Schlieren setup for HTFD

Chapter 4

IR measurement technique

4.1 Infrared theory

The heat transfer measurements conducted in the present study were done by use of an infrared camera. The operation principle of the camera is based on the detection of radiation. In this section some important aspects regarding infrared radiation will be discussed.

4.1.1 Thermal radiation

Every surface which has a temperature above absolute zero radiates a certain amount of heat. This thermal radiation is correlated to the temperature of that surface. The spectral distribution of the radiation emitted by a black body can be described by Planck's law [27]:

$$E_{b,\lambda} = \frac{C_1}{\lambda^5 \left[\exp\left(C_2 / \lambda T_s \right) - 1 \right]}, \tag{4.1}$$

where $C_1 = 3.7415 \times 10^{-16}\ Wm^2$ called the first radiant constant and $C_2 = 1.4388 \times 10^{-2}\ mK$ called the second radiant constant. From equation (4.1) and figure 4.1 can be seen that the monochromatic radiation $E_{b,\lambda}$ $\left(E_{b,\lambda} = \frac{E_b}{\mathrm{d}\lambda} \right)$ varies with wavelength λ and the surface temperature T_s. For a real body in addition it also depends on the surface characteristics. As stated before, Planck's law is valid for a black body. A black body, or ideal radiator, is a body that emits and absorbs at any temperature the maximum possible amount of radiation at any given wavelength. When looking again at figure 4.1 and following any arbitrary Planck curve, the spectral emittance is zero at $\lambda = 0$, then increases rapidly to a maximum at a wavelength $\lambda_{\max}$ and after passing it decreases again until it approaches zero at very long wavelengths. When the temperature increases, the wavelength for maximum monochromatic emissive power decreases. The relationship between $\lambda_{\max}$ and the absolute surface temperature T_s is called Wien's displacement law

$$\lambda_{\max} T_s = 2.898 \times 10^{-3}. \tag{4.2}$$

This formula expresses the common observation that as the temperature of the radiator increases its color varies from red to orange to yellow, the color corresponds with $\lambda_{\max}$.
When Planck's law is integrated, the total emitted energy per surface area is obtained as

$$E_b = \frac{q_r}{A} = \sigma T_s^4, \tag{4.3}$$

where $\sigma = 5.670 \times 10^{-8}\ W/(m^2\ K^4)$ called the Stefan-Boltzmann constant. This equation is called the Stefan-Boltzmann law, when looking at figure 4.1, E_b represents the total area under the Planck curve for a particular temperature.
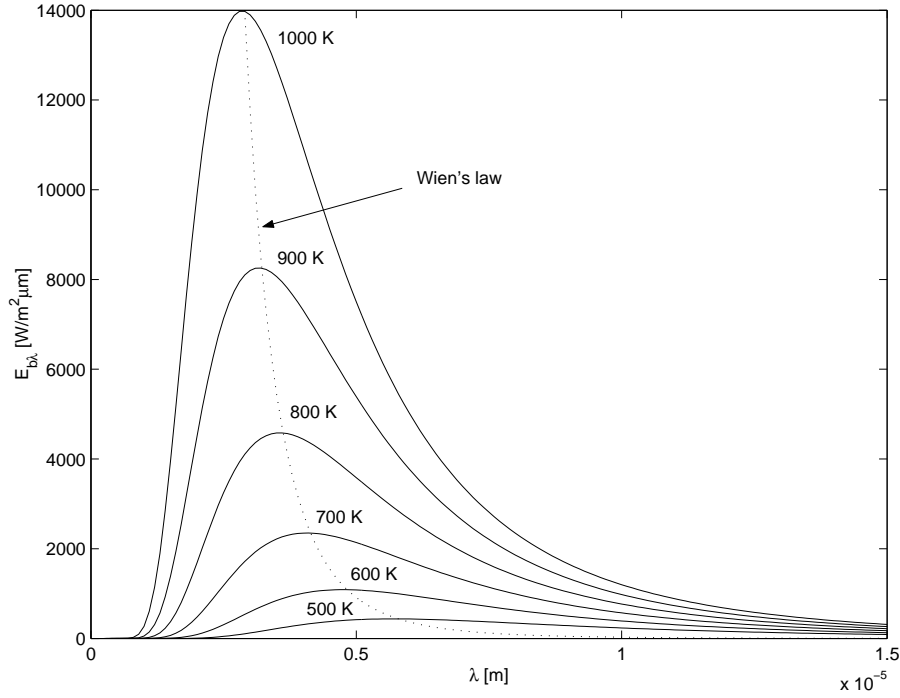
Figure 4.1: Black body spectral radiant emittance

4.1.2 Gray body radiator

In the previous section all equations were applied to black body radiators, however real objects are almost never black bodies, although they may approach black body behavior in certain spectral intervals. There are three reasons why a real body does not act as a black body; a fraction of the incident radiation α may be absorbed, a fraction ρ may be reflected and a fraction τ may be transmitted. Since all these factors are more or less wavelength dependent, the subscript λ is used to indicate the spectral dependence.

The sum of these three factors must always add up to unity at any wavelength (since radiation cannot be destroyed)

$$\alpha_\lambda + \rho_\lambda + \tau_\lambda = 1. \tag{4.4}$$

The amount of radiation emitted by a surface at a certain temperature can be correlated to the radiation emitted by a black body at the same temperature by the emissivity ϵ_λ using a linear relationship

$$\epsilon_\lambda = \frac{E_{o,\lambda}}{E_{b,\lambda}}. \tag{4.5}$$

As can be seen from the definition, the emissivity depends on the wavelength. If this really is the case the object is called a selective radiator, else if $\epsilon_\lambda = \epsilon < 1$ and constant, the object is called a gray body.

According to Kirchhoff's law, for any material the spectral emissivity and spectral absorptance are equal for any specified temperature and wavelength; $\epsilon_\lambda = \alpha_\lambda$.

Since a gray body has a constant spectral emissivity, its total emitted radiation can be correlated to the total radiation emitted by a black body using the Stefan-Boltzmann equation (4.3)

$$E = \epsilon\sigma T_s^4. \tag{4.6}$$

Using this equation and Kirchoff's law ($\epsilon = \alpha$) the net radiant energy transfer of the surroundings to or from a gray body at a certain temperature can be calculated. The radiated energy by the

gray body is

$$E_r = E_o - E_a = \epsilon_o \sigma \left(T_o^4 - T_a^4 \right). \tag{4.7}$$

4.1.3 Real surface characteristics

In the previous section it was stated that the emissivity is a function of the wavelength, but it also depends on the temperature and the shape of the object itself. The influence of temperature is twofold: first if the temperature of the radiating source changes also its emissivity changes, see figure 4.2. Secondly, if the temperature of a source object changes also the absorptivity of the irradiated object will change (change in wavelength due to temperature differences, see figure 4.3)
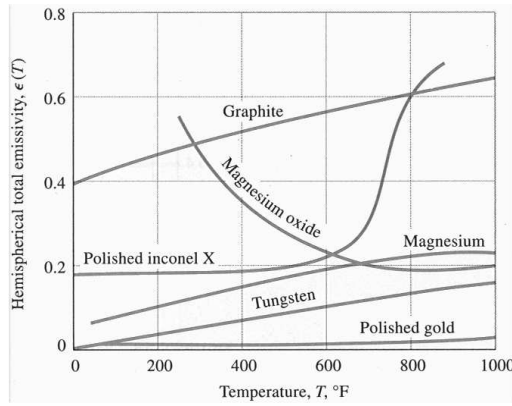

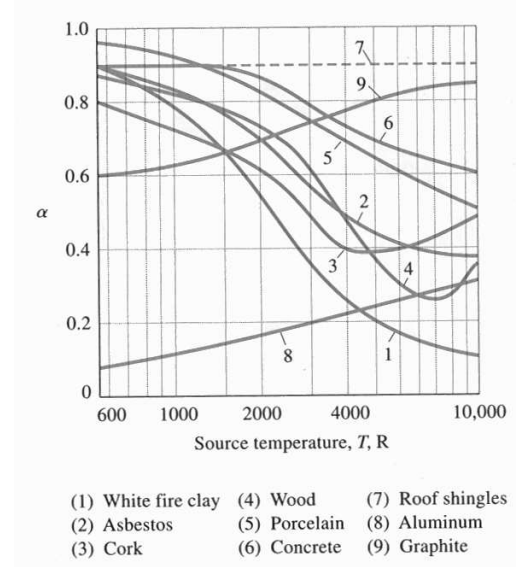Figure 4.2: Effect of temperature on hemispherical total emissivity of several metals, taken from [27]

Figure 4.3: Variation of total absorptivity with source temperature for several materials at room temperature, taken from [27]

In addition to the temperature factors described above, the emissivity also depends on the optical angle of incidence (shape of the surface). The relation between the emissivity and the optical angle ϕ is highly dependent. The polar plots taken from [27] shown in figures 4.4 and 4.5 illustrate the directional emissivity for some electrical non-conductors and conductors.

In these plots θ is the angle between the normal and the direction of the radiant beam emitted from the surface. If the emissivity is independent of the optical angle, the emissivity curves would be semi-circles. Figure 4.4 shows that for nonconductors such as wood, paper and oxide films the emissivity decreases at large values of the emission angle θ, whereas for polished metals the opposite trend is observed (see figure 4.5).

4.1.4 Environmental disturbances

Next to the fact that real surfaces are not ideal black bodies, also the surroundings affect the transfer of radiation. In the previous section it was assumed that the radiation was passing through a vacuum without any nearby bodies. However in reality this is not the case since the radiating body is in contact with the surrounding and is placed in a room with the infrared sensor.
Unless special precautions are taken (vacuum chamber) the surrounding air will reflect and absorb radiation. The magnitude of the disturbances are influenced by a lot of factors, for example: air temperature, air pressure, chemical composition of the air, amount of particles in the air, distance covered by the radiation. Most of these parameters can be neglected at standard conditions.
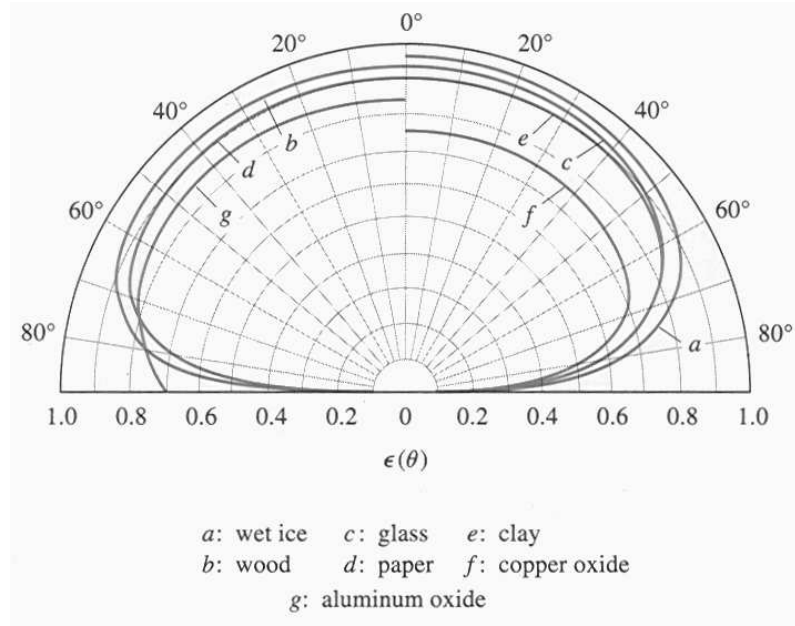
Figure 4.4: Variation of directional emissivity for several electrical nonconductors, taken from [27]
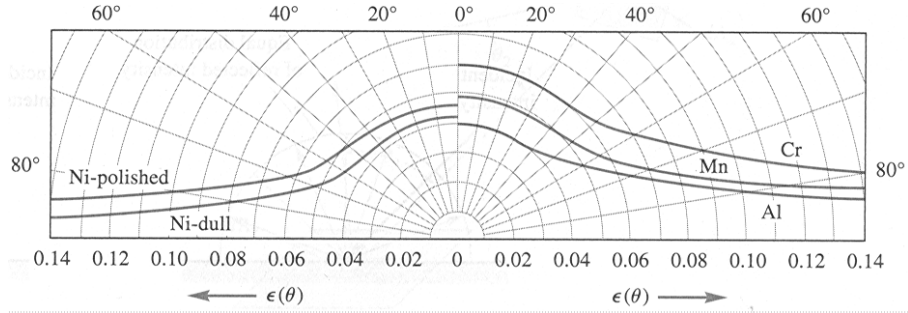

Figure 4.5: Variation of directional emissivity for several metals, taken from [27]

However there are two exceptions; the distance covered by the radiation and the chemical components H_2O and CO_2. When there are no reflective particles in the air the reflectivity can be assumed zero. So equation (4.4) for air now becomes: $\alpha_{\mathrm{air}} + \tau_{\mathrm{air}} = 1$. Water vapor and carbon dioxide absorb energy at certain wavelengths in the infrared spectrum, this leads to a decrease in transmissivity. Wavelength areas of reduced transmissivity can be seen in figure 4.6.

The region up to the wavelength ≈ 5 μm is mainly influenced by the absorbing affect of CO_2. Air is nearly opaque between 5 and 8 μm, this is caused by the water vapor in the air. Wavelength regions of high transmissivity are called atmospheric windows. Especially for radiation measurements over long distances (> 10 m) it is important to operate within these atmospheric windows. For this reason most infrared detectors operate in two distinct bands:

>   —   Short Wave Band (SWB) 3 μm — 5 μm,
>   —   Long Wave Band (LWB) 8 μm — 12 μm.

The choice of the sensor depends on the expected temperature range, sensitivity, detectivity, simplicity etc. When applying Wien's displacement law (equation (4.2) and figure 4.1), the maximum emissive power of objects at ambient temperature falls into the long wave band, for example a body with a temperature of 293 K emits maximum power at $\lambda_{\mathrm{max}} = 9.9$ μm.
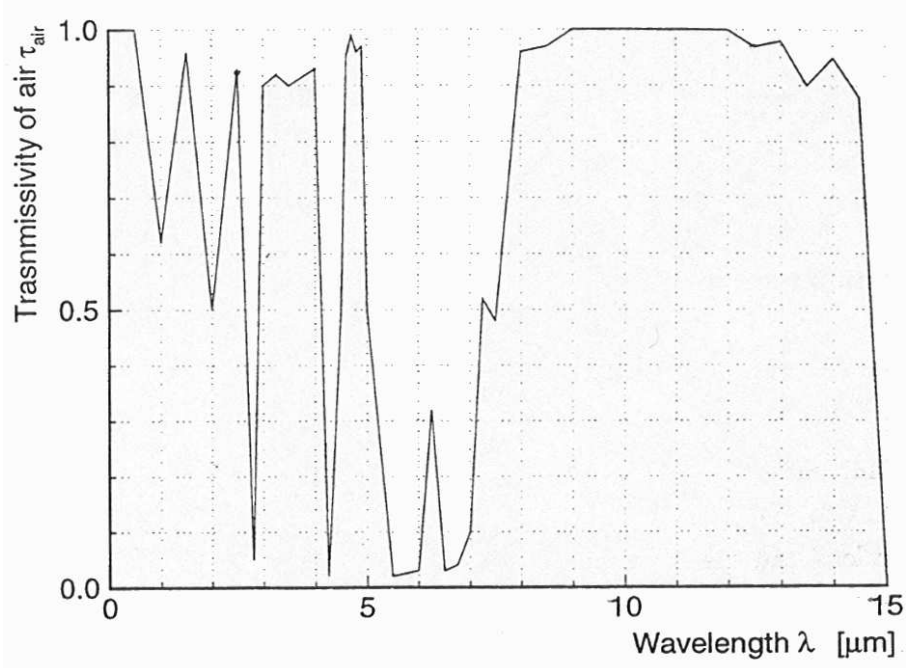
Figure 4.6: Transmissivity of air for different wavelengths (1 *atm*, 25 °*C*, 25 % relative humidity and 30 *m* distance), taken from [30].

4.2 Data acquisition system

For the surface temperature measurements an infrared camera is used. To operate the camera a computer is used, these two components form the data acquisition system. The system consists of an Agema Thermovision® 880 LWB scanner and a BRUT (Burst Recording Unit) system. In this section the most important parts of this system will be discussed; the detector, the scanning mechanism and the BRUT system.

4.2.1 Detector

Basically there are two approaches to the detection of infrared radiation. There are flux detectors; they integrate the optical signal over the complete viewing space or IFOV (instantaneous field of view) and produce a response that is a function of time (radiometry). And there are image detectors that integrate over time, so that the response is a function of the space variables (photography). The detector of flux produces a response that is a function of time and must describe the temporal evolution of the incident signal. If this temporal signal comes from the displacement of the instantaneous field of view (IFOV) seen by the detector, a system is obtained that combines the two modes of operation. An infrared imaging system can be realized, based on either of these approaches. Firstly, the imaging method can be applied directly, in which the IR object image is formed by an array of IR detectors. Alternatively, a single (flux) detector can be used where the image is formed by sequentially scanning the IFOV over the desired FOV (field of view).

There are two types of flux detectors; first there are thermal detectors, which transform the incident luminous flux into heat by absorption. The resulting temperature variation produces the output signal. Examples of thermal detectors are bolometers (conductivity change due to temperature increase), pyroelectric detectors (production of surface electric charges due to heating), thermopiles (production of a voltage due to temperature increase) and pneumatic detectors (gas expansion due to heating). Secondly there are quantum detectors, which measure the direct excitation of its electrons to conduction states by incident photons (photoelectric detectors). The

detector used in the Agema 880 LWB scanner has a HgCdTe quantum flux detector. The sensor has a spectral response of $8-12\ \mu m$ and is mounted at the bottom of a LN_2 (liquid nitrogen) filled Dewar chamber which cools the sensor to a temperature of $77\ K$. The cooling has two beneficial effects; first the cooling will induce a large temperature difference between the object and the sensor which results in a larger net radiant energy transport to the sensor (see equation (4.7)), while secondly the low temperature raises the signal to noise ratio of the sensor.

4.2.2   Scanning mechanism

Since the camera uses a flux quantum detector, the camera has to be fitted with a scanning mechanism which provides the displacement of the IFOV. In this way the scanning mechanism approximates the continuous distribution of thermal radiation of the surface inside the field of view (FOV) of the camera by a series of single measurements. Since the IFOV is not infinitely small, the sensor detects the emitted radiation integrated over the IFOV. The size of the IFOV is a function of the distance between the camera and the object and of the focal length of the utilized lens. The detected integrated radiative energy of one IFOV is converted to a single output by the AD converter. After the conversion the scanning system focuses on another IFOV and the procedure is repeated until the whole FOV is covered.
The scanning mechanism consists of two mirrors; a rotating and an oscillating mirror (see figure 4.7). The rotational speed of the mirror polygon and the sampling speed of the AD converter
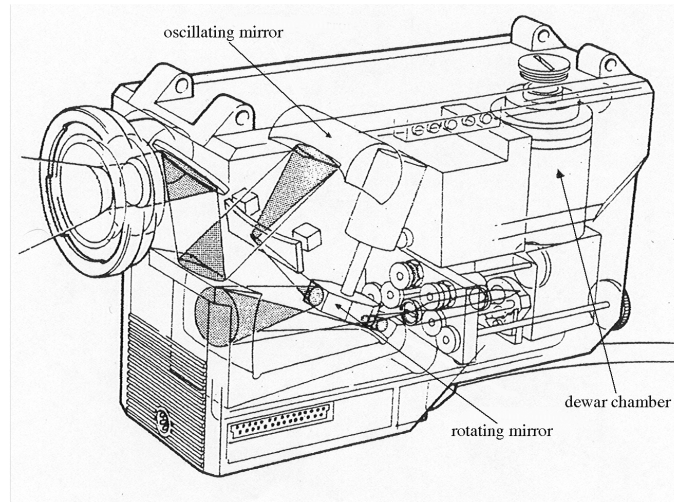
Figure 4.7: Interior of the camera

define the 140 pixels generated in the horizontal direction. The vertical scanning is determined by the frequency ratio of the oscillating and the rotating mirror. The scanning system starts at the top of the monitored area and samples 140 pixels. 100 lines are generated from the top to the bottom before the top is reached again, the group of 100 lines is called a field. Because the frequency ratio is slightly offset, the position of the second field is above that of the first field. The frequency ratio is $100.25\ Hz$, this creates a spatial shift which is exactly one quarter of the distance between two lines in one field, so four fields have to be scanned to obtain a complete frame of 400 lines (interlace mode 4:1). Due to vibrations of the oscillating mirror at the turning point only 70 lines per field can be used. In this way an effective frame of 140×280 pixels is obtained see figure 4.8. The timescales of the scanning mechanism given by the manufacturer are depicted in the following list:

Figure 4.8: Scanning path of the camera

Time per frame	160 ms	6.25 Hz
Time per field	40 ms	25 Hz
Time per line (path AB)	0.4 ms	2.5 KHz
Time per line (path BC)	0.0 ms	

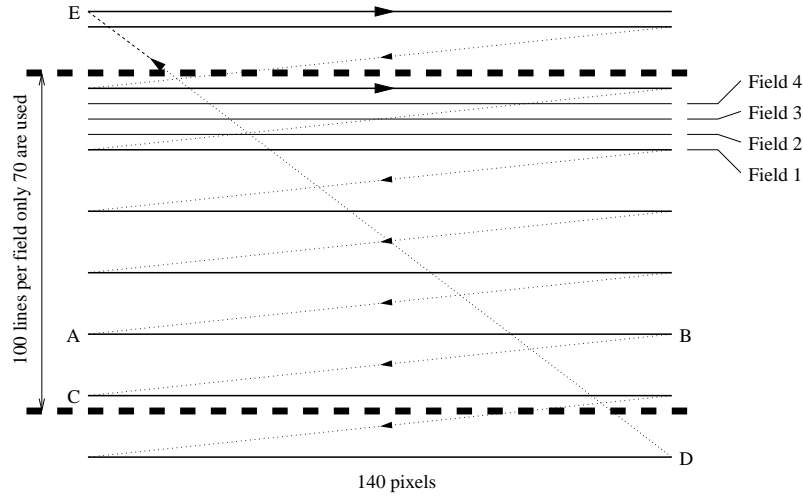**Line scan mode**   Due to its relatively low frame frequency, this system it is not capable of high speed imaging. To modify the camera for high speed imaging it is switched into line scan mode. This is done by stopping the oscillating mirror responsible for the vertical displacement of the IFOV, in this way every time the same line is sampled. This results in an imaging frequency of 2.5 KHz. Although this is a significant speed increase also a lot of spatial information is lost since only one line can be sampled.

The line scan mode could not be activated through the software of the data acquisition system so the oscillating mirror was stopped by changing a jumper setting on the servo-board of the camera. Since the data acquisition software was not equipped to handle the line scan mode it still acted as if the camera was in frame mode. So the software still omits 30 lines per field resulting in gaps in the acquired data.

4.2.3   BRUT system

The BRUT system is used to process and transfer the acquired data. The analogue video signal is first processed in the analog section then converted to digital data in the AD converter. When the system is in record mode, this digital data is continuously assembled to full frame images in the frame memory. The frames are sent through a level & range unit to the display where they are presented. Further in this mode, the completed frames are transferred to the sequence memory (RAM disk) for later playback or storage.

4.2.4   System characteristics

Noise equivalent temperature difference   Due to the fact that the mirrors of the scanning system are driven by electric motors, electrical fields are built up which may contribute to the noise in the signal of the sensor. A significant parameter to describe the influence of the noise is the "Noise Equivalent Temperature Difference" (NETD). In this quantity the total noise is expressed as an equivalent temperature difference. For the Agema 880 scanner the NETD is ±0.2 °C. This value is independent of the measured temperature so it leads to significant errors for measurements

on low temperature differences.

Slit response function   Since the IFOV has a finite size and spatial temperature gradients exist, errors are introduced due to integration of the radiation over the IFOV. In an experiment conducted by Mayer [30] the size of the IFOV for this camera was determined. During the experiment the infrared camera watches a blackbody at constant temperature through a diaphragm with an adjustable slit. By varying the slit width w, the relation between w and the measured sample value $I(w)$ can be determined. The ration between $I_{\max}$ and the actual $I(w)$ is called the "Slit Response Function" (SRF). The SRF is given by the relation:

$$\text{SRF}(w) = \frac{I(w)}{I_{\max}} \tag{4.8}$$

The sample values for different slit widths w and the resulting SRF can be seen in figure 4.9. In
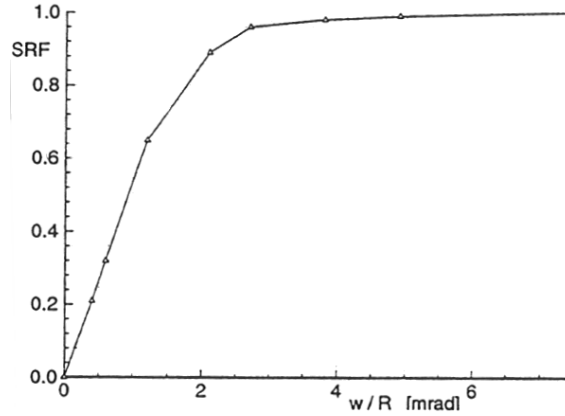

Figure 4.9: Slit response function, taken from [30]

this figure it can be seen that the camera signal $I_{\max}$ is constant as long as w is larger than the size of the IFOV. Thus from figure 4.9 can be concluded that the temperature of objects larger than 4 $mrad$ is measured with sufficient accuracy.

4.3   Calibration and emissivity measurement

To accurately measure temperatures with the infrared sensor the emissivity of the object has to be known and the camera has to be calibrated. In this section both the calibration procedure and the emissivity measurement are treated.

4.3.1   Calibration of the infrared sensor

For the calibration of the infrared camera a black body is used. The camera is calibrated by correlating the black body temperature to the output of the camera. The black body is heated to a prescribed temperature which is measured using a thermocouple and the sample value of the camera output is collected. This process is repeated for different temperatures covering a desired temperature range.

For the camera a certain correlation between the sample value and the temperature has been given by the manufacturer, which is called the calibration function. It will be used to calculate the temperatures from the sample values. The correlation for the camera is given by

$$T = \frac{B}{\ln\left(\frac{R}{I} + F\right)}, \tag{4.9}$$

where B is the scanner calibration spectral factor, F the shape factor and R is the response factor. The constants B,F and R can be used to fit the calibration function through the measured points. The fit is done using the simplex optimization principle (see section 5.5.4 and appendix C).

In order to obtain a high emissivity, the black body is shaped in a special way. In figure 4.10 a cross section of the black body is given, which consists of a circular cylinder closed at one end. The inside of the cylinder is painted black ($\epsilon \approx 0.9$) to increase the emissivity of the cylinder
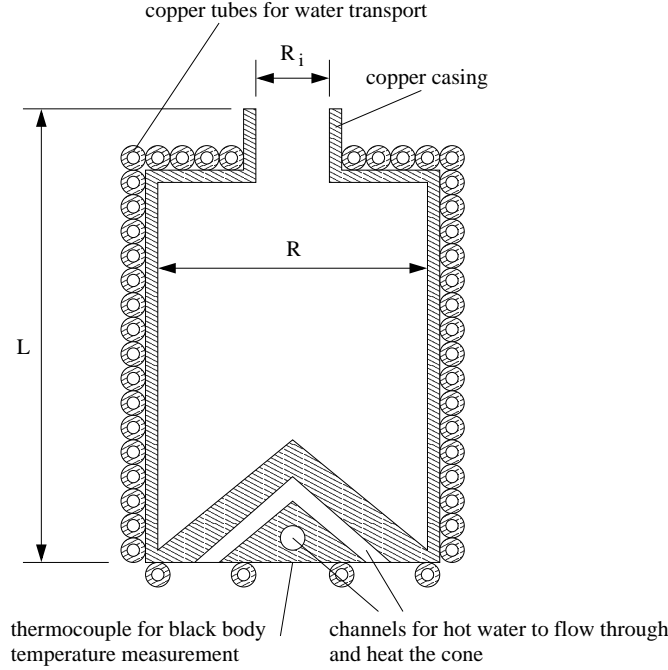

Figure 4.10: Black body layout

walls. When incident radiation strikes the wall of the cylinder, a part is absorbed and the other part is reflected. A part of this reflection is again absorbed and reflected. To obtain a black body with an emissivity of one, all the incident radiation has to be absorbed. This can be achieved by preventing radiation to be reflected out of the black body. For this reason the opening of the cylinder is narrowed. At the back of the cylinder a cone is placed to prevent the direct reflection of radiation from the flat back of the cylinder. In this configuration the opening of the cylinder approaches the behavior of a black body. The black body is heated by circulating hot water through a hollow copper coil which is wound around the outside of the cylinder to obtain a uniform heating. Two channels are drilled in the cone which are connected to the coil for faster heating of the cone. The outside of the black body is insulated with glasswool to minimize heat losses and to achieve a thermal equilibrium. When the black body is heated, following Kirchoff's law, a source of radiation is created since a perfect absorber is also a perfect emitter. In Mayer [30] the apparent emissivity was calculated for different values of the relative aperture $\left(\frac{R_i}{R}\right)$ and the length-diameter ratio $\left(\frac{L}{R}\right)$. If $\frac{R_i}{R}$ decreases then the apparent emissivity increases, the minimum size of the hole is determined by the SRF of the camera and the desire to average over a certain amount of pixels to decrease the influence of camera noise. As is expected, the emissivity also increases with increasing $\frac{L}{R}$. The black body used in the calibration has a length $L = 200 \ mm$, a cylinder diameter $R = 25 \ mm$ and an opening with a diameter $R_i = 10 \ mm$. For this geometry, according to Mayer [30], an apparent emissivity of 0.999 is achieved.

Since a germanium window is used during the experiments this is also used during the calibration, [18]. The camera monitors the radiation emitted by the black body through the germanium window, see figure 4.11. In this way the reduced transmissivity due to the germanium is incor-

Germanium window
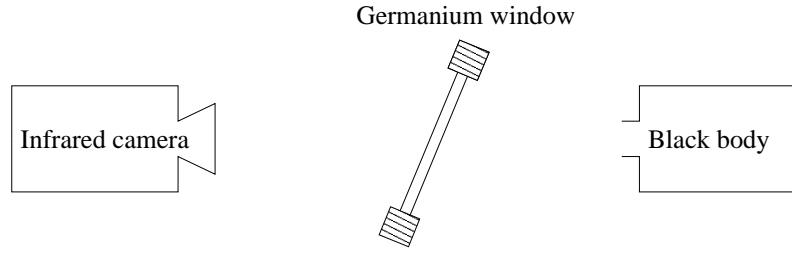
Figure 4.11: Setup for the Calibration measurements

porated into the calibration. The window is also put at an angle because during the experiments the camera also looks at the model at an angle in order to avoid the reflection of the camera to occur in the field of view (narcissus effect). The temperature of the black body is measured by a thermocouple (see appendix B) attached to the back of the cone since this is also the part directly monitored by the camera
Two calibrations were performed, one at the beginning of the experiments and one at the end. The results are shown in table 4.3.1 and figure 4.12. Concluding from table 4.3.1 the difference in camera constants seems quite large.
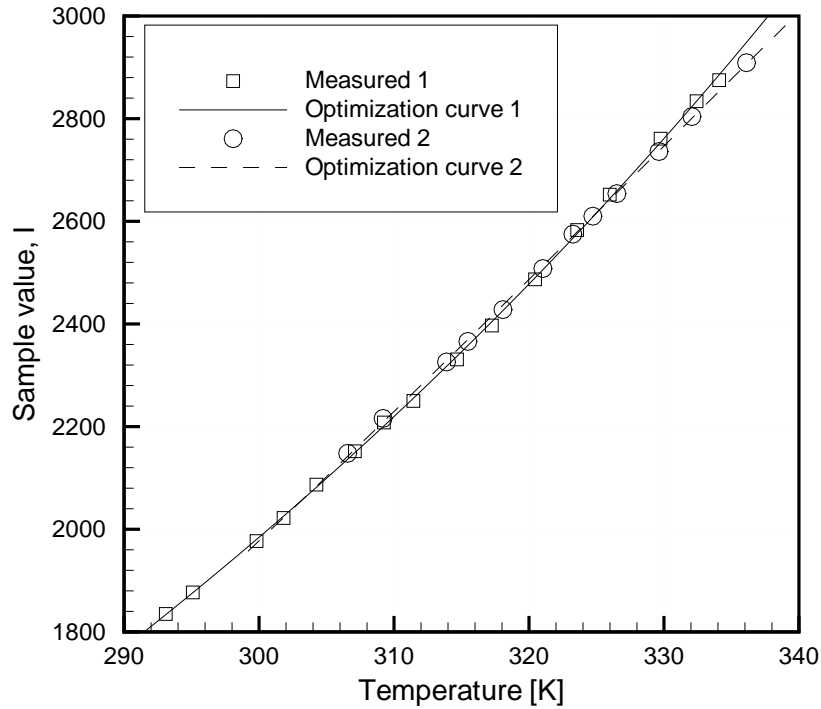
Figure 4.12: Calibration measurements and fitted curves

Either when considering figure 4.12, the two calibration curves are very close to each other. From this can be concluded that not the absolute values of the camera constants are important but the combination of them. This is an important conclusion which will also be important when the data reduction is considered. During the calibration the temperature between the incoming and

	calibration 1	calibration 2
R	242131	9947.3
B	1382.19	628.706
F	-22.2316	3.11816

Table 4.1: Calibration results

outgoing water is measured. The maximum difference was $\pm$ 0.5 K, however, as the heat diffuses through the whole black body, the temperature differences in the black body itself are significantly lower than this value. In the spatial temperature distribution measured by the camera the only temperature difference noticeable is caused by the noise of the camera.

4.3.2 Emissivity measurement

To be able to evaluate the surface temperature of the model accurately, the emissivity must be measured. Since the emissivity is a material property, a special sample can be made for emissivity measurements. Special care has to be taken that the surface finish is equal to that of the model. The emissivity is measured by correlating the temperature of the sample to the emitted radiation. The sample is heated by warm water flowing through it (see figure 4.13), the temperature of the water is measured by a thermocouple (see appendix B). The infrared camera measures the
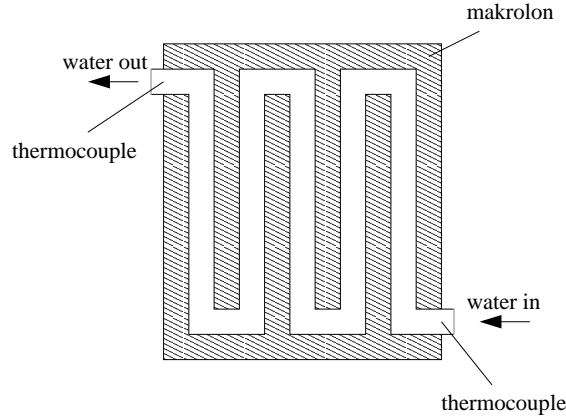
Figure 4.13: Emissivity measurement object

radiation emitted by the object. This radiation consists of the radiation emitted by the object and the reflected radiation from the ambient. Because the object is opaque to the infrared the relation becomes:

$$I_{\text{measured}} = \epsilon \, I_o + (1 - \epsilon) \, I_a \qquad (4.10)$$

I_o and I_a can be calculated using the calibration function (4.9) together with the calibration constants. Since the calibration function was obtained using the germanium window, also the emissivity measurements are conducted using the germanium window. With I_o and I_a known, equation (4.10) is rewritten and ϵ can be calculated form the measured radiation intensity as

$$\epsilon = \frac{I_{\text{measured}} - I_a}{I_o - I_a}. \qquad (4.11)$$

The temperature of the object was measured at the water input, the maximum temperature difference between input and output was 0.03 mV which is equivalent to 0.5 K, this is the same temperature difference as has been found for the black body. This can be further minimized by

better insulating the emissivity measurement object. The emissivity was calculated for different sample temperatures, the results are plotted in figure 4.14. From these emissivities the mean is

Figure 4.14: Emissivity measurement results

calculated, $\epsilon_{\mathrm{mean}} = 0.88$ which is used in the data reduction. The maximum difference between the measured emissivities and the mean is 3.4 %.

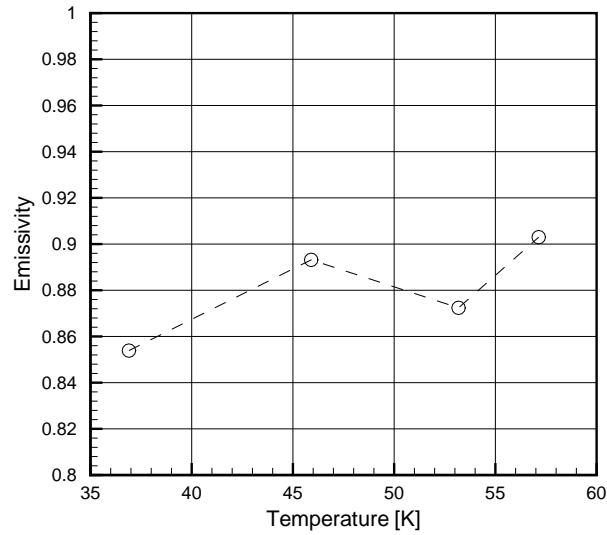Which is adequate since in [9] Carlomagno and de Luca prove that for a gray body that the error imposed on the temperature reading due to an emissivity error is always smaller than one fourth of the emissivity error.

Chapter 5

Short duration heat transfer measurement techniques

5.1 Heat-flux sensors

Heat-flux sensors generally consist of slabs with a known thermal behavior, whose temperature is measured at fixed points. The equation for heat conduction in solids applied to a proper sensor model yields the relationship by which measured temperature is correlated to convective heat transfer rate.

The most commonly used heat-flux sensors are the so called one-dimensional ones, where the heat-flux to be measured is assumed to be (predominantly) normal to the sensing-element surface, and the temperature gradients parallel to the plane of the slab are negligible (this requires a low conductive material). In practice, the slab surfaces may also be curved, but the curvature is neglected if the layer affected by the input heat-flux is rather small compared to the local radius of curvature of the slab. Strictly speaking there is another type of one-dimensional sensor, the Gordon gauge, in which the heat-flux normal to the sensor surface is correlated to a radial temperature difference, along the direction parallel to the slab.

In the following, only ideal one-dimensional sensors are considered. The term ideal means that the thermophysical properties of the sensor materials are assumed independent of the temperature (this is valid if the temperature range is not very large) and that the effect of the presence of the actual temperature-sensing element is not considered, this is valid for IR thermography where the model surface itself or the paint on the surface is the sensor. The four basic one-dimensional sensor models are, [9]:
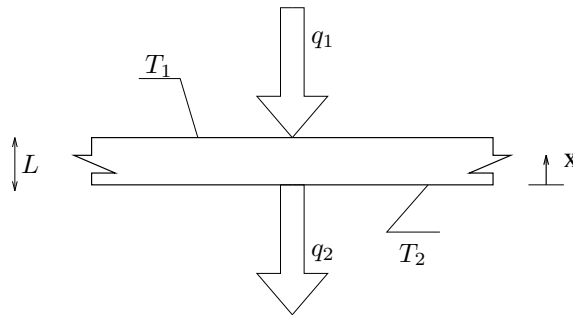

Figure 5.1: Sketch of the generalized one-dimensional heat-flux sensor

Thin-film sensor.   A very thin resistance thermometer classically measures the surface temperature of a "thermally" thicker slab on which it is mounted. The heat-flux is inferred from the theory of heat conduction in a semi-infinite one dimensional wall (see section 5.2). The surface film is made thin so as to have negligible heat capacity and thermal resistance compared to the slab. Surface temperature can be measured by means of IR thermography. In that case the paint to obtain high emissivity is medium 1. If the medium 2 already has the right characteristics (high emissivity), medium 1 can be omitted to increase accuracy. In figure 5.1, the heated surface temperature T_1 is measured.

Thick-film sensor.   The slab is used as a calorimeter, a device to register heat storage. The heat-flux is inferred from the time change of mean slab temperature. This temperature is usually obtained by using the slab as a resistance thermometer. This sensor cannot be used with IR thermography since the surface temp is not an accurate measure of the mean temperature. In figure 5.1, the mean temperature $\bar{T} = \int_0^L T \mathrm{d}x/L$ is measured.

Wall calorimeter/ thin-skin method.   This is a modification of the above method where the slab is made thermally thin (so that the temperature can be assumed constant across the thickness) and is used as a calorimeter. Heat-flux is typically inferred from the time rate of change of the rear-face temperature, usually measured by a thermocouple. This sensor can be used with IR thermography observing the back surface. In figure 5.1, the lower face temperature T_2 is measured in this case.

Gradient sensor.   In this sensor the temperature difference across the slab thickness is measured. The heat-flux is computed from the temperature gradient across the slab. This temperature difference is usually measured using a thermopile of very-thin-ribbon thermocouples or by two thin-film resistance thermometers. As an alternative, an IRSR (infrared scanning radiometer) can be applied. In figure 5.1, the temperature difference $\Delta T = T_1 - T_2$ is measured.

5.2   One dimensional analysis of heat transfer

The basic time-dependent heat transfer problem of heat-flux sensors is that of conduction into a slab of material (medium 1) mounted on a semi-infinite extent of another material (medium 2) as shown in figure 5.2. In the case of a thin film gauge the slab is a thin film deposited on the surface
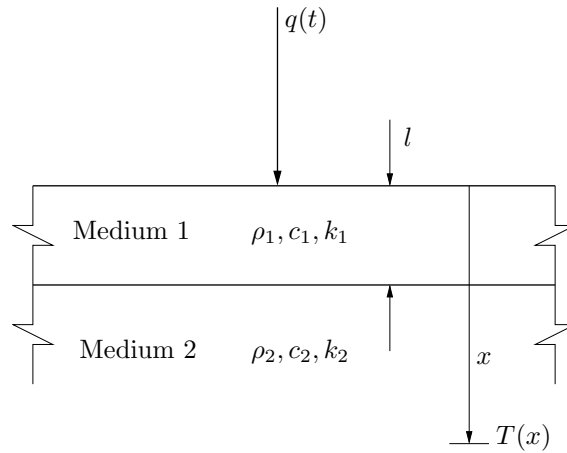

Figure 5.2: Coordinate system for heat conduction in a slab on a semi-infinite substrate

of the medium 2 in order to monitor the surface temperature. It is desired that the film is of such a thickness and has such thermal properties that it does not significantly affect the temperature history of the substrate surface. On the other hand a calorimeter gauge employs a relatively thick slab as medium 1; the temperature of this is measured (using thermocouples) at some point in the slab and it is necessary to know how this measured temperature is related to those throughout the slab (Wall calorimeter). To give an overall view on the heat transfer process in the two-medium material, the basic equations for this configuration will be considered for the general case. The results of this analysis can be used to obtain a better understanding about certain simplifications made in the next sections, and to asses requirements regarding substrate thickness and material properties [34].

The basic equations are derived using the Fourier equation for one dimensional heat flow in each slab:

$$\frac{\partial^2 T_1}{\partial x^2} = \frac{1}{\alpha_1} \frac{\partial T_1}{\partial t}, \tag{5.1}$$

$$\frac{\partial^2 T_2}{\partial x^2} = \frac{1}{\alpha_2} \frac{\partial T_2}{\partial t}, \tag{5.2}$$

where α is the thermal diffusivity of the material. If the surface heat transfer rate is $\dot{q}_s(t)$, then the boundary conditions read:

$$\begin{aligned}
-k_1 \frac{\partial T_1}{\partial x} &= q_s & \text{at} \quad x = 0, \\
k_1 \frac{\partial T_1}{\partial x} &= k_2 \frac{\partial T_2}{\partial x} & \text{at} \quad x = l, \\
T_1 &= T_2 & \text{at} \quad x = l, \\
T_2 &= 0 & \text{at} \quad x = \infty.
\end{aligned} \tag{5.3}$$

Taking the Laplace transform, denoted by "-":

$$\frac{\partial^2 \bar{T}_1}{\partial x^2} = \frac{p}{\alpha_1} \bar{T}_1, \tag{5.4}$$

$$\frac{\partial^2 \bar{T}_2}{\partial x^2} = \frac{p}{\alpha_2} \bar{T}_2, \tag{5.5}$$

with general solutions:

$$\bar{T}_1 = A e^{x\sqrt{p/\alpha_1}} + B e^{-x\sqrt{p/\alpha_1}}, \tag{5.6}$$

$$\bar{T}_2 = C e^{x\sqrt{p/\alpha_2}} + D e^{-x\sqrt{p/\alpha_2}}. \tag{5.7}$$

The transformed boundary conditions are:

$$\begin{aligned}
-k_1 \frac{\partial \bar{T}_1}{\partial x} &= \bar{q}_s & \text{at} \quad x = 0, \\
k_1 \frac{\partial \bar{T}_1}{\partial x} &= k_2 \frac{\partial \bar{T}_2}{\partial x} & \text{at} \quad x = l, \\
\bar{T}_1 &= \bar{T}_2 & \text{at} \quad x = l, \\
\bar{T}_2 &= 0 & \text{at} \quad x = \infty.
\end{aligned} \tag{5.8}$$

These conditions can now be used to evaluate the constants from equations (5.6) and (5.7):

$$\bar{T}_1 = \frac{\bar{q}_s \sqrt{\alpha_1} \left[(1+a) e^{-(x-l)\sqrt{\frac{p}{\alpha_1}}} + (1-a) e^{(x-l)\sqrt{\frac{p}{\alpha_1}}} \right]}{k_1 \sqrt{p} \left[(1+a) e^{l\sqrt{\frac{p}{\alpha_1}}} - (1-a) e^{-l\sqrt{\frac{p}{\alpha_1}}} \right]}, \tag{5.9}$$

$$\bar{T}_2 \quad = \quad \frac{2\bar{q}_s\sqrt{\alpha_1}e^{(l-x)\sqrt{\frac{p}{\alpha_2}}}}{k_1\sqrt{p}\left[(1+a)e^{l\sqrt{\frac{p}{\alpha_1}}} - (1-a)e^{-l\sqrt{\frac{p}{\alpha_1}}}\right]}, \tag{5.10}$$

where:

$$a = \sqrt{\frac{\rho_2 c_2 k_2}{\rho_1 c_1 k_1}}.$$

The transformed time derivatives of the temperature are given by the equation:

$$\frac{\partial \bar{T}}{\partial t} = p\bar{T}. \tag{5.11}$$

Now the solutions of equations (5.9), (5.10) and (5.11) can be applied to the problems that arise, by inverting the transformed quantities and using a numerical technique or expanding in approximate forms.

This set of transformed equations form a basis for the unified treatment of all types of calorimeter heat transfer gauges, thin film gauges and thick wall transducers. The process of inverting these transformed equations is simplified in the thin film gauge for example by allowing l to tend to zero. For the calorimeter gauge l is finite and a is usually much less than unity so that a second form of simplification is possible. In the following sections the thin film sensor is investigated in further detail.

5.3   Gauges operating on the Semi-infinite principle

The heat transfer gauges most commonly used in short duration facilities are of the thin film type. The surface temperature is determined and the heat transfer rate is inferred from the application of equations (5.9) and (5.10). The surface temperature of the model can be determined by a variety of methods: surface-mounted thin film thermocouples, semiconductor resistance thermometers or by using an infrared camera. When observing the surface temperature using an infrared camera the actual gauge is the coating (paint) used to obtain a high emissivity or just the model surface itself. Although the temperature measuring methods may differ significantly from each other, the basic data reduction theory will be the same to a large extent.

5.3.1   Variation of surface temperature with time and heat transfer rate

Assuming in the first instance that the surface measuring film has negligible effect on the heat conduction process, the surface temperature of the substrate may be found by putting $l = 0$ in equation (5.10). The temperature of the substrate then becomes:

$$\bar{T} = \frac{1}{\sqrt{\rho c k}}\frac{\bar{q}_s}{\sqrt{p}}e^{-x\sqrt{\frac{p}{\alpha}}}. \tag{5.12}$$

Now $\rho c k$ and α refer to the substrate properties. At the surface, $x = 0$:

$$\bar{T}_s = \frac{1}{\sqrt{\rho c k}}\frac{\bar{q}_s}{\sqrt{p}}. \tag{5.13}$$

Taking the inverse Laplace:

$$T_s = \frac{1}{\sqrt{\pi\rho c k}}\int_0^t \frac{q_s(\tau)d\tau}{(t-\tau)}. \tag{5.14}$$

Alternatively the heat transfer at the surface may be obtained from equation (5.13) in the form:

$$\bar{q}_s = \bar{T}_s\sqrt{p}\sqrt{\rho c k}. \tag{5.15}$$

Inverting the above equation yields:

$$q_s = \sqrt{\frac{\rho c k}{\pi}} \int_0^t \frac{\frac{dT_s(\tau)}{d\tau}}{\sqrt{t-\tau}} d\tau. \tag{5.16}$$

In principle this shows how to determine the variation of the heat transfer in time from the observed surface temperature $T_s(t)$. This form is inconvenient for practical data reduction since it involves the differential of the surface temperature which will make the determination of equation (5.16) inaccurate due to the presence of noise. The differential can be removed by integrating equation (5.16) by parts with the boundary condition, $T(\tau) = 0$ for $\tau = 0$:

$$q_s = \sqrt{\frac{\rho c k}{\pi}} \left[\frac{T(t)}{\sqrt{t}} + \frac{1}{2} \int_0^t \frac{T(t) - T(\tau)}{(t-\tau)^{3/2}} d\tau \right]. \tag{5.17}$$

This is the form of the solution which is more convenient for data analysis at non constant heat transfer rate. In this form there is, however, a singularity in the integral term at $t = \tau$ which will give rise to errors in the deducted values of $\dot{q}_s$. These errors will in general be larger for small t. Numerical techniques which either reduce or avoid this difficulty are discussed in section 5.4.

For constant heat transfer, equation (5.14) reduces to:

$$T_s = \frac{2q_s}{\sqrt{\pi}} \sqrt{\frac{t}{\rho c k}}. \tag{5.18}$$

From this equation it is seen that under constant heat transfer the surface temperature develops square root like in time. One of the most important criteria is how thick the substrate should be to enable the above analysis to be applied. This thickness may be obtained by considering the solution of the heat transfer equation for the temperature T at depth x, if the surface is subjected to a step function of surface heat transfer q_s whose Laplace transform is q_s/p. The temperature can now be obtained from equation (5.3.1):

$$\bar{T} = \frac{q_s}{\sqrt{\rho c k}} \frac{e^{-x\sqrt{\frac{p}{\alpha}}}}{p^{3/2}} \tag{5.19}$$

Inversion of this expression gives:

$$T = \frac{q_s}{\sqrt{\rho c k}} \left[\frac{2\sqrt{t}}{\sqrt{\pi}} e^{-\frac{x^2}{4\alpha t}} - \frac{x}{\sqrt{\alpha}} \mathrm{erfc}\left(\sqrt{\frac{x^2}{4\alpha t}} \right) \right], \tag{5.20}$$

$$q(x,t) = q_s \mathrm{erfc}\left(\sqrt{\frac{x^2}{4\alpha t}} \right). \tag{5.21}$$

Introducing a dimensionless penetration depth $x^* = x/\sqrt{4\alpha t}$ and putting $x = 0$ in equation (5.20) to obtain the surface temperature:

$$\frac{T}{T_s} = e^{-(x^*)^2} - \sqrt{\pi} x^* \mathrm{erfc}\left(x^* \right), \tag{5.22}$$

$$\frac{q(x,t)}{q_s} = \mathrm{erfc}\left(x^* \right). \tag{5.23}$$

Values of T/T_s and q/q_s are plotted in figure 5.3. The ratio $T/T_s = 0.01$ at $x^* = 1.58$ and $q/q_s = 0.01$ at $x^* = 1.87$. The ratios T/T_s and q/q_s do not fall to 0.01 until $x^* = 3.16\sqrt{\alpha t}$ and $x^* = 3.74\sqrt{\alpha t}$ respectively. These two criteria yield depths so close to each other that a convenient rule of thumb would be $x^* = 4\sqrt{\alpha t}$. The penetration depth at which T/T_s and q/q_s are 1 % of their surface values are given in Schultz and Jones [34] for some commonly used metals and insulators
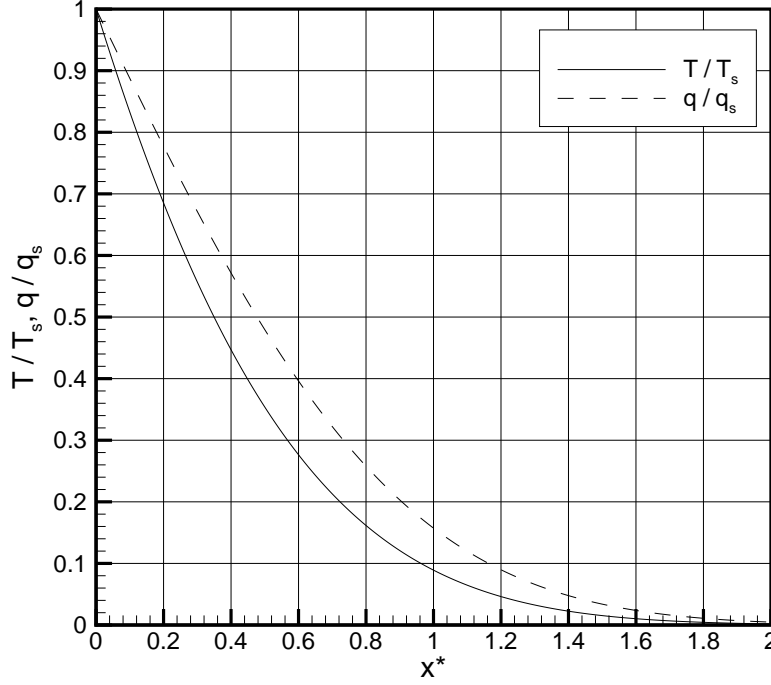
Figure 5.3: Temperature and heat transfer distribution due to a forcing heat flux step at the surface

for constant thermal properties. For metals the rule of thumb would yield $x^*(cm) = 4\sqrt{t(sec)}$ and for insulators it results in $x^*(cm) = 0.3\sqrt{t(sec)}$. As can be seen from the rules of thumb, $x^*_{metals} > x^*_{insulators}$, this is a logical result because in contrary to insulators, metals are good thermal conductors. This implies that a thermal step can penetrate faster into metals than into insulators which results into a larger penetration depth.

5.4   Data reduction based on numerical integration

The evaluation of the heat transfer rate from the observed surface temperature time history record can be carried out numerically or by the use of electrical analogues of the heat conduction process. The electrical analogues were merely used for real-time data reduction. The numerical procedure is convenient when the original data is recorded in either analogue or digital form.

Direct numerical computation   The heat transfer can be directly calculated using equation (5.17):

$$q_s = \frac{\sqrt{\rho c k}}{\sqrt{\pi}} \left[\frac{\phi(t)}{\sqrt{t}} + \int_0^t \frac{\phi(t) - \phi(\tau)}{(t-\tau)^{3/2}} d\tau \right], \tag{5.24}$$

where $\phi(t)$ is the rise in the surface temperature, $T(t) - T(0)$.
Numerical integration of the second part of the expression enables $q_s(t)$ to be determined when the heat transfer rate is not constant, but when evaluating the integration a singularity at $t = \tau$ emerges. Different numerical procedures can be used for reducing the errors introduced by the

uncertainty in the integral term. The effect of this is greatest for small values of t while maintaining constant steps of integration. Different techniques can be used to avoid the singularity in the integral (e.g. trapezoidal rule for integral evaluation), in all techniques the errors are reduced with increasing time from the start of the run. In [14] Cook and Felderman developed a direct numerical integration method by approximating $\phi(\tau)$ through a piecewise linear function of the form:

$$\bar{\phi}(\tau) = \phi(t_{i-1}) + \frac{\phi(t_i) - \phi(t_{i-1})}{\Delta t} (\tau - t_{i-1}) \tag{5.25}$$

where $t_{i-1} \leq \tau \leq t_i$ and $i = 1, 2, 3, \ldots, n$. This equation can now be inserted into equation (5.24), which after some algebra (see appendix A) results in:

$$
\begin{aligned}
q_s(t_n) &= \frac{\sqrt{\rho c k}}{\sqrt{\pi}} \left[\frac{\phi(t)}{\sqrt{t}} + \sum_{i=1}^{n-1} \left\{ \frac{\phi(t_n) - \phi(t_i)}{(t_n - t_i)^{1/2}} - \frac{\phi(t_n) - \phi(t_{i-1})}{(t_n - t_{i-1})^{1/2}} \right. \right. \\
&+ \left. \left. 2\frac{\phi(t_i) - \phi(t_{i-1})}{(t_n - t_i)^{1/2} + (t_n - t_{i-1})^{1/2}} \right\} + \frac{\phi(t_n) - \phi(t_{n-1})}{\sqrt{\Delta t}} \right].
\end{aligned}
\tag{5.26}
$$

This equation can be directly applied to a measured temperature signal to calculate the heat transfer. The only approximation involved in the use of this equation is the local linearization of $\phi(t)$.

Indirect numerical computation As already noted in section 5.3.1, the integrand in equation (5.16) involves the time derivative of the measured temperature. This is inconvenient because it will yield the amplification of any noise present in the measured temperature signal. So integration by parts is used to avoid this noise amplification. An alternative approach to minimize the need for smoothing of the temperature signal is presented in Simeonides [36]. In effect, the one-dimensional heat conduction equation is solved with the same assumptions, initial and boundary conditions as before but for the cumulative heat input to the model surface during a time t rather than the instantaneous convective heating rate, to give:

$$Q(t) = \sqrt{\frac{\rho c k}{\pi}} \int_0^t \frac{T_s(\tau)}{(t - \tau)^{1/2}} \mathrm{d}\tau, \tag{5.27}$$

and the heat transfer rate is then given by:

$$q_s(t) = \frac{\mathrm{d}Q(t)}{\mathrm{d}t}. \tag{5.28}$$

Equation (5.27) can be numerically integrated by [2]:

$$Q(t_n) = \sqrt{\frac{\rho c k}{\pi}} \sum_{i=1}^{n} \frac{\phi(t_{i-1}) + \phi(t_i)}{(t_n - t_{i-1})^{1/2} + (t_n - t_i)^{1/2}} \Delta t. \tag{5.29}$$

Now the derivative defined by equation (5.28), can be computed using finite differencing:

$$q_s(t_n) = \frac{-2Q(t_{n-8}) - Q(t_{n-4}) + Q(t_{n+4}) + 2Q(t_{n-8})}{40(t_n - t_{n-1})} \tag{5.30}$$

Filtering This indirect data-reduction method can still pose some problems with the amplification of the noise in the original temperature signal.
For this reason the temperature signal can be filtered before the data reduction is applied. For this the Gaussian filter is used, since the noise is also of Gaussian origin. The filtering is a convolution of the raw temperature signal with a convolution mask:

$$T_{i,\mathrm{gaus}} = d_{\mathrm{gaus}} * T_i. \tag{5.31}$$

The convolution mask (the actual filter) is given by a vector, which size is given by the number of data-points which contribute to the filtering of the central data-point. The elements of the kernel are defined by:

$$d_{\text{gaus},j} = \frac{e^{\frac{j^2}{\sigma}}}{\sum_{i=1}^{n} e^{\frac{i^2}{\sigma}}}. \tag{5.32}$$

In this definition $d_{\text{gaus},j}$ is the j-th component of the kernel, n is the kernel size, σ is the steepness parameter and element $(n+1)/2$ is the central element of the kernel. If σ tends toward zero, the filter becomes a Dirac-function at the central element. If σ goes to infinity, the filter becomes an average filter (all the elements have the same value: $1/n$).

5.5 Data reduction based on algebraic curve fitting

In section 5.2 the general equations for the heat transfer in a 2-layer medium were derived. These equations are valid for arbitrary surface heat transfer rates varying in time. They were further simplified by assuming that the thickness of the upper slab is infinitesimally small ($l = 0$). This expression can be used to reduce surface temperature to heat transfer, using a piecewise linear approximation of the temperature development. This data reduction method is very noise sensitive and requires a certain minimum amount of measurement samples which have to be evenly distributed in time. Due to these restrictions also another method is applied for comparison. This approach is discussed further in this section, and is based on the fact that for certain boundary conditions an analytical solution for the surface temperature variation in time can be obtained. By fitting these analytical expressions to the measured surface temperature evolution in time, the heat transfer can be deducted, [16]. The fit is done through an optimization process. In this section two analytical expressions are discussed, the first is based on the assumption that the heat transfer <u>coefficient</u> is constant under invariant flow-conditions. The second expression is obtained by assuming a constant value of the heat transfer itself, which is a further simplification of the constant heat transfer coefficient assumption. Also the implementation of the analytical expressions and the optimization method is discussed.

5.5.1 Variation of surface temperature based on constant heat-transfer coefficient

When the one dimensional heat diffusion equation in solids is evaluated using the following hypothesis as the surface boundary conditions:

$$-k\frac{T}{x}\big|_{x=0} = h\left[T_{aw} - T(0,t)\right], \tag{5.33}$$

where h is the heat transfer coefficient. When h is assumed constant an analytical equation can be put up for the temperature development:

$$\frac{T(x,t) - T_{s,i}}{T_{aw} - T_{s,i}} = \text{erfc}\left(\frac{x}{2\sqrt{\alpha t}}\right) - \exp\left[\left(\frac{hx}{k} + \frac{h^2xt}{k^2}\right)\right]\text{erfc}\left(\frac{x}{2\sqrt{\alpha t}} + \frac{h\sqrt{\alpha t}}{k}\right), \tag{5.34}$$

where T_{aw} is the adiabatic wall temperature and $T_{s,i}$ is the initial surface temperature. This equation can now be used to determine the surface temperature development, this can be done by putting $x = 0$ in equation (5.34):

$$T_s = T_{s,i} + (T_{aw} - T_{s,i})\left[1 - e^{\beta^2}\text{erfc}(\beta)\right], \tag{5.35}$$

where $\beta = h\sqrt{t}/\sqrt{\rho c k}$ to simplify the notation.

In the presence of radiative heat flux, under the assumption that the convective and radiative contribution are uncoupled, equation (5.35) can be modified to take the radiation into account:

$$T_s = T_{s,i} + (T_{aw} - T_{s,i})\left[1 - e^{\beta^2}\text{erfc}(\beta)\right] - \frac{q_r}{h} \tag{5.36}$$

With:

$$q_r = \sigma\epsilon\left(T_s{}^4 - T_a{}^4\right) \tag{5.37}$$

Where in equation (5.37) T_s is the measured surface temperature.

5.5.2   Variation of surface temperature based on constant heat-transfer

In section 5.3.1 the temperature development under constant heat-transfer was derived, repeating equation (5.18) gives:

$$T_s = \frac{2q_s}{\sqrt{\pi}}\sqrt{\frac{t}{\rho ck}}$$

Just like in the previous case, it is also possible to compensate for radiative losses:

$$T_s = \frac{2\left(q_s - q_r\right)}{\sqrt{\pi}}\sqrt{\frac{t}{\rho ck}}. \tag{5.38}$$

Where q_r is given by equation (5.37). When regarding equation (5.33), which is used for the calculation of the convective heat-transfer, h and T_{aw} are considered constant since they are determined by the flow structure. T_w is the only time dependent variable because the surface is heated by the flow. To examine the current simplification (with respect to the constant heat transfer coefficient case) the time dependent wall temperature is divided into two different parts. One part is the constant initial temperature, $T_{s,i}$, and the second part is the variable temperature increase $\phi(t)$.

$$q_c = h\left(T_{aw} - T_{s,i} - \phi(t)\right)$$

$$q_c = h\left(T_{aw} - T_{s,i}\right)\left\{1 - \frac{\phi(t)}{T_{aw} - T_{s,i}}\right\} \tag{5.39}$$

So, for this method to be applicable, the last term has to be negligible. This means that the total temperature rise of the model must be small compared to the adiabatic wall temperature (which is assumed constant under constant flow conditions) minus the initial wall temperature.
In the current experiments $T_{aw} - T_{s,i}$ is approximately 400 K and $\phi(t)$ has a maximum of about 30 K. This results in a deviation with respect to the constant heat transfer coefficient of about 8 %.

5.5.3   Algebraic curve fitting through optimization

In the two previous sections, algebraic expressions were obtained using simplified boundary conditions for the heat diffusion equation. The surface temperature in these algebraic equations are a function of the model material constants (ρ, c and k), time and the heat transfer parameters (q_c or h and T_{aw}). The material constants are defined by the material used for the wind tunnel model (see section 3.2.2) and the time is also defined. But the heat transfer parameters are 'free', this means they are only influenced by the thermal state of the body. The thermal state can for example be influenced by the airflow over the body. To find the correct heat transfer parameters which belong to a certain state, the algebraic correlations can be fitted to the measured surface temperature evolution by changing the heat transfer parameters. For the constant heat transfer coefficient case, h and T_{aw} are the free parameters while the constant heat-transfer case only uses q_c. In addition to the heat transfer parameters also a time offset is taken into account to correct for non-instantaneous starting phenomena. In this way a sightly different starting time can be used to compensate for some changes in heat transfer at the start of the run. The introduction of the time offset also creates the possibility to optimize temperature signals which do not incorporate the starting process, provided that the initial temperature is given.
The optimum fit is achieved by minimizing the difference between the measured and algebraic

values. The optimization method requires the difference to be expressed in one function value; this is done by taking the norm of the difference. So the function which is minimized is given by

$$f(\vec{x}, t_0) = \sqrt{\sum_{i=0}^{n} [T_i - T(\vec{x}, t_i - t_0)]^2} \tag{5.40}$$

Where T_i is the measured temperature signal, $T(\vec{x}, t_i - t_0)$ is the algebraic temperature signal, $\vec{x}$ is the vector containing the free parameters and t_0 is the starting time offset.

The free parameters obtained by the optimization process are now the characteristic numbers for the heating process. The optimization method uses the Nelder-Mead simplex method.

5.5.4   Nelder-Mead simplex method

The Nelder-Mead simplex method is a direct search method which does not require gradient or other derivative information. The method characterizes the elements of a vector $\vec{x}$ to a simplex in a multidimensional space. If the vector has $n+1$ elements, the simplex also consists of $n+1$ points and is situated in a n dimensional space. For example if the vector x has three elements then the simplex is a triangle in a 2D space, and if $\vec{x}$ has four elements, the simplex is a pyramid in a 3D space. At each step of the search, a new point in or near the current simplex is generated. The function value at the new point is compared with the function values at the vertices of the simplex and, usually, one of the vertices is replaced by the new point, giving a new simplex. This step is repeated until the equivalent diameter of the simplex is less than the specified tolerance and the maximum function value differs from the lowest function value by less than the specified tolerance, or the maximum number of function evaluations has been exceeded. For the mathematical procedure see appendix C.

5.6   Data reduction program

In the previous sections the general concepts of the data reduction procedures were given. In the following sections the actual data reduction program will be discussed, this will be done in three parts: the first part is the general data initialization, these are the procedures which are used by both data reduction procedures. In the second part the data reduction procedures based on the numerical integration approach are discussed, while the third part deals with the curve fitting optimization method.

5.6.1   General data initialization

In figure 5.4 the general structure of the general data initialization is presented. There are three files which contain all the necessary data for the data reduction process:

   - the HP1000 data acquisition output file,

   - the BRUT file,

   - and the config file.

HP1000 file   The HP1000 file contains the reservoir pressure as a function of time. In figure 3.2 an example is shown of the total pressure profile during a measurement. In the data reduction procedure the total storage pressure (p_0) is calculated as the average over the first 20 measurements. This is equivalent with the first 7 ms of the data acquisition. From the figure it can be seen that the reservoir pressure remains constant so the 7 ms is adequate to obtain the total pressure. The averaging time is taken this short to make sure no problems occur in case the tunnel is started earlier.
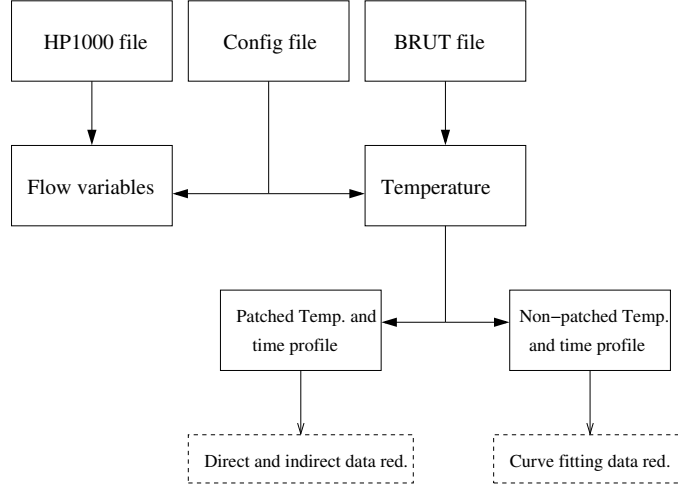
Figure 5.4: General data initialization

BRUT file   The BRUT file contains the binary thermal images from the infrared camera. The file is stored in binary format by the BRUT data acquisition system. The layout of the file with the binary structure is explained in appendix D. The binary file is converted to ASCII-code and the sample values are obtained.

Config file   The config file contains all the user defined input. In this file the position of the model in the thermal image can be set. It is also used to set the reservoir temperature (T_0), calibration constants, ambient temperature (T_a) and parameters for the optimization and filtering. A complete description of the file is given in appendix E.

Flow variables   The flow variables are computed from the parameters obtained through the config and the HP1000 file. The pressure and temperature which are set for the hot storage tube are not equal to the total pressure and total temperature of the free-stream flow. This is due to the non-isentropic unsteady expansion wave which is generated when the fast closing valve is opened (see section 3.1.1). The pressure and temperature have to be corrected for this. For Mach 9 the total pressure and temperature loss is calculated by

$$p_t = 0.888 \cdot p_0, \tag{5.41}$$

$$T_t = 0.967 \cdot T_0. \tag{5.42}$$

Now the static free-stream temperature can be calculated using the total temperature and the Mach number which are set in the config file:

$$T_\infty = \frac{T_t}{(1 + \frac{\gamma-1}{2}M_\infty^2)}. \tag{5.43}$$

The static free-stream pressure is calculated using the averaged reservoir pressure and the Mach number:

$$p_\infty = \frac{p_t}{(1 + \frac{\gamma-1}{2}M_\infty^2)^{\frac{\gamma}{\gamma-1}}}. \tag{5.44}$$

Equations (5.43) and (5.44) together with the perfect gas law can be used to calculate the density:

$$\rho_\infty = \frac{p_\infty}{T_\infty R}. \tag{5.45}$$

To obtain the Reynolds number and the Stanton number it is necessary to calculate the free-stream velocity using the Mach number and the definition for the speed of sound:

$$u_\infty = M_\infty \sqrt{\gamma R T_\infty}. \tag{5.46}$$

The viscosity and conductivity are calculated using the Sutherland law, which is based on the kinetic theory of gases. It relates the variation of the viscosity with temperature to the nature of the intermolecular forces between the molecules:

$$\frac{\mu_\infty}{\mu_r} = \left(\frac{T_\infty}{T_r}\right)^{3/2} \frac{T_r + S_\mu}{T_\infty + S_\mu} \tag{5.47}$$

$$\frac{k_\infty}{k_r} = \left(\frac{T_\infty}{T_r}\right)^{3/2} \frac{T_r + S_k}{T_\infty + S_k}. \tag{5.48}$$

In these equations the subscript r refers to a reference state. In these formulas the reference temperature is 20 $^\circ C$, $T_r = 273 \ K$, the corresponding reference values for the viscosity and conductivity are, $\mu_r = 1.716 \cdot 10^{-5} \ kg/(m \cdot s)$ and $k_r = 0.0241 \ W/(m \cdot K)$. The characteristic temperatures S_μ and S_k are respectively 110 K and 194 K.

Now all the required flow quantities are known, the Reynolds and Prandtl number can be calculated:

$$Re_\infty = \frac{\rho_\infty u_\infty l_{\text{char}}}{\mu_\infty}, \tag{5.49}$$

$$Pr_\infty = \frac{\mu_\infty c_p}{k_\infty}. \tag{5.50}$$

In equation (5.49), l_{char} is a characteristic length-scale, in the current experiments the length of the model is used ($l_{\text{char}} = 131.9 \ mm$).

Temperature profile Before the surface temperature can be calculated from the sample values, it first has to be corrected for the radiation from the ambient reflected from the surface of the model. To do this it is necessary to identify the sources of radiation which are registered by the camera. The radiation received by the camera consists of two contributions (the transmissivity is assumed to be zero so $\rho = 1 - \epsilon$):

$$I_{\text{measured}} = \underbrace{\epsilon \cdot I_o}_{\text{emitted radiation by the model}} + \underbrace{(1 - \epsilon) \cdot I_a}_{\text{reflected radiation from the ambient}}.$$

Here I_{measured} is the measured sample value, while I_o is the desired sample value due to the radiation of the model. If the equation is rewritten, the measured sample value can be corrected using the sample value due to the ambient, I_a, and the emissivity ϵ

$$I_o = \frac{I_{\text{measured}} - (1 - \epsilon) \cdot I_a}{\epsilon}. \tag{5.51}$$

Now the desired sample values can be converted to surface temperatures using the calibration equation

$$T = \frac{B}{\ln\left(\frac{R}{I} + F\right)}. \tag{5.52}$$

In this equation B, F and R are calibration constants obtained by the black body calibration (see section 4.3.1), they are set in the cfg-file. This equation is also used to calculate the sample values due to the ambient

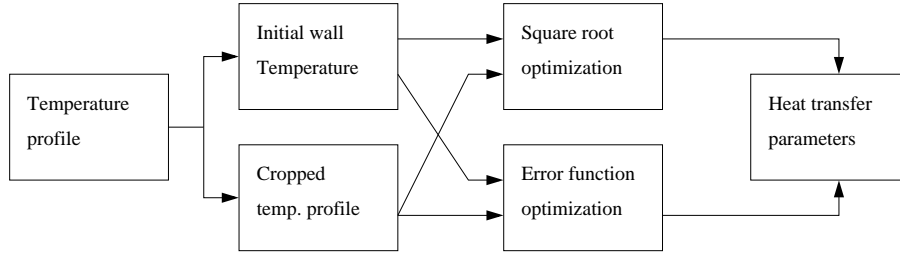$$I_a = \frac{R}{e^{B/T_a} - F}. \tag{5.53}$$

Figure 5.5: Curve fitting data reduction

Time data Since the data reduction is based on a transient heat-transfer process, information about the recording time of a pixel is needed. The time profile is calculated using the characteristics of the camera (see section 4.2.2). The time for one line is 0.4 ms (the line scanning frequency is 2.5 kHz) and each field 30 lines are discarded so the time calculation looks like:

$$t_i = \frac{\text{PIX}/140 + i + 30 \cdot \text{FIELD}}{2500} \tag{5.54}$$

Where 'PIX' is the pixel number which is read, 'FIELD' is the number of fields which have already passed since the start of the recording and $'i'$ is the line number.

For the curve fitting data reduction procedure all preparations are taken and the data reduction can start. The direct and indirect method cannot be applied directly since the camera produces gaps in the data record due to the line scan setting (see section 4.2.2). The temperature signal first has to be patched by linear interpolation; the sample values are first patched and from these patched sample values the patched temperature signal is calculated using equation (5.52).

5.6.2 Curve fitting data reduction procedure

The curve-fitting procedure is schematically depicted in figure 5.5. The first two steps are the determination of the initial temperature $(T_{s,i})$ and the cropping of the signal time record. The initial surface temperature is determined as an average over the first ten measurement points to correct for noise from the camera. The temperature signal is cropped to correct for transient startup and shutdown phenomena, these phenomena can be incorporated into the optimization process but experience shows that they can cause considerable errors. In figure 5.6 a typical temperature signal is given for a position on the flare near the compression corner. In the profile the gaps can be seen where the camera doesn't record sample values. In the first part of the graph the flat signal can be seen where the initial temperature is determined, after the flat signal the temperature starts to rise. In this rise (in the first block) a sort of inflexion point can be seen, this is probably caused by a reflecting shock-wave (see section 3.1.1). This inflexion point has great influence on the data reduction so this part of the signal is cropped (of course the initial temperature is stored). At the end of the run there is a temperature jump, this jump is also cropped. The temperature jump is caused when the valve of the wind tunnel is closed and the model is still immersed in the low speed hot gas flow. The amount of cropping is determined by the user through the cfg-file and the results from the optimization procedure (the value of the minimized function). Both the error function and the square root function are optimized using the same cropped temperature signal, and the heat transfer data (optimized free parameters) is obtained. The square root function optimization immediately gives the heat transfer from which the Stanton number can be calculated (see equation (2.4)):

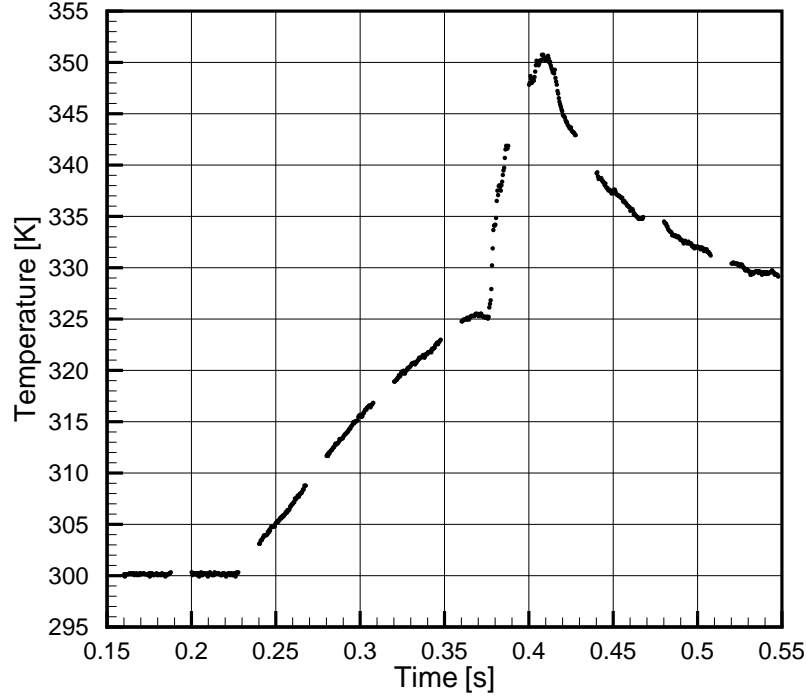$$c_h = \frac{q_c}{c_p \rho_\infty u_\infty (T_t - T_s)}.$$

Figure 5.6: Measured temperature time evolution at a single point on the flare near the compression corner

The error function optimization produces the heat transfer coefficient h and the adiabatic wall temperature T_{aw}. From these values the heat transfer is calculated

$$q_c = h\left(T_{aw} - T_s\right). \tag{5.55}$$

Now also the Stanton number can be calculated using equation (2.4)

5.6.3   Numerical integration data reduction procedure

From figure 5.7 the data reduction procedure can be seen for the direct and the indirect methods. Before the patched temperature signal is used for data reduction it is filtered using a Gaussian filter (see section 5.4). The kernel-size, n and the kernel-shape, σ can be set in the cfg-file. If the kernel-size is set to one, no filtering is applied. In figure 5.8 a typical patched and filtered temperature can be seen. The original temperature data can be seen in figure 5.6. When looking at figure 5.8 it is clear that the filtering doesn't alter the general shape of the signal, it only decreases the high frequency noise in the signal which is desired when using the direct and indirect data reduction methods. The results of the different procedures will be discussed in section 5.7.

5.7   Data reduction Results

Before being able to analyse the flow field using the heat transfer measurements, first the heat transfer data reduction methods have to be evaluated. In this section, the (in)direct and optimization methods will be discussed and compared. Also the influence of the corrections on the obtained heat transfer will be discussed and a data reduction method is chosen.
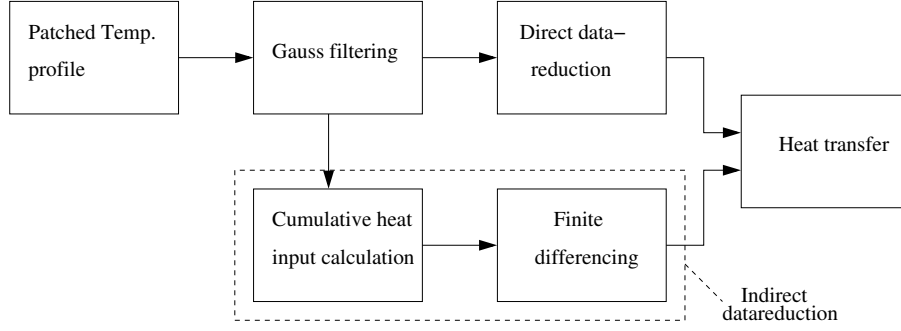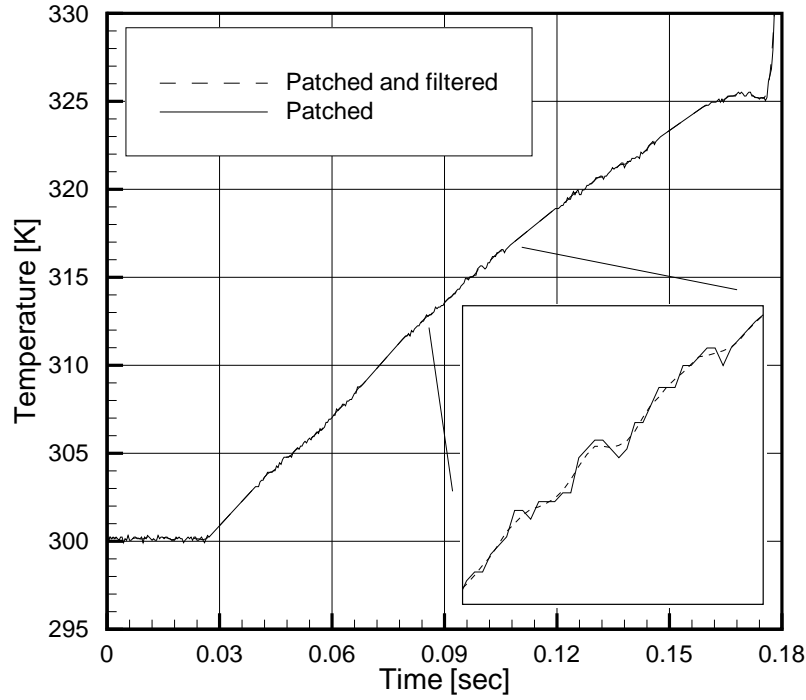
Figure 5.7: Data reduction by direct and indirect numerical integration

Figure 5.8: Patched and filtered temperature signal with $n = 5$ and $\sigma = 10$

5.7.1 Numerical integration methods

In section 5.6.3 the implementation of the direct and indirect data reduction method were discussed. Figures 5.10 and 5.9 give the results for the heat transfer data for the original temperature data of figure 5.8, obtained with the integration methods, with and without filtering. The filtering has a considerable influence on the direct method, it smooths the heat transfer graph. The effect on the indirect method is negligible. When looking back to figure 5.8 the corresponding temperature signal is given, from which can be seen that the filtering has only little effect on the temperature signal, only the high frequency noise which greatly influences the direct method is filtered.
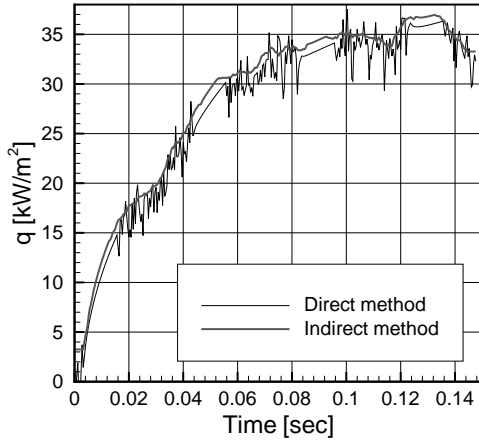
Figure 5.9: Heat transfer calculated using the direct and indirect method without filtering
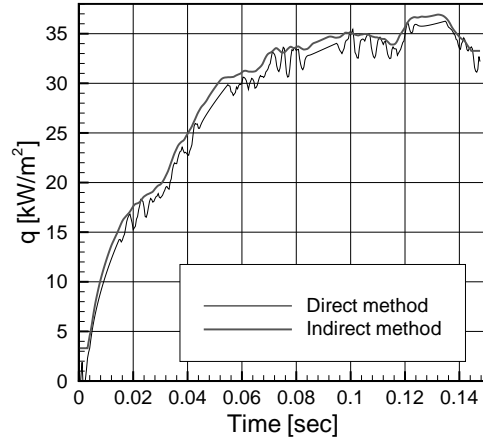
Figure 5.10: Heat transfer calculated using the direct and indirect method with filtering, $\sigma = 10$ and $n = 5$ (equivalent time is 2 ms)

From figure 5.10 it is evident that the heat transfer is changing in time, in the first part of the experiment the heat transfer is expected to increase square-root-like. This makes sense when looking at the first part of the temperature signal in figure 5.8, the signal is nearly linear so a square root shaped heat transfer signal has to appear. This can be seen when repeating equation (5.16):

$$q_s = \sqrt{\frac{\rho ck}{\pi}} \int_0^t \frac{\frac{dT(\tau)}{d\tau}}{\sqrt{t-\tau}} d\tau.$$

If the temperature signal is linear then $\frac{dT(\tau)}{d\tau} = \Delta T$ is a constant. Now the integral can be evaluated and the heat transfer signal for a linear temperature signal is obtained:

$$q_s = 2\Delta T \sqrt{\frac{\rho ck}{\pi}} \sqrt{t}. \tag{5.56}$$

The square-root like graph also emerges when the patched piece of the temperature signal is used in the numerical integration.

At the end of the run the heat transfer becomes nearly constant, this part of the heat transfer signal is averaged and the Stanton number is calculated using equation (2.4). This result indicates that it is preferred to also use the last part of the temperature signal for optimization data reduction. When looking at figures 5.10 and 5.9 it is evident that the indirect method always produces higher heat transfer rates than the direct method, also the indirect method graph is much smoother. From comparison with the optimization data reduction results (see section 5.7.4) can be concluded that the direct method under-predicts the heat transfer.

5.7.2   Optimization methods

In this section the results of the optimization methods are discussed, first the influence of cropping on the heat transfer parameters is studied. In figure 5.11 an uncropped signal is depicted while in figure 5.12 a cropped signal is given. The employed signal is for a pixel which corresponds with a point on the flare near the compression corner (the same point is also used for the direct and indirect method). In table 5.7.2 the corresponding values obtained from the optimization processes are given. When comparing figures 5.11 and 5.12 it appears that the cropping has considerable influence on the optimization process. This is caused by the inflexion point in the
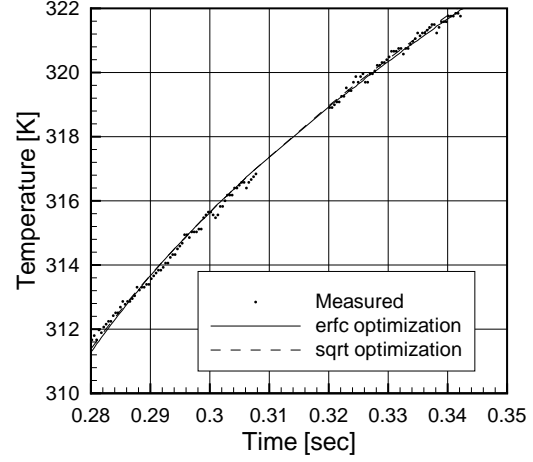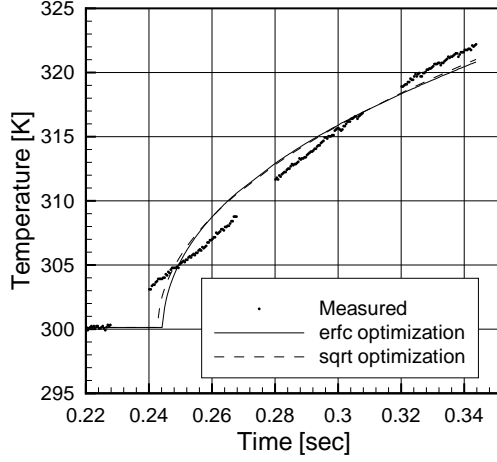
Figure 5.11: Optimization on uncropped signal   Figure 5.12: Optimization on cropped signal

method	quantity		uncropped	cropped
erfc (const h)	h_{opt}	$[W/(m^2 k)]$	81.2	78.5
	$T_{\text{aw,opt}}$	$[K]$	727.5	806.3
	$t_{0,\text{opt}}$	$[s]$	0.244	0.259
	q_c	$[W/m^2]$	32887	38007
	f_{min}	$[K]$	19.5	1.7
sqrt (const q)	$t_{0,\text{opt}}$	$[s]$	0.243	0.258
	q_c	$[W/m^2]$	30881	35457
	f_{min}	$[K]$	17.4	1.5

Table 5.1: Optimization results for cropped and uncropped temperature signal. For the 'erfc' method, q is calculated using $T_{s,i}$

temperature signal, this inflexion is probably caused by the reflection of the expansion wave at the cross-sectional discontinuity (see section 3.1.1). This can also be seen in figures 5.10 and 5.9 where the heat transfer graphs have a dent at approximately 0.03 s. The 'erfc' optimization returns the adiabatic wall temperature and the heat transfer coefficient separately. These values were not used separately because the results for these properties were not realistic, at the end of the flare the adiabatic wall temperature goes to 1100 K which is not realistic since it cannot exceed the total free-stream temperature. Also the heat transfer coefficient cannot be used because it is not affected by any variation on the flow field (it remains nearly constant from the nose to the flare). Although, when they are combined in the heat transfer they do give acceptable results, indicating that just like in the calibration case, not the individual parameters are important but the combination of them (see section 4.3.1).

When the 'erfc' and the 'sqrt' methods are compared, it turns out that they yield nearly the same results. At the flare the two methods differ to a certain extent, which is probably due to the inaccurate adiabatic wall temperature.

5.7.3   Corrections

In the optimization data reduction methods a radiation heat loss correction is applied. When a maximum temperature difference with the ambient of $30°C$ is assumed the radiative loss becomes

$$q_r = \sigma\epsilon\left(T_s{}^4 - T_a{}^4\right) = 175 \ W/m^2.$$

Comparing this to a convective heat transfer of $33 \ kW/m^2$, then the loss is 0.5 %. Under these conditions it can be concluded that it would not be necessary to apply a radiation correction.
Another loss which is not accounted for in the data reduction methods is lateral conduction. Assuming an axisymmetric flow only stream wise temperature gradients appear so only conduction in this direction has to be regarded. The maximum temperature difference between two pixels is approximately $2°C$ for a pixel size of $1 \ mm$. The conduction loss now becomes:

$$q_{\text{cond}} = k\frac{\Delta T}{\Delta x} = 400 \ W/m^2.$$

Compared to the convective heat transfer (1.2 %) also this term can be neglected.

5.7.4   Conclusion

The present heat transfer investigation has shown that the choice of a specific data reduction method does not significantly affects the results. In fact all methods have been applied for data reduction and all methods were found to yield the same results in terms of the convective heat transfer q_c. In figure 5.13 results for different data reduction methods are shown for a smooth nose experiment. Figure 5.14 shows the corresponding results for a roughened nose. All the meth-
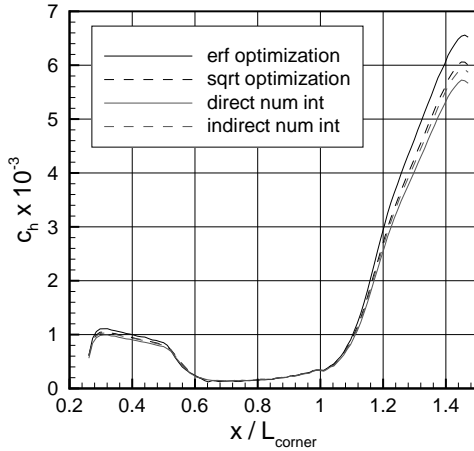

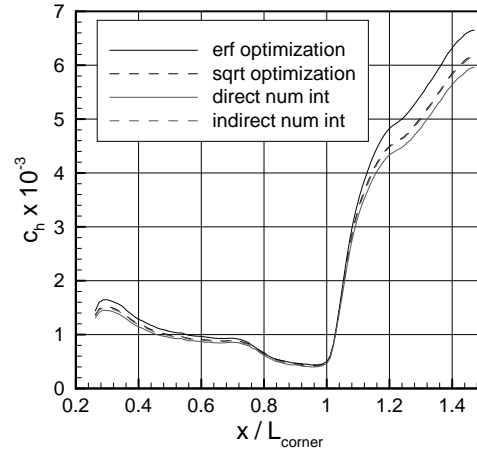Figure 5.13: Stanton curves deducted from run 43, clean nose ($Re_L = 1.12 \times 10^6$)

Figure 5.14: Stanton curves deducted from run 69, rough nose ($Re_L = 1.13 \times 10^6$)

ods give similar results although some differences can be seen: the values obtained by the direct method are always the lowest compared to the other method while the erfc optimization always gives higher values especially at the flare. The maximum difference between these two methods is determined as a typical measure for the data reduction related inaccuracy. The maximum deviation for the clean nose experiments is approximately 10 %, for the rough nose the maximum deviation is 13 % (the maximum difference always occurs between the erfc optimization and the direct method). When comparing the indirect method with the sqrt optimization a maximum deviation of 5% for both the clean and roughened nose is found, where the optimization method always returns the higher vlaues. For flow diagnostics one of these two methods can be used, in the remainder of the thesis the indirect method is used.

Chapter 6

Results

6.1 Flow assessment

Before the final experiments can be conducted, the flow quality in terms of axisymmetry and repeatability have to be checked. Also the measured heat transfer data is checked with a theoretical approximation.

6.1.1 Schlieren images

Schlieren pictures of the flow around the model were obtained using high speed photography and a digital CCD camera. Both color schlieren and black and white pictures were taken. The high speed camera was used to study the transient flow during the startup and to verify that the flow is constant during the experiment. Also the symmetry of the shock pattern was checked.

One of the images obtained by the high speed camera for a clean nose configuration is depicted in figure 6.1. The frame rate of the high speed camera was $500\ Hz$, the first image which showed shock waves already indicated an established flow (the next images showed an identical shock pattern). This indicates that the startup phenomena in the tunnel are in the order of $2\ ms$, which is in good agreement with the startup times found by Holden [23].

In figure 6.1 the shock wave pattern is seen to be symmetric, which indicates a uniform free stream or at least an axisymmetric flow field. The detached bow shock is clearly visible, while further downstream the separation shock can be seen. At half of the flare length the bow shock merges with the separation shock. Below the intersection of the separation and the bow shock the start of the dark compression wave can be seen. At the end of the flare a white expansion is visible.

Using the Taylor-Maccoll method (see section 2.2.3) the shock angle for a pointed cone with a half cone angle of $15°$ can be calculated. This shock angle is expected to be similar to the shock angle of the straight part of the shock obtained from the schlieren picture. For Mach 9.13 a shock angle of $17.6°$ is obtained, the measured angle from the schlieren image is $18°$. This is indicates that the Taylor-Maccoll method can be applied to approximate flow parameters outside of the boundary layer, which can be used for heat transfer approximation.

In figure 6.2 a schlieren picture made by the CCD camera is shown for a roughened nose configuration. Near the nose the contours of the copper turbulators can be clearly discerned. The shock induced by the first turbulator is seen as a black line in the schlieren picture. Where this shock impinges on the bow shock a slip-line is formed, and when figure 6.2 is carefully examined this slip-line (shear layer) can be seen traveling downstream until it reaches the flare. Also the shock and expansion waves generated by the other two turbulators can be seen in the figure. Proceeding further downstream another dark line is visible, which is the separation shock. At the flare the reattachment wave is visible which deflects and recompresses the flow along the flare. To obtain more information from the schlieren pictures they have to be enhanced using edge detectors and brightness/contrast adjustments (see section 6.2.1).
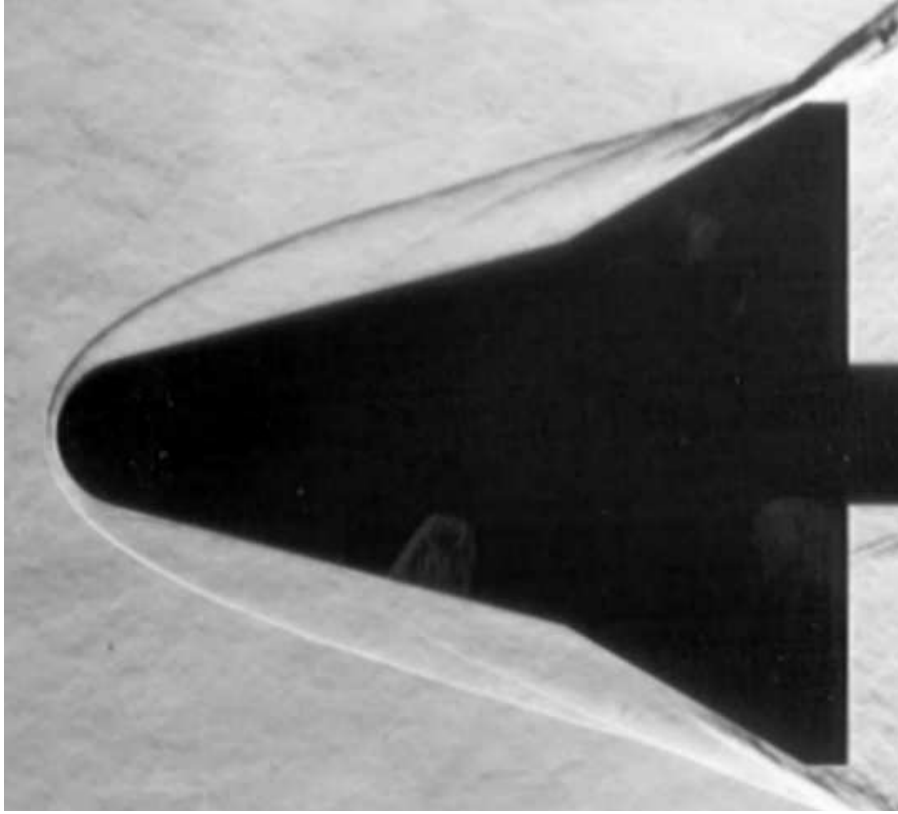
Figure 6.1: Schlieren image from high speed camera for a clean nose at $Re_L = 1.40 \cdot 10^6$ and $M = 9.1$

6.1.2 Theoretical approximation of the heat transfer

As is already stated in the previous section, the Taylor-Maccoll method can be used to approximate values of the flow properties at the edge of the boundary layer, which in their turn, can be used to approximate the heat transfer by applying the method described in section 2.2.2. To compare the approximation with the measured values three cases were regarded: a low, medium and high Reynolds case. The accessory data are depicted in table 6.1 For each Reynolds number the

Input	θ_c [°]	M_∞	T_t [K]	p_{t1} [Pa]	p_{t2} [Pa]	p_{t3} [Pa]
	15	9.13	747	45×10^5	62×10^5	89×10^5
Output	θ_s [°]	M_e	T_e [K]	p_{e1} [Pa]	p_{e2} [Pa]	p_{e3} [Pa]
	17.6	5.56	104.14	1833	2526	3626

Table 6.1: Input and output variables for the Taylor-Maccoll method

boundary layer edge Mach number and temperature are constant just as the shock wave angle θ_s (they only depend on the cone angle). Using the method from section 2.2.2 a relation is obtained between c_h and s, where s is the distance measured along the wetted surface.

In figure 6.3 the clean nose measurements are compared with laminar flow theory. When applying the theory the resulting Stanton number was found to be systematically a factor three too high. So for comparison the theoretical Stanton numbers depicted in figure 6.3 are the theoretical values divided by three. After the correction the theory agrees well with the measurements, both the stream wise trend and the Reynolds dependence are predicted well. From the graph it can be seen that the measured curves are somewhat steeper, this can be explained by the fact that the
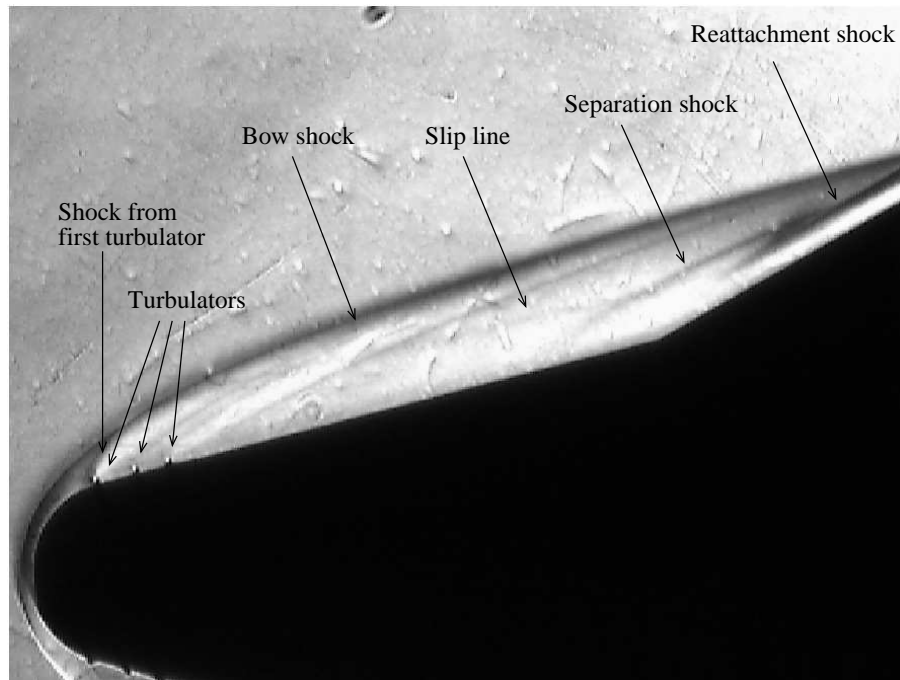
Figure 6.2: Schlieren picture form CCD camera for roughened nose at $Re_L = 1.30 \cdot 10^6$ and $M = 9.1$
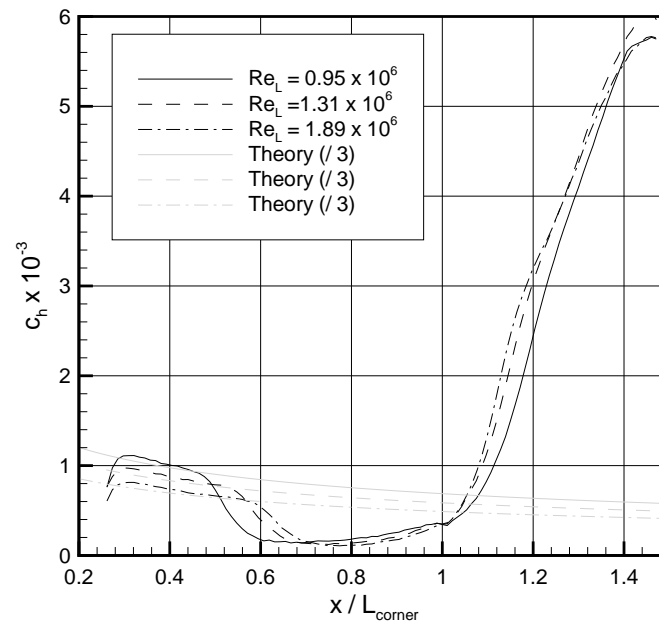

Figure 6.3: Comparison between theoretical and measured Stanton curves

boundary-layer thickness increases faster due to an increase of the Mach number at the edge of the boundary layer induced by the rounded nose. The multiplication factor may be a result of the curved shock. When applying Taylor-Maccoll it is assumed that the boundary edge stream line

has passed through a 17.6 ° oblique shock wave while in reality due to the curved shock this angle may be higher. Another feature of the curved shock is the generation of an entropy layer which introduces temperature gradients and accompanying conduction effects.

6.1.3   Repeatability

For each Reynolds number three experiments were preformed to verify the repeatability of the flow conditions. Figure 6.4 shows the results from three runs for a clean nose configuration. A
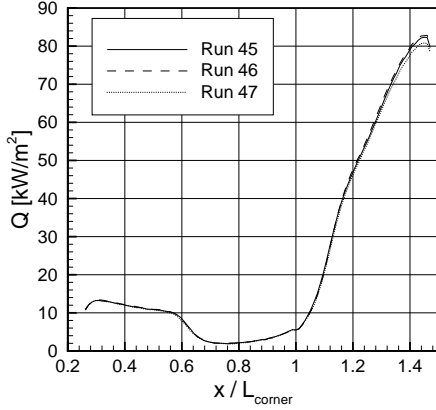

Figure 6.4:   Comparison between three high Reynolds number runs for a clean nose
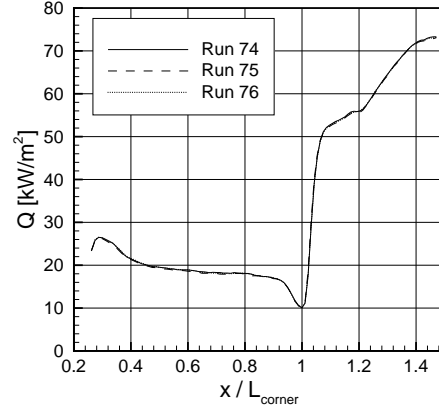
Figure 6.5:   Comparison between three high Reynolds number runs for a rough nose

similar comparison for the rough nose experiment can be seen in figure 6.5. These figures indicate that the repeatability of the measurements is very good, the maximum difference between two measurements is 2%.

6.2   Experimental results

In the experiments a Reynolds number range was covered between $Re_L = 0.56 \times 10^6$ and $Re_L = 1.89 \times 10^6$ which corresponds to reservoir pressures of respectively $P_0 = 30\ bar$ and $P_0 = 100\ bar$. For the clean nose experiments it was found that for reservoir pressures below 50 bar passive heating was insufficient to provide an adequate signal for data reduction, while 40 bar was the minimum reservoir pressure for the rough nose experiments. These minimum pressure levels correspond to a minimum Reynolds number of $Re_L = 0.94 \times 10^6$ for the clean nose case and the minimum Reynolds number is $Re_L = 0.76 \times 10^6$ for the roughened nose case. The pixel size for the heat transfer measurements on the cone is 1.03 mm and on the flare it is 0.91 mm. Appendix F contains an overview of the test conditions.

6.2.1   Clean nose measurements

In figures 6.6 and 6.7 the curves for Stanton number and heat transfer are depicted for different Reynolds numbers. At the front of the model the heat transfer slightly decreases moving downstream due to the laminar boundary layer development. In agreement with laminar theory, the Stanton number is observed to decrease with increasing Reynolds number, being inversely proportional with the square root of the Reynolds number (see section 2.2.2):

$$c_h \propto Re_x^{-1/2}.$$

This can already be concluded from figure 6.3 but is even better visualized when $c_h\sqrt{Re_x}$ is plotted versus x/L_{corner}, see figure 6.8. Near the nose all Stanton curves clearly coalesce onto a nearly
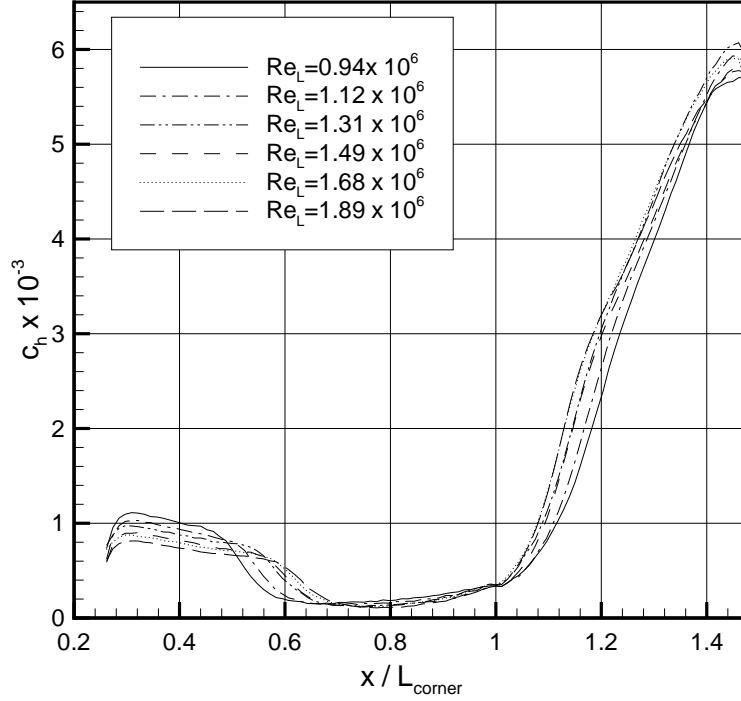
Figure 6.6: Stanton curves for clean nose runs

horizontal line, indicating the $\sqrt{Re_x}$ dependence. When regarding the heat transfer itself (in absolute sense) an opposite trend is noticed, the heat transfer increases with increasing Reynolds number. Due to the density increase more mass flow is available for model heating.
Continuing further downstream an abrupt drop in heat transfer is observed, as a result of the separation of the boundary layer due to the adverse pressure gradient caused by the compression ramp. In [10] Chapman derived that the heat transfer from a separated laminar region is 0.56 of that to a corresponding attached laminar boundary layer having the same constant pressure. From figure 6.7 it can be seen that this corresponds reasonably for the low Reynolds number cases. When the Reynolds number is increased the point of separation moves downstream (see also figure 6.13), this is also visible in the schlieren pictures 6.9 to 6.11 when extending the shock waves toward the model surface (dashed line). According to literature (see section 2.3.5) this is characteristic for transitional interactions since fully laminar or turbulent interactions show a growing separation extent with increasing Reynolds number. In some schlieren pictures the separation shock is difficult to see but if it is extended it agrees with the separation locations observed from the heat transfer distributions. When moving further downstream through the separated region the heat transfer and the Stanton number start to increase strongly due to the effect of the gradual shear layer reattachment. At the flare the heat transfer curve has an inflexion point, this point closely correlates with the location of the compression wave at the back of the flare. In the color schlieren images a green compression wave can be discerned at the flare which deflects the flow so that it runs parallel with the flare. At the back of the flare a red expansion wave can be observed.

At the end of the flare the maximum heating is reached, and the peak heating ratio ($c_{h,peak}/c_{h,ref}$) is quite high, where $c_{h,ref}$ is the reference Stanton number for an identical blunted cone but without flare (no separation). In section 2.3.4 the peak heating correlations of Hung and Barnett [26] are discussed which are given in table 6.2.1 using the conditions behind the first shock (which are approximated by the Taylor-Maccoll method).
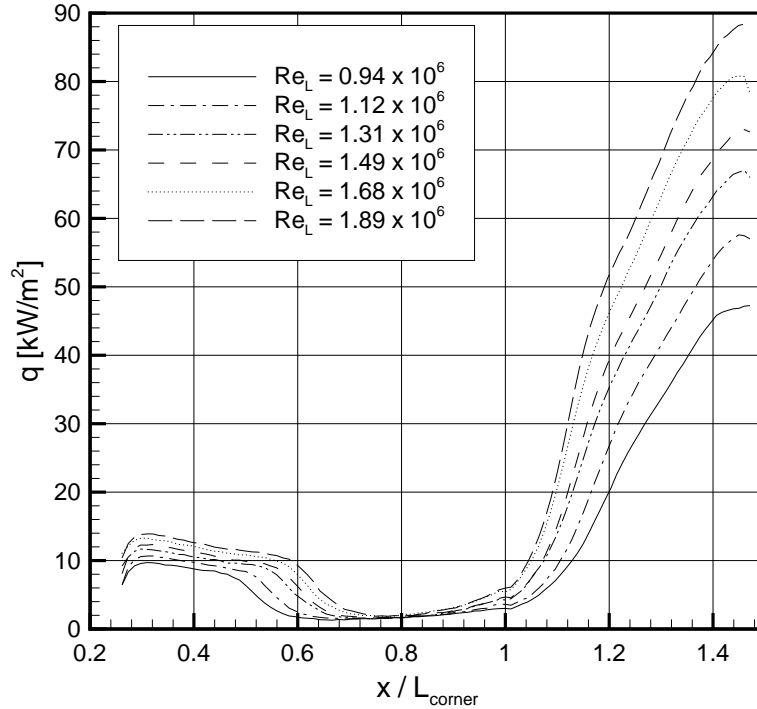
Figure 6.7: Heat transfer for clean nose runs

Input	M_1	p_3/p_1	$Re_{L,corner} \times 10^{-6}$
	5.56	5.47	0.97
Output	Laminar	Transitional	Turbulent
$c_{h,peak}/c_{h,ref}$	0.89	3.01	3.89

Table 6.2: Peak heating results for Hung and Barnett equations

The correlations give a laminar peak heating ratio smaller than one which is not realistic. This is caused by the limited applicability and the simplicity of the correlation. When regarding the transitional and turbulent correlation results and comparing them to the measured values, it appears that the measured peak heating ratios are a factor 2 to 3 higher.

A possible explanation the high peak heating ratio is transition in the separated shear layer. As the flow separates the heat transfer drops, in the separated region upstream of the flare the heat transfer remains about constant due to the thick separated layer. Over the flare the separated layer thickness decreases again causing the heat transfer to increase. As the relatively unstable free shear layer recompresses at the flare transition will occur which increases the heat transfer even further. The point of transition probably coincides with the inflexion point of the heat transfer curve at the flare but this is still open to discussion. Due to the compression of the entropy layer over the flare the typical transitional heat transfer signature is further masked.

This transition can also be seen on the spark schlieren pictures made by the high speed camera. In the schlieren pictures obtained by the CCD camera the transition is not evident due to the long exposure time (≈ 25 ms) and the use of a continuous light source, so that only a 'mean' wave is observed. From the instantaneous flow visualizations in figure 6.12 the transition process can be studied in more detail. In this figure digital enlargements from the high speed schlieren photographs are given. The enlargements are made in the separation and reattachment region and
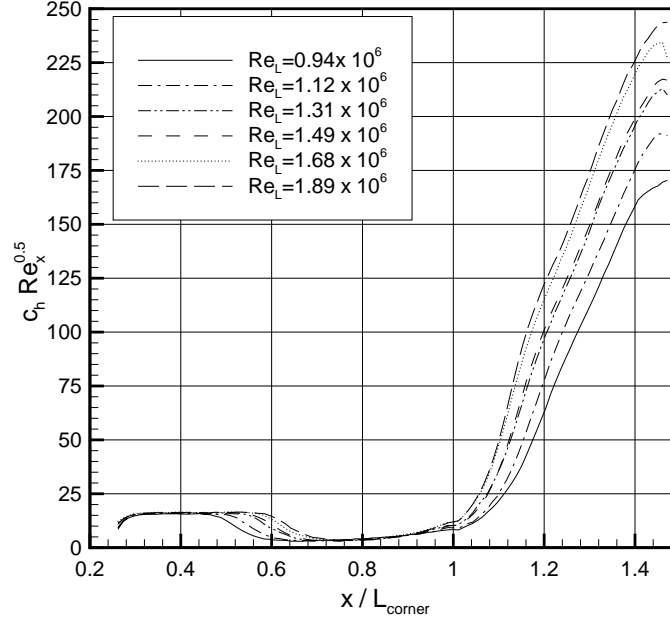
Figure 6.8: Correlation of c_h with $\sqrt{Re_x}$ for laminar attached flow

Figure 6.9: Color schlieren picture for clean nose at $Re_L = 1.88 \cdot 10^6$ and $M = 9.1$, $x_{sep}/L_{corner} = 0.63$

digitally enhanced using 'contrast' and 'sharpen' filters. Above the cone the bow and separation shocks are clearly visible as white lines. At the back of the flare the transition region is discernible, when the pictures are closely examined the flow structure can be seen to differ from picture to picture indicating an unsteady or relatively large-scale turbulent flow behaviour. Between the bow shock and the transitional region small 'white' shocks can be observed, in pictures 1, 3, 5 and 7 they are most evident and with a careful inspection they are found to be present in each picture. These shocklets are caused by the interaction of the outer flow with the transitional flow features of the free shear layer. The position of these shocks differs from picture to picture. When
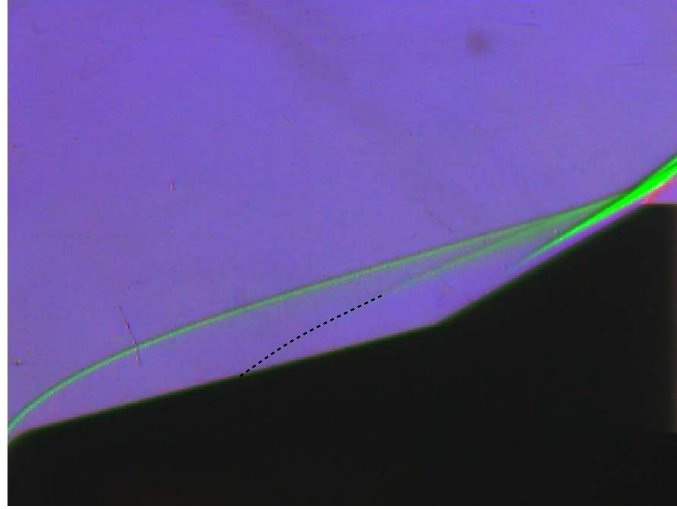
Figure 6.10: Color schlieren picture for clean nose at $Re_L = 1.51 \cdot 10^6$ and $M = 9.1$, $x_{sep}/L_{corner} = 0.61$

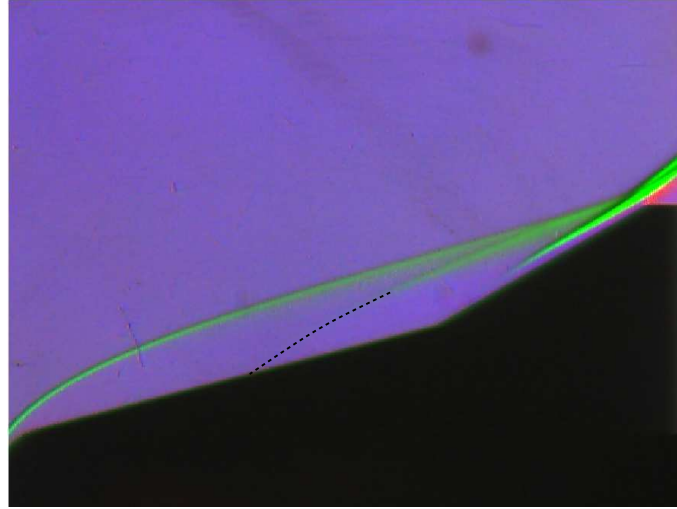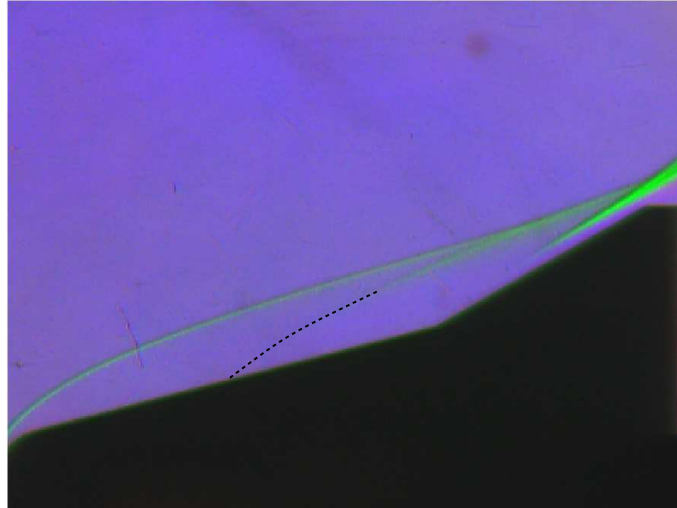Figure 6.11: Color schlieren picture for clean nose at $Re_L = 1.13 \cdot 10^6$ and $M = 9.1$, $x_{sep}/L_{corner} = 0.58$

the intersection of the separation shock and the bow shock is regarded it is found that this point moves in time, which may be induced by the unsteadiness caused by the free shear layer transition.

6.2.2   Roughened nose measurements

In figures 6.14 and 6.15 the Stanton number and the heat transfer curves are shown for the roughened nose. The corresponding schlieren pictures are shown in figures 6.16 to 6.18. The influence of the Reynolds number for the first part of the Stanton curve is not as evident as for the clean nose case, no systematic trend can be detected. In general an increase of the heat transfer with Reynolds number can be found, which is again caused by the increase in mass flow available for model heating. The overall Stanton number at the start of the cone is a factor 1.5 higher with respect to the clean nose configuration indicating a perturbed boundary layer. As the
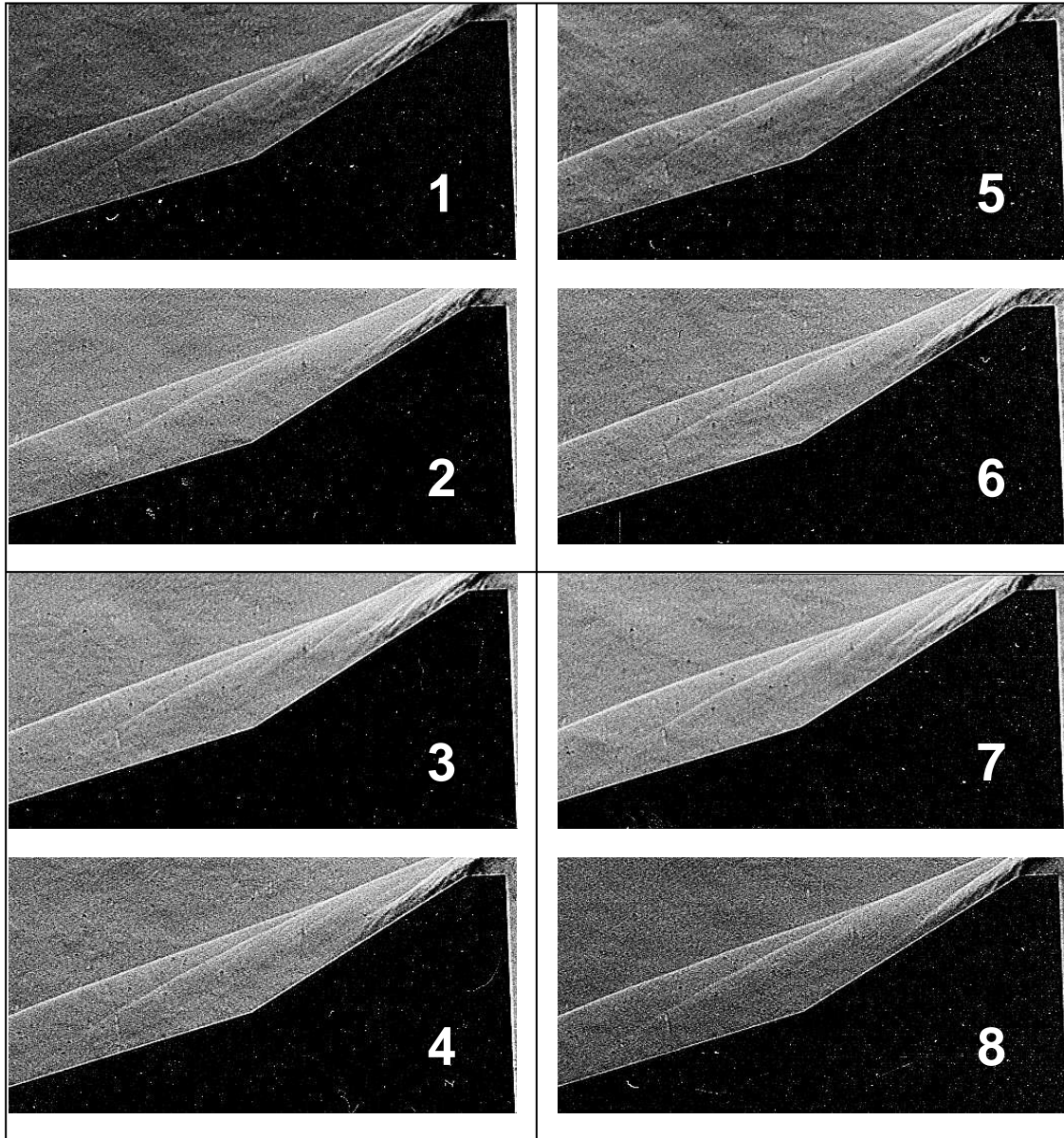
Figure 6.12: Schlieren photographs from high speed photography. Pictures 1 and 2 are consecutive and separated of 2 *ms*. This is also the case for 3 -4, 5-6 and 7-8. All pictures are from the same experiment

flow separates the heat transfer drops, for the lowest Reynolds number the separation location is comparable to the separation point of the clean nose results. Like in the clean nose case the separation point shifts downstream with increasing Reynolds number, only the shift extent is considerably larger. Consequently for the rough nose cases the separation point is more sensitive to the Reynolds number, see figure 6.13. The separation region becomes very small at high Reynolds numbers, this can also be concluded from figure 6.16 where the separation shock is absent and only the compression wave can be seen emerging from the compression corner. In figures 6.17 and 6.18 the separation shock can be seen, the separation point corresponds to the positions determined by the heat transfer measurements. Moving further downstream the heat transfer begins to rise sharply, the steepness of the heat transfer diagrams increases with the Reynolds number until an

Figure 6.13: Correlation of the separation point with the Reynolds number

attached flow field is achieved. Downstream of a steep increase a pause in the heat transfer is observed, Asma [5] explains this by stating that the flow is transitional in that region. Probably this is the same phenomenon occurring at the inflexion point in the clean nose case so also the 'plateau' coincides with the transition region.

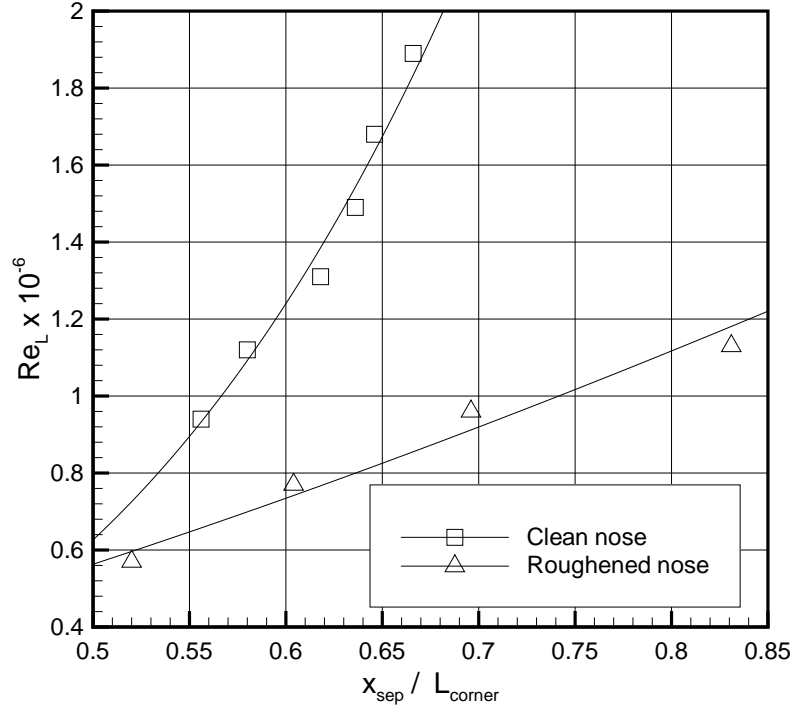For the roughened nose experiments the steepness of the heat transfer at the cone-flare junction is considerably higher compared to the clean nose configuration. This means that the free shear layer thickness decreases faster in the roughened nose case. Due to an already slightly perturbed boundary layer generated by the roughness at the nose more efficient mixing is established in the separated free shear layer. This causes the shear layer thickness to decrease since less outer flow needs to be entrained to overcome the recompression at the flare.

6.2.3 Conclusion

In the clean nose experiments a sharp decrease of the heat transfer is measured upstream of the flare-cone junction which is inextricably connected to boundary layer separation. When the Reynolds number is increased, the separation point is found to move downstream (separation is delayed). From the schlieren pictures the separation shock could be identified, the separation position closely agrees with the separation point deducted from the heat transfer measurements. Reattachment is unclear for the smooth nose configuration, the flow does not seem to reattach within the flare length although a recompression region is observed from the schlieren pictures at about half of the flare length and due to the compression of the entropy layer the flow features are masked. The heat transfer data shows a continuous increase starting from the compression corner. The peak heating observed at the end of the flare is 2 to 3 times higher than correlations from literature. No local peak heating on the flare is observed, only a small inflexion is noticed. So it is conjectured that the separated shear layer undergoes transition, which would explain the
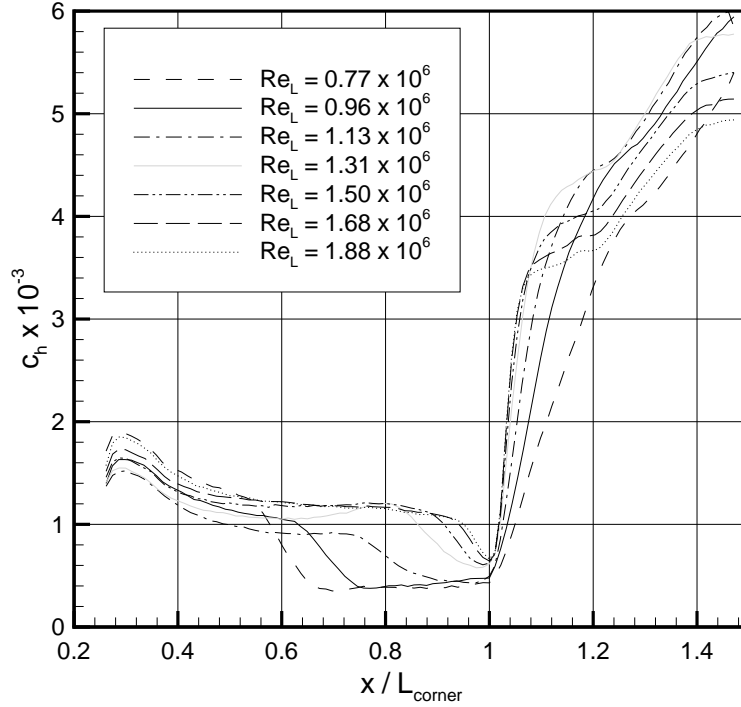
Figure 6.14: Stanton curves for roughened nose runs

continuous heat transfer increase and high peak heating at the end of the flare. This is supported by spark schlieren photographs showing significant unsteady behaviour by means of small shocks in the region at the aft half of the flare. The unsteady behaviour of the shear layer also caused the intersection of the bow and separation shock to move during an experiment.

The overall Stanton number at the start of the cone is a factor 1.5 higher with respect to the clean nose configuration indicating a perturbed boundary layer flow, with enhanced mixing, due to the nose roughness. The sensitivity of the separation extent with the Reynolds number for the roughened nose configuration is much higher and at high Reynolds numbers the separated region has virtually disappeared. For these Reynolds numbers the separation shock has disappeared and the schlieren pictures show only a single compression wave emerging from the compression corner. At the flare a 'plateau' in the heat transfer is observed which is also connected with transition. As the free shear layer recompresses along the flare the steepness of the heat transfer distribution is considerably higher for the rough nose with respect to the clean nose configuration. This is probably caused by the roughness at the nose inducing a more efficient mixing in the free shear layer.
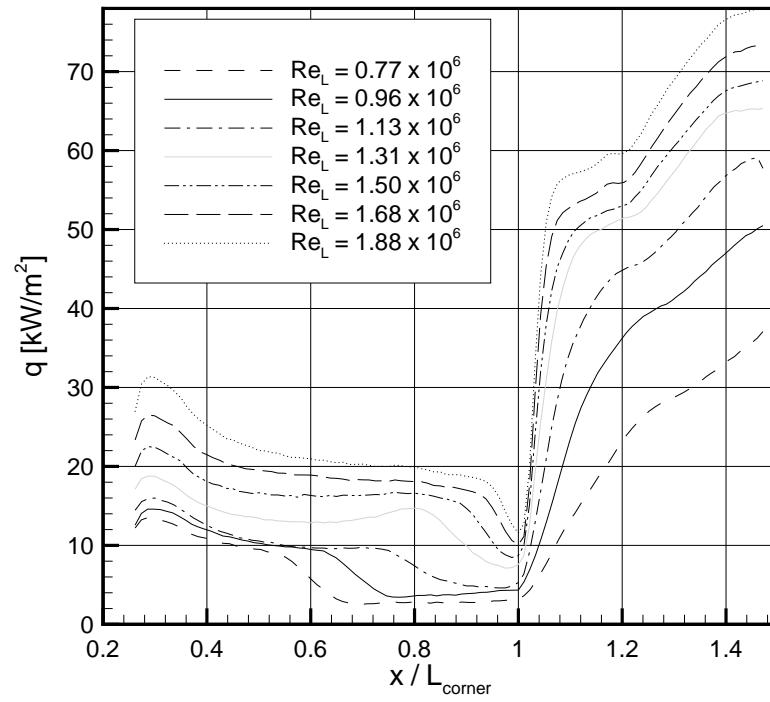
Figure 6.15: Heat transfer for roughened nose runs
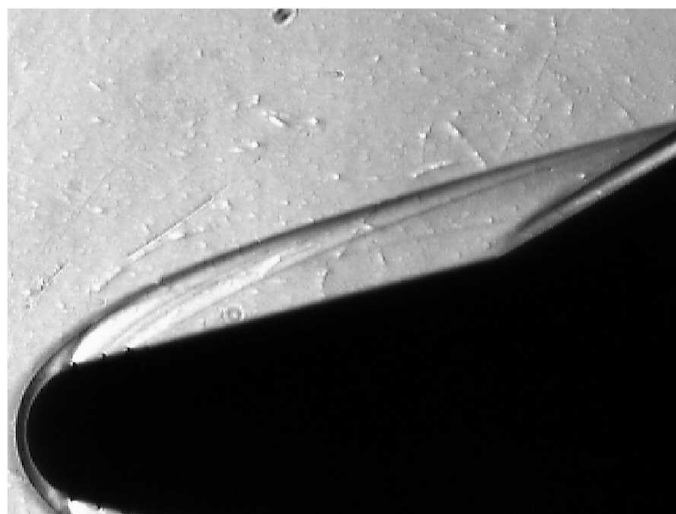
Figure 6.16: Schlieren picture for roughened nose at $Re_L = 1.88 \cdot 10^6$ and $M = 9.1$
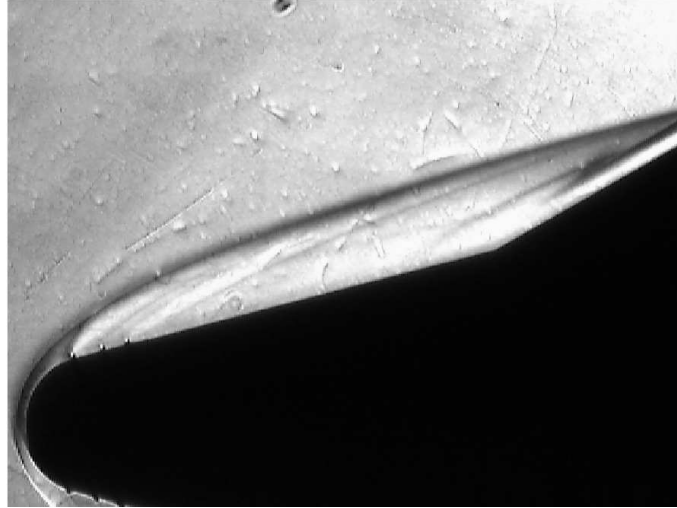
Figure 6.17: Schlieren picture for roughened nose at $Re_L = 1.30 \cdot 10^6$ and $M = 9.1$, $x_{sep}/L_{corner} = 0.83$
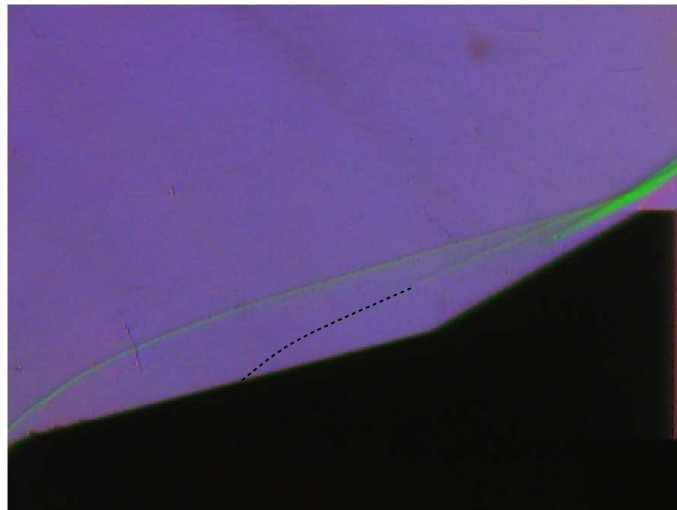
Figure 6.18: Color schlieren picture for roughened nose at $Re_L = 7.53 \cdot 10^5$ and $M = 9.1$, $x_{sep}/L_{corner} = 0.60$

Chapter 7

Conclusions

In the present study the application of infrared thermography on a blunted cone-flare in a short duration hypersonic facility is studied. The infrared technique has been successfully applied as a quantitative heat transfer diagnostic method. The infrared camera was successfully calibrated using a black body. For further accuracy the emissivity of the wind tunnel model was determined. Four different data reduction methods were used to obtain the heat transfer from the transient surface temperature, from which two groups were basically different (two optimizations versus two numerical integrations). The maximum difference between the heat transfer obtained with the different methods was about 10%.

The heat transfer measurements were conducted to investigate the boundary layer separation and reattachment on a blunted cone-flare. The heat transfer measurements were complemented by schlieren visualization. During the experiments the model was fitted with either a smooth or a roughened nose. On both configurations boundary layer separation, associated with a sharp drop in heat transfer, was measured. The separation point moves downstream (separation is delayed) with increasing Reynolds number, for the roughened nose the separation point is more sensitive to the Reynolds number, the separated region practically disappears for the higher Reynolds numbers. For the roughened nose configuration the overall Stanton number at the start of the cone is a factor 1.5 higher with respect to the clean nose configuration indicating a perturbed boundary layer. The schlieren photographs return among other features, the separation shock, which agrees satisfactorily with the heat transfer data with respect to the location of separation.

Reattachment is unclear for the smooth nose configuration, in fact the flow does not seem to reattach within the flare length, although a recompression region is visualized with the schlieren method originating at about half the flare length. The heat transfer data show a continuous increase starting from the cone-flare junction. No local peak heating is observed and only a very weak inflexion point can be seen. For the roughened nose case the heat transfer growth along the flare is distinctly paused. It is conjectured that the inflexion point in the smooth nose case and the 'plateau' in the roughened nose case is connected with shear layer transition justifying the continuous heat transfer increase and the high peak heating at the end of the flare. Due to the presence of the entropy layer (generated by the bow shock), which also recompresses at the flare, striking flow features at the flare, regarding reattachment or transition are masked.

The transition conjecture is supported by spark schlieren photographs for the smooth nose configuration showing significant unsteady behaviour at the aft half of the flare which is probably caused by the transition of the relatively unstable free shear layer due to the unfavourable pressure gradient. In the region between the transitional region and the bow shock small unsteady shocklets can be observed which are caused by the flow patterns due to the transitional free shear layer. The photographs also show an unsteady intersection position of the bow and separation shock.

For the roughened nose experiments the steepness of the heat transfer at the cone-flare junction is considerably higher compared to the clean nose configuration. This is caused by a more efficient mixing in the shear layer due to the flow perturbation by the roughness elements at the nose.

Chapter 8

Recommendations

Black body temperature accuracy

During calibration a temperature difference of 0.5 K was noticed over the black body, to reduce this temperature difference the black body has to be modified. Probably the water mass-flow rate through the black body is inadequate so the internal diameter of the copper coil has to be increased. The lack of mass-flow also manifested itself in the long time it took (approximately 1 hour) for the black body to achieve a thermal equilibrium.

Influence vacuum test-section

During the experiment there is almost a vacuum in the test-section whereas the calibration is carried out at ambient conditions. Due to the lack of air less radiation will be absorbed before it reaches the camera so slightly higher temperatures will be measured. The effect of the vacuum on the measured temperatures can be studied by placing an object in the test-section at a known temperature and to measure the temperature with and without vacuum.

Influence wind-tunnel wall temperature

In the data reduction, the sample values are corrected for the ambient temperature which in the current experiments is taken as the room temperature. This is generally true when monitoring in line-scan mode, the measured line mostly reflects the incident ambient radiation because it is most perpendicular to the relatively large window. Besides this it is still useful to asses the wall temperature during the run by monitoring a black spot on the wind-tunnel wall using the infrared camera.

Model geometry modification

In the present study due to the relatively complex geometry of the model there was a limited possibility to check the separation and reattachment phenomena with correlations from literature. So it will be instructive to consider a simplified sharp flat plate geometry to study the viscous interaction, a ramp can be added afterward to study the separation and reattachment. Using a sharp flat plate also increases the chance of a reattachment on the flare. Also the Mach number variation can be studied by placing the flat plate at different angles of attack. Finally a blunt leading-edge can be added to study the interaction of the entropy layer with the separation and reattachment phenomenon.

Sampling frequency of the infrared camera

The infrared camera used in the present study was only capable of operating in line-scan mode at the desired sampling frequency so it was not possible to check for thermal axisymmetry on the

model. In future experiments it is desirable to examine the azimuthal distribution of the surface heat transfer, especially when a non-zero angle of attack is considered where highly asymmetric heating patterns can appear.

Pressure measurements

Together with heat transfer measurements also pressure measurement need to be done to achieve a better understanding of the flow field since it is rather complex to understand, especially due to the interaction of the entropy layer with the separation and reattachment phenomenon. These pressure measurements can also be used to approximate the heat transfer though Cheng's equations [24] and other correlations.

Influence of the optimization method

For the calibration and data reduction the simplex optimization method was used. To study the influence of the optimization process on the data reduction, also another method (e.g. Powell's method) could be applied.

HTFD flow assessment

Since the Hypersonic Test Facility Delft has not been used on such an extensive basis more information has to be obtained regarding the determination of the flow quality and in particular of the stagnation quantities. Also the behaviour of the strongly undercooled gas flow close to the condensation point deserves a further assessment.

References

[1] http://www.dart-project.com, 12 2002.

[2] M.J. Flanagan , Jr. Aerodynamic heating in the vicinity of hypersonic, axisymmetric, shockwave-boundary layer interactions. AIAA-paper 93-2766, AIAA, 1993.

[3] John D. Anderson, Jr. *Hypersonic and high temperature gas dynamics*. McGraw-Hill, Boston, Massachusetts, 1989.

[4] John D. Anderson, Jr. *Modern compressible flow: With historical perspective*. McGraw-Hill, New York, 2nd edition, 1990.

[5] C.O. Asma, S. Paris, M.S.D. Tapsoba, and D.G. Fletcher. Transitional shock wave-boundary layer interaction over a cone-flare model at hypersonic conditions. In *Proc. 4th Europ Symp. Aerothermodynamics for Space Applications*, number 487 in sp, 2002.

[6] W.J. Bannink. De hypersone test faciliteit delft (htfd). Lezing: Najaarscolloquium J.M. Burgerscentrum, 29 oktober 1996.

[7] J.J. Bertin. *Hypersonic aerothermodynamics*. AIAA education series., Washington, DC, 1994.

[8] J. Buursink, T.J. van Baten, E. Mooij, and K.J. Sudmeijer. Dart: the delft aerospace re-entry test vehicle. Technical Report 00-V.4.07, IAF, 2000.

[9] G.M. Carlomagno and L. de Luca. Infrared thermography in heat transfer. In Wen-Jei Young, editor, *Handbook of flow visualization*, chapter 32, pages 531–553. Taylor & Francis, 1989.

[10] D.R. Chapman. A theoretical analysis of heat transfer in regions of separated flow. Technical Report TN-3792, NACA, 1956.

[11] D.R. Chapman, D.M. Kuehn, and K.H. Larson. Investigation of separated flows in supersonic and subsonic streams with emphasis on the effects of transition. Technical Report 1356, NACA, 1958.

[12] R. Chase and M. Tang. The quest for single stage to orbit: Tav, nasp, dc-x and x-33 accomplishments, deficiencies, and why they did not fly. AIAA-paper 2002-5143, AIAA, 2002.

[13] H.K. Cheng, J. Gordon Hall, T.C. Golian, and A. Hertzberg. Boundary-layer displacement and leading edge bluntness effects in high temperature hypersonic flow. *AIAA journal*, 9(1):84–93, 1971.

[14] W.J. Cook and E.J. Felderman. Reduction of data from thin-film heat-transfer gages: A concise numerical technique. *AIAA journal*, 4(3):561, 562, 1995.

[15] M.O. Creager. Effects of leading-edge blunting on the local heat transfer and pressure distributions over flat plates in supersonic flow. Technical Report TN-4142, NACA, 1957.

[16] L. de Luca, G. Cardone, D.M. de la Chevalerie, and A. Fonteneau. Viscous interaction phenomena in hypersonic wedge flow. *AIAA journal*, 33(12):2293–2298, 1995.

[17] J. Delery and J.G. Marvin. Shock-wave boundary layer interactions. AG 280, AGARD, France, 1986.

[18] D.M. Boscher D.L. Balageas and A.A. Deom. Measurement of convective heat-transfer coefficients on a wind tunnel model by passive and stimulated infrared thermography. Technical Report 1990-96, Onera, 1990.

[19] H. Friehmelt, G. Koppenwallner, and R. Muller-Eigner. Calibration and first results of a redesigned ludwieg expansion tube. AIAA-paper 93-5001, AIAA, 1993.

[20] F. Grasso and M. Marini. Analysis of hypersonic shock-wave laminar boundary-layer interaction phenomena. *Computers & fluids*, 25(6):561–581, 1996.

[21] K.S. Heffner, A. Chpoun, and J.C. Lengrand. Experimental study of transitional axisymmetric shock-boundary layer interactions at mach 5. AIAA-paper 93-3131, AIAA, 1993.

[22] M.S. Holden. Leading-edge bluntness and boundary-layer displacement effect on attached and separated laminar boundary layers in a compression corner. Technical Report 68-68, AIAA, 1968.

[23] M.S. Holden. Boundary-layer displacement and leading edge bluntness effects on attached and separated boundary layers in a compression corner. part ii: experimental study. *AIAA journal*, 9(1):84–93, 1971.

[24] M.S. Holden. A study of flow separation in regions of shock wave-boundary layer interaction in hypersonic flow. Technical Report 78-1169, AIAA, 1978.

[25] K. Hozumi, Y. Yamamoto, and K. Fujii. Investigation of hypersonic compression ramp heating at high angles of attack. *Journal of spacecraft and rockets*, 38(4):488–496, 2001.

[26] F.T. Hung and D.O. Barnett. Shockwave-boundary layer interference heating analysis. Technical Report 73-237, AIAA, 1973.

[27] F. Kreith and Mark S. Bohn. *Principles of heat transfer.* Brooks/Cole, Pacific Grove, CA, 6th edition, 2001.

[28] S.G. Mallinson, S.L. Gai, and N.R. Mudford. The interaction of a shock wave with a laminar boundary layer at a compression corner in high-enthalpy flows including real gas effects. *Journal of fluid mechanics*, 342:1–35, 1997.

[29] M. Marini. Effects of flow and geometry parameters on shock-wave boundary-layer interaction phenomena. AIAA-paper 98-1570, AIAA, 1998.

[30] R. Mayer. Orientation on quantitative IR-thermography in wall shear stress measurements. report LR-812, Delft University of Technology, Delft, 1996.

[31] D.A. Needham and J.L. Stollery. Boundary layer separation in hypersonic flow. AIAA-paper 66-455, AIAA, 1966.

[32] J. Olejniczak, M.J. Wright, and G.V. Candler. Numerical study of inviscid shock interactions on double-wedge geometries. *journal of fluid mechanics*, 352:1–25, 1997.

[33] M. Rasmussen. *Hypersonic flow.* John Wiley & Sons, Inc., New York, 1994.

[34] D.L. Schultz and T.V. Jones. Heat-transfer measurements in short-duration hypersonic facilities. AG 165, AGARD, France, 1973.

[35] G.S. Settles. *Schlieren and shadowgraph techniques.* Springer, New York, 2001.

[36] G. Simeonides. The vki hypersonic wind tunnels and associated measurement techniques. TM 46, von Karman Institute, Belgium, 1990.

[37] G. Simeonides. *Hypersonic shock wave boundary layer interactions over compression corners.* PhD thesis, von Karman Institute, Belgium, April 1992.

[38] G. Simeonides, W. Haase, and M. Manna. Experimental, analytical and computational methods applied to hypersonic compression ramp flows. Technical report, von Karman Institute, Belgium, 1993.

[39] Frank M. White. *Viscous fluid flow.* McGraw-Hill, Singapore, 2nd edition, 1991.

Appendix A

Derivation of Cook and Feldermann integration function

The heat transfer is given by:

$$q_s = \frac{\sqrt{\rho c k}}{\sqrt{\pi}} \left[\frac{\phi(t)}{\sqrt{t}} + \int_0^t \frac{\phi(t) - \phi(\tau)}{(t-\tau)^{3/2}} d\tau \right], \tag{A.1}$$

$\phi(\tau)$ is approximated by a piecewise linear function of the form:

$$\bar{\phi}(\tau) = \phi(t_{i-1}) + \frac{\phi(t_i) - \phi(t_{i-1})}{\Delta t} (\tau - t_{i-1}) \tag{A.2}$$

where $t_{i-1} \leq \tau \leq t_i$ and $i = 1, 2, 3, \ldots, n$. The integral in equation (A.1) can be written as:

$$
\begin{aligned}
R(t_n) &= \frac{1}{2} \int_0^{t_n} \frac{\phi(t_n) - \bar{\phi}_\tau}{(t_n-\tau)^{3/2}} d\tau \\[2mm]
&= \frac{1}{2} \sum_{i=1}^n \int_{t_{i-1}}^{t_i} \frac{\phi(t_n) - \bar{\phi}_\tau}{(t_n-\tau)^{3/2}} d\tau \\[2mm]
&= \frac{1}{2} \sum_{i=1}^n \int_{t_{i-1}}^{t_i} \left[\phi(t_n) - \phi(t_{i-1}) - \frac{\phi(t_i) - \phi(t_{i-1})}{\Delta t}(\tau - t_{i-1}) \right] \frac{d\tau}{(t_n-\tau)^{3/2}} \\[2mm]
&= \frac{1}{2} \sum_{i=1}^n \left\{ [\phi(t_n) - \phi(t_{i-1})] \int_{t_{i-1}}^{t_i} \frac{d\tau}{(t_n-\tau)^{3/2}} - \left[\frac{\phi(t_i) - \phi(t_{i-1})}{\Delta t} \right] \int_{t_{i-1}}^{t_i} \frac{(\tau - t_{i-1})}{(t_n-\tau)^{3/2}} d\tau \right\}
\end{aligned}
\tag{A.3}
$$

Considering the first integral in equation (A.3):

$$\int_{t_{i-1}}^{t_i} \frac{d\tau}{(t_n - \tau)^{3/2}} = \left[\frac{2}{(t_n - \tau)^{1/2}} \right]_{t_{i-1}}^{t_i} = 2 \left[\frac{1}{(t_n - t_i)^{1/2}} - \frac{1}{(t_n - t_{i-1})^{1/2}} \right] \tag{A.4}$$

Considering the last integral in equation (A.3) and integrating by parts:

$$
\begin{aligned}
\int_{t_{i-1}}^{t_i} \frac{\tau - t_{i-1}}{(t_n-\tau)^{3/2}} &= \left[\frac{2(\tau - t_{i-1})}{(t_n-\tau)^{1/2}} \right]_{t_{i-1}}^{t_i} - 2 \int_{t_{i-1}}^{t_i} \frac{d\tau}{(t_n-\tau)^{1/2}} \\[2mm]
&= \left[\frac{2(t_i - t_{i-1})}{(t_n-t_i)^{1/2}} \right] + \left[4(t_n - \tau)^{1/2} \right]_{t_{i-1}}^{t_i} \\[2mm]
&= \frac{2\Delta t}{(t_n-\tau)^{1/2}} + 4 \left[(t_n - t_i)^{1/2} - (t_n - t_{i-1})^{1/2} \right]
\end{aligned}
\tag{A.5}
$$

Substituting equations (A.4) and (A.5) into (A.3):

$$
\begin{aligned}
R(t_n) = \frac{1}{2} \sum_{i=1}^n \Bigg\{ &2 \left[\phi(t_n) - \phi(t_{i-1}) \right] \left[\frac{1}{(t_n-t_i)^{1/2}} - \frac{1}{(t_n-t_{i-1})^{1/2}} \right] \\
&- \left[\frac{\phi(t_i) - \phi(t_{i-1})}{\Delta T} \right] \left[\frac{2\Delta t}{(t_n-\tau)^{1/2}} + 4 \left((t_n - t_i)^{1/2} - (t_n - t_{i-1})^{1/2} \right) \right] \Bigg\}
\end{aligned}
\tag{A.6}
$$

Now:

$$(t_n - t_i)^{1/2} - (t_n - t_{i-1})^{1/2} = \frac{t_i - t_{i-1}}{(t_n - t_i)^{1/2} + (t_n - t_{i-1})^{1/2}} = \frac{-\Delta t}{(t_n - t_i)^{1/2} + (t_n - t_{i-1})^{1/2}}$$

and substituting into equation (A.6) and grouping terms:

$$R(t_n) = \sum_{i=1}^{n} \frac{\phi(t_n) - \phi(t_i)}{(t_n - t_i)^{1/2}} - \sum_{i=1}^{n} \frac{\phi(t_n) - \phi(t_{i-1})}{(t_n - t_{i-1})^{1/2}} + 2\sum_{i=1}^{n} \frac{\phi(t_i) - \phi(t_{i-1})}{(t_n - t_i)^{1/2} - (t_n - t_{i-1})^{1/2}} \qquad (A.7)$$

At $i = n$, the first term in equation (A.7) is indeterminate. since however , $E(t)$ was taken as piecewise linear:

$$\lim_{\tau \to t_n} \left[\frac{K(t_n - \tau)}{(t_n - \tau)^{1/2}} \right] = 0$$

Equation (A.7) may therefore be written as:

$$\begin{aligned} R(t_n) &= \sum_{i=1}^{n-1} \left\{ \frac{\phi(t_n) - \phi(t_i)}{(t_n - t_i)^{1/2}} - \frac{\phi(t_n) - \phi(t_{i-1})}{(t_n - t_{i-1})^{1/2}} \right. \\ &+ \left. 2\frac{\phi(t_i) - \phi(t_{i-1})}{(t_n - t_i)^{1/2} + (t_n - t_{i-1})^{1/2}} \right\} + \frac{\phi(t_n) - \phi(t_{n-1})}{\sqrt{\Delta t}} \end{aligned} \qquad (A.8)$$

Equation (A.1) can now be written as:

$$\begin{aligned} q_n &= \frac{\sqrt{\rho c k}}{\sqrt{\pi}} \left[\frac{\phi(t)}{\sqrt{t}} + \sum_{i=1}^{n-1} \left\{ \frac{\phi(t_n) - \phi(t_i)}{(t_n - t_i)^{1/2}} - \frac{\phi(t_n) - \phi(t_{i-1})}{(t_n - t_{i-1})^{1/2}} \right. \right. \\ &+ \left. \left. 2\frac{\phi(t_i) - \phi(t_{i-1})}{(t_n - t_i)^{1/2} + (t_n - t_{i-1})^{1/2}} \right\} + \frac{\phi(t_n) - \phi(t_{n-1})}{\sqrt{\Delta t}} \right]. \end{aligned} \qquad (A.9)$$

Appendix B

Thermocouple temperature measurements

Thermocouple measurements are based on the thermal electrical effect of conductors. The kinetic energy of electrons in a conductor depends on the temperature of the conductor. When the temperature of the conductor is high, the kinetic energy increases (Fermi and Dirac). When a temperature difference exists in a conductor a current will be generated due to the movement of the electrons towards the colder side of the conductor. This current will continue until an equilibrium is achieved with the electrical field, see figure B.1. When two conductors a and b are
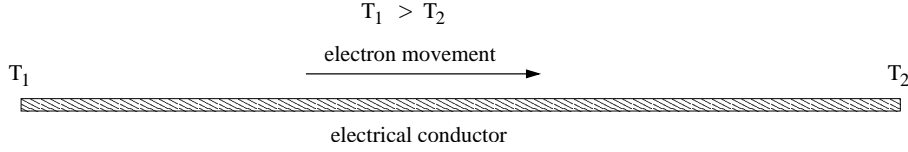
Figure B.1: Electron movement in an electrical conductor

coupled on one side, a voltage can be measured at the loose ends. This combination is called a thermocouple, see figure B.2. The voltage over a conductor is proportional to the temperature
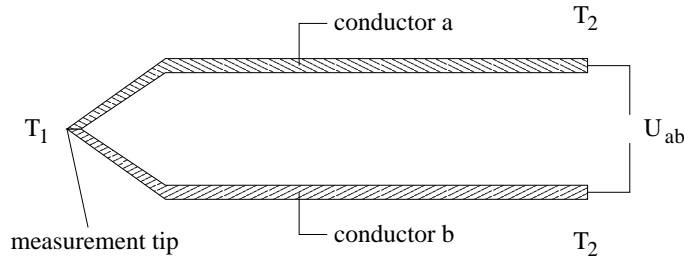
Figure B.2: Electron movement in an electrical conductor

difference over the conductor:

$$U = S(T)[T_1 - T_2], \tag{B.1}$$

where S is the Seebeck coefficient which defines the thermal electrical characteristic of the conductor. For a thermocouple this correlation becomes

$$U_{ab} = U_a - U_b = \{S_a(T) - S_b(T)\}[T_1 - T_2] = S_{ab}(T)[T_1 - T_2]. \tag{B.2}$$

Now the coupled tip (at temperature T_1) can be used as a measurement point. When the voltage over the loose ends is measured, the temperature difference $T_1 - T_2$ is measured. Thus T_2 acts as the reference temperature. In practice a second thermocouple is added, see figure B.3 and the measurement tip of this thermocouple is kept at a constant known temperature by placing it in melting ice. Now the second measurement tip is always at $0°C$ and the exact temperature is measured.

$$U_{\text{measure}} = S_{ab}[T_1 - T_2] - S_{ab}[0 - T_2] = S_{ab} \cdot T_1 \tag{B.3}$$

Because S_{ab} can depend on the temperature calibration tables are available which correlate the measured voltage to the temperature. In the current experiments only K-type thermocouples are used (NiCr - Ni) which have an almost constant S_{ab}.
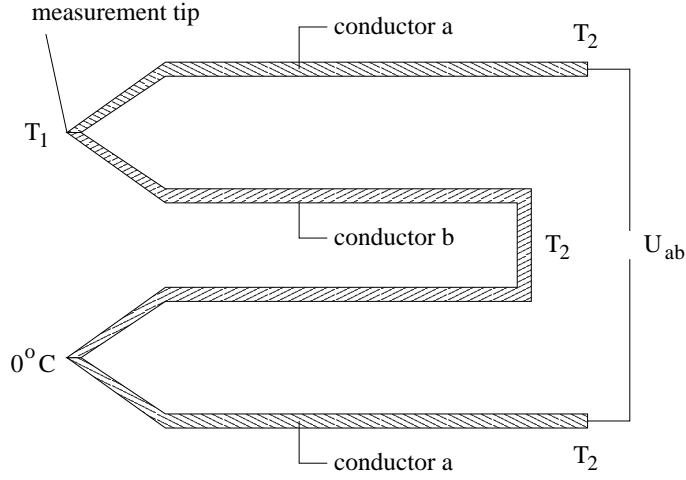
Figure B.3: Combined thermocouple

Appendix C

Simplex method

The simplex method is based on the utilization of subsets in E_n which are spanned by $n+1$ points (vertices) in E_n. This subset is referred to as a simplex.

Consider $n + 1$ vertices $x^0, x^1, \ldots, x^n$ and the corresponding function values are denoted by $f_i = f(x^i)$. For simplicity a consecutive numbering of the vertices is assumed such that $f_0 \leq f_1 \leq \ldots \leq f_n$. The principal idea of the method is that a new simplex can easily be formed from the current one by reflecting x^n in the hyperplane spanned by the remaining points; at the new point, the function value will often be lower than f_n. If this is the case, the process can be continued with a new simplex.

First a centroid is generated

$$x^* = \frac{1}{n} \sum_i^{n-1} = x^i \tag{C.1}$$

and the reflected vertex is generated

$$x^r = x^* + \alpha \left(x^* - x^n \right), \tag{C.2}$$

where α is a positive constant (≈ 1). Now $f_r = f(x^r)$ can be computed, the value of f_r determines which one of the following three operations is performed:

- Reflection: If $f_0 \leq f_r \leq f_{n-1}$, the reflected point x^r is accepted and the vertex x^n is dropped. The vertices are now renumbered in ascending order of correspondig function values and computations are restarted using the new simplex.

- Contraction: If $f_r > f_{n-1}$, replacing x^n by x^r would leave x^r as the new maximum. Therefore the simplex is contracted: if $f_r > f_n$, x^c is computed by

$$x^c = x^* + \beta \left(x^n - x^* \right); \tag{C.3}$$

else

$$x^c = x^* + \beta \left(x^r - x^* \right). \tag{C.4}$$

The contraction coefficient β lies between 0 and 1 ($0 < \beta < 1$) and mostly is taken to be equal to 0.5. If $f_c \leq \min \left(f_n, f_r \right)$, x^n is replaced by x^c, the vertices are renumbered and the computations are restarted with the new vertex. If $f_c > \min \left(f_n, f_r \right)$, the contraction has failed and the simplex has to be shrinked to x^0 (all vertices are replaced except x^0)

$$x^i = x^0 + \Delta \left(x^i - x^0 \right) \tag{C.5}$$

where $i = 1 \ldots n$ and $\Delta = \frac{1}{2}$. The vertices are renumbered and the computation is restarted.

- Expansion: If $f_r < f_0$, the reflected point is x^r is a new minimum. Then x^e is generated by expanding into x^r

$$x^e = x^r + \gamma \left(x^r - x^* \right) \tag{C.6}$$

where the expansion coefficient, γ is a positive constant (≈ 2). If $f_e < f_r$, x^n is replaced by x^e and the computation is restarted after renumbering the vertices; otherwise the expansion has failed and x^n is replaced by x^r before restarting.
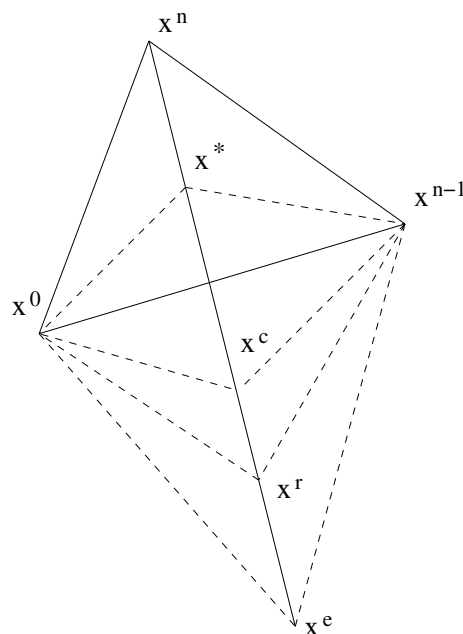
Figure C.1: The simplex method in 2D

The computation is stopped if the variation of the function value has dropped below a certain prescribed value $|f_0 - f_n| < \text{tol}_f$ or if the distance between the vertices becomes very small.

If the optimization does not converge, the computation is also stopped after a certain number of function evaluations or iterations. The computation is stopped if the number of iterations or function evaluations has exceeded a prescribed number (this mostly means a good optimization is not possible).

Appendix D

BRUT system file format

The BRUT system stores its file in a binary format, the structure of the format (image and header) is explained below. A single image (frame) consists of four fields, each consisting of 70 lines of 140 pixels, each pixel consisting of 2 bytes, the first byte being the most significant.
A frame takes up 140 pixels * 70 lines * 2 bytes * 4 fields = 78400 bytes when it is stored.
Each pixel is 16 bits long. The image data is contained in the 13 least significant bits. Bit 13 and 14 are of no use, while the most significant bit (bit 15) is used to encode the recording time of each field.
The 8 bytes of recording time data for a field is spread out on the most significant bit (nr 15) of the first 64 pixels of the top of the field. The first pixel of the top line contains the most significant bit of the first byte in the 8 bytes recording time data. The 8 bytes of recording time data are organized as follows:

byte 0:	not used
byte 1:	year, binary 0-99
byte 2:	month, binary 1-12
byte 3:	day, binary 1-31
byte 4:	hour, binary 0-23
byte 5:	minutes, binary 0-59
byte 6:	seconds, binary 0-59
byte 7:	hundredth's of seconds, binary 0-99

A sequence of images on the network consists of a 512 byte file header, followed by the images which constitutes the secquence. The images are stored in image format and packed end to end without any fillers between the individual images. The layout of the header is given below.

Byte offset	Field	Type
0	Identification of the file as a BRUT sequence (Constant hex. number 13977931)	Integer
4	Sequence name (Max 80 bytes)	String
84	Sequence length in number of images	Integer
88	Recording date (00, year, month, day)	Integer
92	Recording time (h, m, s, ms)	Integer
96	Not used	
100	Scanner type identification	String
126	Scanner data message	String
134	User comment (Max 80 bytes)	String
214	Trigger date (00, year, month, day)	Integer
218	Trigger time (h, m, s, ms)	Integer
222	R - Scanner calibration response factor	Float
230	B - Scanner calibration spectral factor	Float
238	F - Scanner calibration shape factor	Float
246	α atmospheric attenuation	Float
254	β atmospheric attenuation	Float
262	Distance from scanner to calibration blackbody	Float
270	Atmospheric temperature	Float
278	Ambient temperature	Float
286	P_{IU} isothermal unit per sample value	Float
294	ϵ_0 for spot temperature calculation	Float
302	Distance form scanner to spot	Float
310	ϵ_0 for area temperature calculation	Float
318	Distance from scanner to area	Float
326	Rest is not used	

Table D.1: Network file header layout

Appendix E

Data reduction program description

In this appendix the data reduction program structure is explained. The program need four files in specific directories. The first is `htfd_ir.cfg`, this file contains the name of the configuration file which has to be read, it is placed in the same directory as the main program. The second file is the HP1000 file, this file contains the pressure data from the HTFD and must be placed in the subdirectory `/data`. In this directory also the BRUT file has to be placed, the filename has to be the same as the HP1000 filename but the extension has to be `.bsl` (Binary Line Sequence). And finally the cfg file is used to define user input variables, this file must be placed in the subdirectory `/cfg`. The name of the cfg file has to be identical to the HP1000 and the BRUT filename but with a `.cfg` extension. Also a `/graphs` directory has to be created, in this directory the graphs created by the data reduction program are saved. The program also generates save files which can be read by TECplot and they are saved in the `/data` directory

The program can be run in two modes, a tuning mode and the normal data reduction mode. When in tune mode, the program only does a data reduction for one pixel (mean of nose and back pixel) and saves the results in graph form in the main directory so they can be evaluated. This enables the user to adjust the cropping borders or change other variables quickly without having to wait for the complete data reduction to end. The essential files for the data reduction are summarized below.

`ir_htfd`	main program
`htfd_ir.cfg`	cfg file
`/data/htfd052`	HP1000 file
`/data/htfd052.bsl`	BRUT file
`/cfg/htfd052.cfg`	cfg file

The cfg file allows the user to modify certain variables regarding the data reduction process. In the table below the structure of the cfg file is outlined.

Value	Description
52	Shot number
9.13	Nozzle for Mach
773.15	Reservoir tube temperature [K]
70	Reservoir tube pressure [bar]
297.95	Ambient temperature [K]
69090	R response factor (obtained from calibration)
1063.6	B spectral factor (obtained from calibration)
-0.0517466	F shape factor (obtained from calibration)
134	Pixel where the nose starts
72	Pixel where the corner is
28	Pixel where the back is
480	Number of points to skip before optimization data reduction starts
1120	Number of points to skip at the end for optimization data reduction
550	Number of points to skip before direct and indirect data reduction starts
1370	Number of points to skip at the end of direct and indirect data reduction
0	Flag for interval adjustments (1 = on, 0 = off)
100000	Maximum number of function evaluations for optimization process
80000	Maximum number of iterations for optimization process
1000	`h_opt`, starting value for erfc optimization process [W/(m2 K)]
100	`Taw_opt`, starting value for erfc optimization process [K]
0.1	`t0_opt`, starting value for erfc and sqrt optimization process [s]
1000	`q_opt`, starting value for erfc optimization process [W]
5	Size of the Gaussian filter (always odd number) for direct and indirect data reduction
10	Sigma of the Gaussian filter for direct and indirect data reduction

Table E.1: Cfg file layout

Appendix F

Overview of the test conditions

Run nr	Roughness	Observation	p_0	T_0	p_t	T_t	$Re_L \times 10^6$
30	Clean	Strobodrum	74.4	773.15	66.1	747.64	1.40
31	Clean	Strobodrum	74.5	773.15	66.2	747.64	1.40
32	Clean	IR	100.0	773.15	88.8	747.64	1.88
33	Clean	IR	74.9	773.15	66.5	747.64	1.41
34	Clean	IR	50.3	773.15	44.7	747.64	0.95
36	Clean	IR	50.1	773.15	44.5	747.64	0.94
37	Clean	IR	50.3	773.15	44.7	747.64	0.95
38	Clean	IR	49.9	773.15	44.3	747.64	0.94
39	Clean	IR	79.1	773.15	70.2	747.64	1.49
40	Clean	IR	80.0	773.15	71.0	747.64	1.51
41	Clean	IR	78.9	773.15	70.1	747.64	1.49
42	Clean	IR	59.7	773.15	53.0	747.64	1.12
43	Clean	IR	59.6	773.15	52.9	747.64	1.12
44	Clean	IR	59.3	773.15	52.7	747.64	1.12
45	Clean	IR	89.0	773.15	79.0	747.64	1.68
46	Clean	IR	91.0	773.15	80.8	747.64	1.71
47	Clean	IR	89.0	773.15	79.0	747.64	1.68
48	Clean	IR	99.8	773.15	88.6	747.64	1.88
50	Clean	IR	100.2	773.15	89.0	747.64	1.89
51	Clean	IR	69.9	773.15	62.1	747.64	1.32
52	Clean	IR	69.5	773.15	61.7	747.64	1.31
53	Clean	IR	69.7	773.15	61.9	747.64	1.31
54	1R 0.5[mm]	IR	68.9	773.15	61.2	747.64	1.30
55	1R 0.5[mm]	IR	50.5	773.15	44.8	747.64	0.95
56	1R 1.0[mm]	IR	90.4	773.15	80.3	747.64	1.70
57	3R	Schlieren	49.7	773.15	44.1	747.64	0.94
58	3R	Schlieren	69.0	773.15	61.3	747.64	1.30
59	3R	Schlieren	94.3	773.15	83.7	747.64	1.78
60	3R	Schlieren	99.9	773.15	88.7	747.64	1.88
61	3R	IR	49.2	773.15	43.7	747.64	0.93
62	3R	IR	51.1	773.15	45.4	747.64	0.96
63	3R	IR	49.8	773.15	44.2	747.64	0.94
64	3R	IR	40.4	773.15	35.9	747.64	0.76
65	3R	IR	40.7	773.15	36.1	747.64	0.77
66	3R	IR	40.1	773.15	35.6	747.64	0.76
67	3R	IR	60.0	773.15	53.3	747.64	1.13
68	3R	IR	59.3	773.15	52.7	747.64	1.12
69	3R	IR	60.2	773.15	53.5	747.64	1.13
70	3R	IR	70.0	773.15	62.2	747.64	1.32
71	3R	IR	100.3	773.15	89.1	747.64	1.89
72	3R	IR	99.5	773.15	88.4	747.64	1.88
73	3R	IR	99.1	773.15	88.0	747.64	1.87
74	3R	IR	89.3	773.15	79.3	747.64	1.68
75	3R	IR	89.0	773.15	79.0	747.64	1.68
76	3R	IR	89.4	773.15	79.3	747.64	1.68
77	3R	IR	79.5	773.15	70.6	747.64	1.50
78	3R	IR	79.0	773.15	70.2	747.64	1.49
79	3R	IR	80.1	773.15	71.1	747.64	1.51
80	3R	IR	69.6	773.15	61.8	747.64	1.31
81	3R	IR	69.0	773.15	61.3	747.64	1.30
82	3R	IR	30.1	773.15	26.7	747.64	0.57
83	3R	IR	29.7	773.15	26.4	747.64	0.56
84	3R	IR	30.5	773.15	27.1	747.64	0.57

Table F.1: Overview of test conditions